CONTINUUM DAMAGE MECHANICS BASED MODELLING OF LAMINATED FIBER REINFORCED COMPOSITES

A Thesis Submitted to
the Graduate School of
İzmir Institute of Technology
in Partial Fulfillment of the Requirements for the Degree of

DOCTOR OF PHILOSOPHY

in Civil Engineering

by
Süleyman YAŞAYANLAR

June 2023
İZMİR

We approve the thesis of **Süleyman YAŞAYANLAR**

Examining Committee Members:

Prof. Dr. H. Seçil ARTEM
Department of Machine Engineering, İzmir Institute of Technology

Prof. Dr. Engin AKTAŞ
Department of Civil Engineering, İzmir Institute of Technology

Prof. Dr. Babür DELİKTAŞ
Department of Civil Engineering, Uludağ University

Assoc. Prof. Dr. İzzet ÖZDEMİR
Department of Civil Engineering, İzmir Institute of Technology

Assoc. Prof. Dr. S. Can Girgin
Department of Civil Engineering, Dokuz Eylül University

22 June 2023

Assoc. Prof. Dr. İzzet ÖZDEMİR
Supervisor, Department of Civil Engineering
İzmir Institute of Technology

Prof. Dr. Cemalettin DÖNMEZ
Head of the Department of
Civil Engineering

Prof. Dr. Mehtap EANES
Dean of the Graduate School

ACKNOWLEDGMENTS

I express my gratitude to my advisor, Associate Professor Dr. İzzet Özdemir, for his support, patience, and dedication. Without his guidance and expertise, completing this thesis would not have been possible. It has been a great honor to have the opportunity to work with him during this chapter of my life.

I would like to thank my thesis examining committee members, Prof. Dr. H. Seçil Artem, Prof. Dr. Engin Aktaş, Prof. Dr. Babür Deliktaş and Assoc. Prof. Dr. S. Can Girgin for their precious comments on my study.

I would also have to thank to my colleagues Bekir Kaçmaz and Petek Kaçmaz for all their support during this journey.

Additionally, I am deeply thankful to my beloved wife Yonca Yaşayanlar and my family for their invaluable support and encouragement.

ABSTRACT

CONTINUUM DAMAGE MECHANICS BASED MODELLING OF LAMINATED FIBER REINFORCED COMPOSITES

Multiscale modeling, which merges the worlds of macro- and micromechanics, is establishing itself as a viable alternative to experimental procedures in the characterization of the mechanical behavior of complex materials. Advanced composite materials are a perfect field for the application of such modeling concepts. This thesis focuses on failure mechanics of fiber reinforced composites and addresses the modeling of failure processes at both micro- and macro-scales. First, a novel damage-plasticity model is developed and implemented within finite element software Abaqus as a user defined element. It is verified that the model gives mesh objective results, and the model is calibrated with experimental stress-strain curves from the literature. Representative volume elements (RVEs) based micro-mechanical models are constructed where damage-plasticity model and cohesive surfaces are employed to capture failure in matrix and matrix-fiber interface, respectively. A sufficiently large number of RVE analysis results are used to generate discrete failure envelopes. These failure envelopes are compared with continuous ones resulting from Puck's criteria. Furthermore, the influence of microstructural imperfections is investigated systematically, and an extended version of Puck's criteria is assessed from a micro-mechanical perspective as well. In the last part of the thesis, a macroscopic model is proposed which combines Puck's criteria with localizing implicit gradient damage model. It is shown that the model provides consistent results such that the failure angle obtained at material point and the orientation of the emerging macroscopic damage band match provided that sufficiently small internal length scale parameter is used.

ÖZET

FİBERLE GÜÇLENDİRİLMİŞ ÇOK KATMANLI KIRILMANIN HASAR MEKANİĞİ İLE İNCELENMESİ

Çok ölçekli modelleme, mikromekanik ve makromekanik ölçekleri birleştirmektedir. Bu sebeple, kompleks malzemelerin özelliklerinin belirlenmesinde deneysel prosedürlere iyi bir alternatif olmaktadır. Kompozit malzemenin modellenmesi çok ölçekli modelleme konsepti için uygun bir alandır. Bu tez, fiberle güçlendirilmiş kompozitlerin kırılma mekaniğine hem mikro ölçekte hem de makro ölçekte yoğunlaşmaktadır. İlk olarak mikro ölçekli modellerde kullanılmak üzere hasar-plastisite modeli geliştirilmiş ve sonlu elemanlar programı Abaqus'e kullanıcı elemanı olarak entegre edilmiştir. Modelin ağdan bağımsız sonuçlar verdiği gösterilmiş ve model parametreleri literatürden elde edilen farklı yükleme durumlarındaki deneysel stres-gerinim eğrileri ile kalibre edilmiştir. Temsili hacim elemanları (THE) kullanılarak mikromekanik modeller oluşturulmuştur. Bu modellerde hasar-plastisite modeli ve yapışkan kontak yüzeyleri, epoksi ve epoksi-fiber arayüzlerindeki hasarı takip etmek için kullanılmıştır. Çok sayıda THE analizi yapılmış ve bunların sonuçlarıyla kesikli kırılma zarfları oluşturulmuştur. Bu kırılma zarfları Puck'ın kırılma teorisinden elde edilen sürekli kırılma zarfları ile karşılaştırılmıştır. Ayrıca, mikro ölçekteki kusurların, örneğin epoksi-fiber ayrışması gibi, etkisi sistematik bir şekilde incelenmiş ve Puck'ın geliştirilmiş kırılma teorisinin mikromekanik ölçekteki başarısı araştırılmıştır. Tezin son kısmında makromekanik ölçeğe geçilmiştir. Bu kısımda, Puck'ın kırılma teorisini ve lokalize olan örtük gradyant hasar yaklaşımını birleştirerek kompozitlerin ilerleyici kırılma analizi yapabilecek bir model oluşturulmuştur. Model Abaqus'e kullanıcı elemanı olarak entegre edilmiştir ve modelin başarısı literatürden alınan tek eksenli sıkıştırma testi ile araştırılmıştır. Modelin malzeme noktalarında tahmin ettiği kırılma açıları ve makro ölçekte görülen hasar dağılımının tutarlı olduğu anlaşılmıştır. Bu tutarlılığı sağlamak için eleman boyutunun ve içsel uzunluk ölçeğinin uygun seçilmesi gerektiği görülmüştür.

TABLE OF CONTENTS

LIST OF FIGURES

Figure **Page**

Figure **Page**

Figure **Page**

LIST OF TABLES

Table **Page**

CHAPTER 1

INTRODUCTION

Unidirectionally fiber reinforced composites have superior material properties, such as lightweightness, higher specific stiffness and strength over metal and metal alloys. Therefore, such composites have started to replace metal and metal alloys in primary structure assemblies (Deuschle and Puck, 2013; Reinoso et al., 2017) and are being used in a wide range of structural components, such as aerospace and aeronautical components, rotor blades in wind-energy systems, and automotive components. Under service loads, composite components are subjected to complicated 3D stress states (Deuschle and Puck, 2013). Therefore, reliable and efficient failure prediction under general 3D stress state is essential for the safe design of unidirectional composite components. For this purpose, over the years a number of failure criterion have been proposed.

Definition of a universal failure criteria for unidirectional composites has been a long standing challenge. Through years different failure criteria, mostly based on experimental data (Hashin, 1980; Puck, 1998) or dependent on empirical parameters (Azzi and Tsai, 1965; Tsai and Wu, 1971), have been proposed. To asses the predictive capabilities of these failure criteria and provide recommendations for academics and designers, two world wide failure exercises (WWFEs) were carried out (Kaddour and Hinton, 2012; Soden et al., 2004). In both WWFEs, failure criteria are compared and ranked based on their failure load and mode predictions. It was explicitly mentioned that none of the failure criteria are free of shortcomings (Kaddour and Hinton, 2012; Soden et al., 2004). Improvement of failure criterion requires extensive experimental verification. Unfortunately full experimental characterization under a wide spectrum of stress states is costly and more importantly it is not always possible to impose boundary conditions that would lead to the desired stress state due to difficulties associated with experimental limitations such as multi-axial loading issues and specimen geometries, (Deuschle and Puck, 2013). As far as use of failure criterion in design practice is concerned, typically satisfaction of criteria at a material point within the component/specimen is considered to be the total failure of the specimen neglecting all the remaining capacity. In case of laminated composites, neglected capacity may reach to significant levels. In fact it is the aim of this thesis to at least partially address two issues, namely,

- Assessment and characterization of failure criteria through computational micro mechanical modeling and,
- Progressive failure analysis through continuum damage mechanics

by developing and employing suitable computational modeling techniques.

As far as the first issue is concerned, computational micro-mechanical models provide an alternative perspective for analysis of heterogeneous materials. Instead of trying to predict homogenized response of the composite, micro-mechanical models resolve each phase and possibly interfaces of the heterogeneous microstructure in combination with dedicated constitutive models for different phases and interfaces. More precisely, so-called representative volume elements (RVEs), which have similar statistical characteristics in terms of geometrical features such as volume fractions and phase geometries, to real material microstructure are constructed and discretized typically by the finite element method under appropriate boundary conditions. For each phase, experimentally calibrated constitutive models are employed and the RVE is analyzed under different loading conditions from which macroscopic response is extracted through homogenization. Provided that statistical representativeness is ensured and the employed constitutive models are experimentally calibrated, the RVE based analysis of material response yield reliable results. Since all material testing is done virtually, a very wide spectrum of stress states can be realized on RVE and discrete failure envelopes can be constructed. Furthermore microstructural imperfections stemming from manufacturing process chain of composites, e.g. micro-voids, matrix-fiber interface debonding can be introduced into RVE models easily, (Ashouri Vajari et al., 2014; Jiang et al., 2019).

Regarding progressive failure analysis, among different alternatives, continuum damage mechanics has been extensively used primarily due to its clear theoretical basis and easy-to-implement structure. However as realized soon after its use in combination with finite element method, continuum damage mechanics leads to mesh dependent solution which converges to a non-physical limiting case. Therefore since then there has been a number of remedies to circumvent so-called pathological mesh dependency problem (Bažant and Oh, 1983; Peerlings et al., 1998; Voyiadjis et al., 2001, 2010). A highly effective and satisfactory remedy which has not been fully explored yet, was proposed by Poh and his co-workers, (Poh and Sun, 2017). So exploring the use of so-called localizing implicit gradient damage (LIGD) model in combination with an effective failure criteria, e.g., Puck's failure criteria, could be a valuable addition to the set of tools that can be used for progressive analysis of composites.

Referring back to the first issue, in this thesis, in Chapter 2, in order to describe the mechanical response of matrix material, a plasticity model with tension-compression yield strength asymmetry is extended with LIGD based damage model and implemented in commercial finite element program Abaqus through user element (UEL) subroutine (Systemes, 2013). Due to its non-local and coupled nature, the solution requires a three-field element formulation which is embedded in a monolithic implicit solution algorithm. The model is calibrated with experimental measurements before it is used in micro-mechanical models. In Chapter 3, statistically representative elements are constructed which employs the model presented in Chapter 2 for the matrix in combination with an elastic response for the fibers and damaging cohesive contact surfaces (interfaces) between the matrix and fibers. Different RVEs and different fiber distributions are first analyzed to assess the statistical representativeness of the RVEs. Following that, a sufficiently large number of RVE analysis under various load combinations are conducted and their results are used to construct discrete failure loci in different stress spaces. In fact here the ultimate goal is to assess the predictive capabilities of Puck' failure criteria, which is considered to be one of the most reliable failure criteria in both WWFEs (Kaddour and Hinton, 2012; Soden et al., 2004). In addition to comparison between discrete failure loci and Puck's continuous envelopes, the influence of imperfections along matrix-fiber interfaces are investigated systematically.

Switching from micro to macro-scale, in Chapter 4, the focus has been shifted to a model that embeds Puck's criteria within continuum damage mechanics. First a self-contained presentation of Puck's criteria is given including an effective search technique to identify the failure plane and angle which is central to Puck's criteria. Afterwards again LIGD formulation is exploited and exposure factors associated with Puck's criteria are used as the indicator of damage initiation and evolution. The resulting formulation is tested with a challenging compression test which fails with an inclined macroscopic failure surface. It is considered to be challenging because progressive failure analysis tools from which macroscopically observed failure orientations emerge naturally has been missing. It is shown that the proposed damage mechanics model predicts inclined macroscopic failure bands successfully that are also consistent with the predictions of Puck's criteria at material point.

The thesis is closed with major findings and merits of the current study and some comments on potential future research directions that can be pursued.

CHAPTER 2

DAMAGE-PLASTICITY MODEL FOR THE MATRIX PHASE

2.1. Introduction

The accurate prediction of the failure mechanism of uni-directional composites has been a long-standing challenge, and it is quite a complex task. There exists large number of failure criteria (Tsai and Wu, 1971, Hashin, 1980, Puck, 1998, Maimí et al., 2007). However, as demonstrated in both world wide failure exercise (WWFE) I and II (Kaddour and Hinton, 2013; Soden et al., 2004), they are not fully adequate to capture the experimental response of the composites under complex stress states. Instead of focusing on macroscopic behaviour and corresponding failure criteria, understanding the underlying micro-mechanical response could be an important step to circumvent problems associated with macroscopic failure criteria and might even contribute to improve the prediction capabilities of existing failure criterion. Uni-Directional composites consist of fiber, matrix, and fiber-matrix interfaces/interactions. The strain capacity of fiber and fiber-matrix interactions is limited, and they do not show significant non-linearity. However, until complete failure, plastic strains develop within the matrix phase and significant non-linearity is observed, (Fiedler et al., 2001; Melro et al., 2013a, 2013b). Furthermore, the response of matrix is quite different under tension and compression loads. To accurately capture the response of the Uni-Directional composites, a model that takes into account plasticity and tension-compression asymmetry is necessary. Furthermore to describe failure, the model should be extended with a reliable and objective failure modeling technique.

To address these issues, in this chapter, a plasticity model which provides all the previously mentioned properties of matrix material is extended with a mesh objective damage formulation and implemented within the commercial Finite Element software Abaqus. The objectiveness of the damage model is demonstrated and the parameters of the model are calibrated with the aid of reported experimental results.

2.2. Plasticity Model

The matrix material in uni-directional composites is pressure-dependent, shows significant non-linearity under the influence of shear load (Fiedler et al., 2001; Melro et al., 2013a), and has tension-compression asymmetry. Since it has a great impact on the accurate prediction of the failure mechanism of Uni-Directional composites, there is a vast literature for the modeling of matrix material (Totry et al., 2008; Van Der Meer, 2016). In light of the literature, it is observed that the standard non-linear material models (such as Mohr-Coulomb or Drucker-Prager) are inadequate for representing the behavior of matrix in uni-directional composites (Ghorbel, 2008; Melro et al., 2013a).

The yield surface used in this thesis is the paraboloidal yield criterion proposed by Tschoegl (Tschoegl, 1971) which captures the tension-compression asymmetry. The explicit form of yield surface of Tschoegl is given as,

$$\phi(\boldsymbol{\sigma}) = 6J_2 + 2I_1\,(\sigma_c - \sigma_t) - 2\sigma_c\sigma_t \tag{2.1}$$

where I_1 and J_2 are the first invariant of the stress tensor and the second invariant of the deviatoric stress tensor, respectively. Furthermore, σ_c and σ_t are the yield stresses for tension and compression, respectively. Furthermore, with the aid of $2I_1\,(\sigma_c - \sigma_t)$ term both pressure dependency and tension-compression asymmetry is taken into account. If the same hardening curves are assigned to σ_c and σ_t, pressure dependency and tension-compression asymmetry vanish. Consequently, Equation (2.1) reduces to the standard Von Mises yield condition. The schematic view of the yield locus in principal stress space is presented in Figure 2.5.

In the next section integration algorithm and its implementation within a finite element context is going to be elaborated. Afterwards, incorporation of damage is going to be detailed.

2.2.1. Integration Algorithm and Implementation of the Plasticity Model

Implementation of material model is carried out regarding small deformation theory (de Souza Neto et al., 2008). Thence, total strain is decomposed into elastic and

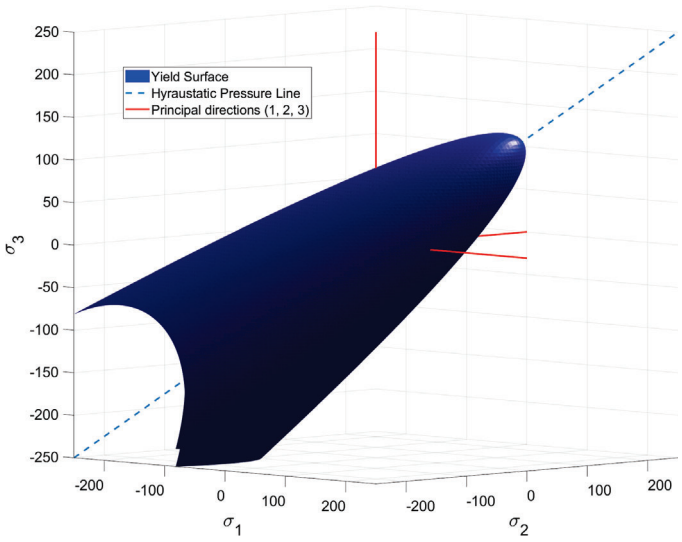

Figure 2.1. Yield locus for the plasticity model

plastic parts as,

$$\boldsymbol{\varepsilon} = \boldsymbol{\varepsilon}^{\boldsymbol{el}} + \boldsymbol{\varepsilon}^{\boldsymbol{p}} \tag{2.2}$$

where, $\boldsymbol{\varepsilon}$, $\boldsymbol{\varepsilon}^{\boldsymbol{el}}$ and $\boldsymbol{\varepsilon}^{\boldsymbol{p}}$ are total strain, elastic strain and plastic strain, respectively.

Since the problem is going to be solved incremental-iterative way by using the Newton-Raphson method, in a time discretized setting the quantities associated with time t_n are known. Furthermore, due to strain driven nature of the solution algorithm, the total strain $\boldsymbol{\varepsilon}_{n+1}$ associated with t_{n+1} is known as well. However, it is not known that if $\boldsymbol{\varepsilon}$ causes only elastic deformation or elasto-plastic deformation within the step. Thence, to capture the evolution of $\boldsymbol{\varepsilon}^{\boldsymbol{el}}$ and $\boldsymbol{\varepsilon}^{\boldsymbol{p}}$ the elastic predictor plastic corrector return mapping algorithm (Simo, 1999) is used. Therefore, the implementation of the plasticity model begins with the trial step where the response is assumed to be elastic. In the trial step, it is assumed that there is no evolution of plastic strain, and therefore plastic strain tensor $(\boldsymbol{\varepsilon}^{\boldsymbol{p}})$ is not updated and trial stress tensor $\left(\boldsymbol{\sigma}^{\boldsymbol{tr}}\right)$ is computed as follows,

$$\boldsymbol{\sigma}^{\boldsymbol{tr}}_{\boldsymbol{n+1}} = \mathbb{C}^{\boldsymbol{el}} : \left(\boldsymbol{\varepsilon}_{n+1} - \boldsymbol{\varepsilon}^{p}_{n}\right) \tag{2.3}$$

where subscripts "n" and "$n+1$" denote previous and current steps (increments), respectively. Then $\boldsymbol{\varepsilon}_{n+1}$ and $\boldsymbol{\sigma}^{\boldsymbol{tr}}_{\boldsymbol{n+1}}$ are total strain tensor and trial stress tensor at current step, respectively. Furthermore, $\boldsymbol{\varepsilon}^{p}_{n}$ is a plastic strain tensor from the previous step. Finally, $\mathbb{C}^{\boldsymbol{el}}$

is the fourth order elasticity tensor and is defined as,

$$\mathbb{C}^{\boldsymbol{el}} = 2G\,\boldsymbol{\mathcal{I}}^{\boldsymbol{sym}} + \left(K - \frac{2}{3}G\right)\boldsymbol{I} \otimes \boldsymbol{I} \tag{2.4}$$

where G and K are the shear and the bulk modulus of material, respectively. Furthermore, $\boldsymbol{I}$ and $\boldsymbol{\mathcal{I}}^{\boldsymbol{sym}}$ are second-order identity tensor and fourth-order symmetric identity tensor, respectively. In indicial notation, $\boldsymbol{\mathcal{I}}^{\boldsymbol{sym}}$ is expressed as,

$$\delta_{ijkl}^{sym} = \frac{1}{2}\left(\delta_{ik}\delta_{jl} + \delta_{il}\delta_{jk}\right) \tag{2.5}$$

Once the activation function (yield criteria) in Equation (2.1) takes non-negative values (exceeds elastic domain) then the initial assumption of elastic response becomes invalid. Therefore, plastic strain tensor in the current step $\left(\boldsymbol{\varepsilon}_{\boldsymbol{n+1}}^{\boldsymbol{p}}\right)$ must be updated. Consequently, the incremental plastic strain tensor $(\boldsymbol{\Delta\varepsilon^p})$ must be computed. Therefore Equation (2.3) is revised as,

$$\boldsymbol{\sigma_{n+1}} = \mathbb{C}^{\boldsymbol{el}} : \left(\boldsymbol{\varepsilon}_{n+1} - \boldsymbol{\varepsilon}_{n+1}^{p}\right) \tag{2.6}$$

where plastic strain tensor in the current step can be can be written as,

$$\boldsymbol{\varepsilon}_{n+1}^{p} = \boldsymbol{\varepsilon}_{n}^{p} + \boldsymbol{\Delta\varepsilon^p} \tag{2.7}$$

A non-associative plastic flow rule is utilized due to plastic compressibility and following plastic potential,

$$g = 3J_2 + \alpha p^2 \tag{2.8}$$

is used to determine the 'direction' of the incremental plastic flow. In Equation (2.9) α is material property, which controls plastic volumetric flow and described in terms of plastic Poisson's ratio, $\left(\nu_p\right)$, as $\alpha = \frac{9}{2}\frac{1-2\nu_p}{1+\nu_p}$. Furthermore, p term in Equation (2.9) is hydrostatic pressure and defined as $p = \frac{1}{3}I_1$. For the evolution of plastic strain, the flow rule,

$$\dot{\varepsilon}^{p} = \dot{\gamma}\frac{\partial g}{\partial \boldsymbol{\sigma}} = \dot{\gamma}\boldsymbol{N} \tag{2.9}$$

is used, where $\dot{\gamma}$ is the time derivative of plastic multiplier and $\boldsymbol{N}$ is the direction of plastic

flow. γ has to be consistent with Karush-Kuhn-Tucker conditions expressed as

$$\dot{\gamma} \geq 0;\ \phi \leq 0;\ \dot{\gamma}\phi = 0 \tag{2.10}$$

which simply reflects that increment in plastic flow must be non-negative and yield conditions can not be violated. In Equation (2.9) the evolution of plastic strain is defined in continuous manner. By employing backward Euler scheme, the incremental form Equation (2.9) is defined as,

$$\Delta\varepsilon^p = \Delta\gamma\ \boldsymbol{N}_{n+1} \tag{2.11}$$

where, Δ term designates increment in related quantities and $\boldsymbol{N}$ is the direction of plastic flow. The incremental plastic strain tensor, ($\boldsymbol{\Delta\varepsilon^p}$) in Equation (2.11) then takes the following form,

$$\boldsymbol{\Delta\varepsilon}^p = \gamma_{n+1}\left(3\boldsymbol{S_{n+1}} + \frac{2}{9}\alpha\,(I_1)_{n+1}\,\boldsymbol{I}\right) \tag{2.12}$$

where, γ_{n+1} is the unknown plastic multiplier; and $\boldsymbol{S_{n+1}}$ is the deviatoric part of the stress tensor.

The incremental equivalent plastic strain, $\Delta\varepsilon^p_{eq}$ is defined as

$$\Delta\varepsilon^p_{eq} = \sqrt{k\boldsymbol{\Delta\varepsilon}^p : \boldsymbol{\Delta\varepsilon}^p} \tag{2.13}$$

which is going to be used to quantify the hardening curves. In Equation (2.13), k is based on plastic Poisson's ratio and defined as $k = 1/(1 + 2\,\nu_p^2)$, which reflects the plastic compressibility of the model, (Van Der Meer, 2016).

Experimentally obtained separate hardening curves for tension and compression are used. To construct continuous curves from these discrete data points, exponential polynomials are fitted to experimental results of Fiedler (Fiedler et al., 2001). Unlike most of the literature (Melro et al., 2013a; Sun et al., 2019; Van Der Meer, 2016) different equivalent plastic strains are used to construct those polynomials. In other words, to construct tensile and compressive hardening curves, tensile equivalent plastic strain, ε^{p+}_{eq}, and compressive equivalent plastic strain, ε^{p-}_{eq}, are used, respectively. Finally, σ_t and σ_c

are defined as functions of $\left(\varepsilon_{eq}^{p+}\right)_{n+1}$ and $\left(\varepsilon_{eq}^{p-}\right)_{n+1}$ in the following exponential form,

$$\begin{aligned}\sigma_c &= a_c \exp\left(b_c \left(\varepsilon_{eq}^{p+}\right)_{n+1}\right) + c_c \exp\left(d_c \left(\varepsilon_{eq}^{p+}\right)_{n+1}\right) \\ \sigma_t &= a_t \exp\left(b_t \left(\varepsilon_{eq}^{p-}\right)_{n+1}\right) + c_t \exp\left(d_t \left(\varepsilon_{eq}^{p-}\right)_{n+1}\right)\end{aligned} \tag{2.14}$$

where a, b, c and d are fitting parameters to obtain a similar response to experimental results (positive integers) (Arefi et al., 2018); t and c denote tension and compression, respectively. In Figure 2.2 fitted curve and Fiedler's experimental curves (Fiedler et al., 2001) are presented.

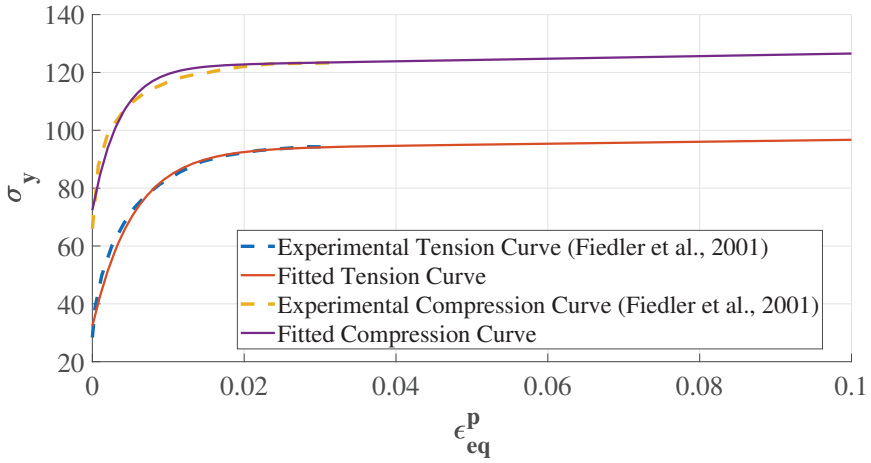

Figure 2.2. Plastic strain versus yield strength curves, experimental measurements of (Fiedler et al., 2001) and fitted curves are shown together.

Referring back to stress update algorithm and determination of γ_{n+1}, an important issue is going to be the determination of yield strength under arbitrary stress/strain states. This requires the determination of ε_{eq}^{p+} and ε_{eq}^{p-} from the plastic strain tensor at t_{n+1}. For this purpose, incremental equivalent plastic strain, $\Delta\varepsilon_{eq}^{p}$ is described in spectral form such that each eigenvalue of $\Delta\varepsilon_{eq}^{p}$ is designated as $\left(\Delta\varepsilon_{eq}^{p}\right)_i$ for $i = 1, 3$ which allows the the following expressions,

$$\Delta\varepsilon_{eq}^{p+} = \sqrt{k \sum \left(\Delta\varepsilon_{eq}^{p}\right)_i^2} \text{ if } \left(\Delta\varepsilon_{eq}^{p}\right)_i > 0 \tag{2.15}$$

$$\Delta\varepsilon_{eq}^{p-} = \sqrt{k \sum \left(\Delta\varepsilon_{eq}^{p}\right)_i^2} \text{ if } \left(\Delta\varepsilon_{eq}^{p}\right)_i < 0 \tag{2.16}$$

for incremental tensile equivalent plastic strain and incremental compressive equivalent plastic strain. Once $\Delta\varepsilon_{eq}^{p+}$ and $\Delta\varepsilon_{eq}^{p-}$ are computed, total tensile equivalent plastic strain

and total compressive equivalent plastic strain are obtained simply by,

$$\begin{aligned}\left(\varepsilon_{eq}^{p+}\right)_{n+1} &= \left(\varepsilon_{eq}^{p+}\right)_{n} + \Delta\varepsilon_{eq}^{p+} \\ \left(\varepsilon_{eq}^{p-}\right)_{n+1} &= \left(\varepsilon_{eq}^{p-}\right)_{n} + \Delta\varepsilon_{eq}^{p-}\end{aligned} \tag{2.17}$$

Due to non-linear relation between current yield strength and incremental plastic strain tensor, the determination of $\Delta\gamma$ is a non-linear problem and requires a specific solution algorithm at material/integration point.

To demonstrate solution process and the steps of implementation, an arbitrary material point between (pseudo-)time increments t_n and t_{n+1} is investigated, (Bonet and Wood, 2008; Borja, 2013; de Souza Neto et al., 2008). Since the values of variables at time t_n are known, with strain increment $\Delta\boldsymbol{\varepsilon}$, the numerical algorithm must yield updated variables at the end of the increment t_{n+1}. The updated stress tensor at the end of the increment t_{n+1} is given by,

$$\begin{aligned}\boldsymbol{\sigma_{n+1}} &= \boldsymbol{\sigma}_{n+1}^{tr} - \mathbb{C}^{el} : \Delta\boldsymbol{\varepsilon}^{p} \\ &= \boldsymbol{\sigma}_{n+1}^{tr} - \mathbb{C}^{el} : (\Delta\boldsymbol{\varepsilon} - \Delta\boldsymbol{\varepsilon}^{p})\end{aligned} \tag{2.18}$$

The last term in Equation (2.18) can also be denoted as the plastic corrector. The trial stress can be computed by freezing the plastic strain and assuming all of the strain increment is elastic. Then, the trial stress is expressed as follows,

$$\boldsymbol{\sigma}_{n+1}^{tr} = \boldsymbol{\sigma}_{n} + \mathbb{C}^{el} : \Delta\boldsymbol{\varepsilon} \tag{2.19}$$

Total incremental strain $\Delta\boldsymbol{\varepsilon}$ in Equation (2.19) can be split into deviatoric and volumetric parts $(\boldsymbol{\Delta\varepsilon}_d, \Delta\varepsilon_v)$. Consequently, deviatoric trial stress tensor, $\left(\boldsymbol{S}_{n+1}^{tr}\right)$, trial pressure $\left(P_{n+1}^{tr}\right)$, and total trial stress tensor $\left(\boldsymbol{\sigma}_{n+1}^{tr}\right)$ can be written as,

$$\begin{aligned}\boldsymbol{S_{n+1}}^{tr} &= \boldsymbol{S_n} + 2G\,\boldsymbol{(\Delta\varepsilon_d)_{n+1}} = 2G\,\boldsymbol{(\varepsilon_d)_{n+1}} \\ P_{n+1}^{tr} &= p_n^{tr} + \kappa\Delta\varepsilon_v = \kappa(\varepsilon_v)_{n+1} \\ \boldsymbol{\sigma_{n+1}^{tr}} &= \boldsymbol{S_{n+1}}^{tr} + P_{n+1}^{tr}\boldsymbol{I}\end{aligned} \tag{2.20}$$

Inserting Equation (2.12) into Equation (2.18) yields,

$$\boldsymbol{\sigma_{n+1}} = \boldsymbol{\sigma_{n+1}^{tr}} - 6G\Delta\gamma\boldsymbol{S_{n+1}} - \frac{2}{9}\kappa\alpha\Delta\gamma(I_1)_{n+1}\boldsymbol{I} \tag{2.21}$$

The stress tensor in Equation (2.21) can be split into deviatoric and volumetric parts as follows,

$$\begin{aligned} \boldsymbol{S_{n+1}} &= \boldsymbol{S^{tr}_{n+1}} - 6G\Delta\gamma \boldsymbol{S_{n+1}} \\ &= \frac{\boldsymbol{S^{tr}_{n+1}}}{1 + 6G\Delta\gamma} \\ p_{n+1} &= \bar{p}^{tr}_{n+1} - \frac{2}{3}\Delta\gamma\kappa\alpha I_1 \\ &= \frac{p^{tr}_{n+1}}{1 + 2\kappa\alpha\Delta\gamma} \end{aligned} \tag{2.22}$$

It is known that during plastic flow, the yield function, $\phi(\bar{\sigma})$, has to be zero. Since the proposed stress update algortihm has an implicit structure, by enforcing Equation (2.1) to be zero, the only unknown $\Delta\gamma$ can be determined. To do so, a simple Newton-Raphson Scheme can be used. In Newton-Raphson scheme $\frac{\partial\phi}{\partial\Delta\gamma}$ must be computed. The algorithmic structure of the local Newton-Raphson procedure at material point level is presented in Algorithm 1.

Once $\Delta\gamma$ is available, total plastic strain at t_{n+1} and in turn stress tensor σ_{n+1} can be computed. Finite element level equilibrium equations are also solved implicitly by the Newton-Raphson method. A stress update algorithm shall supply the material tangent stiffness which is basically $\frac{\partial\sigma_{n+1}}{\partial\epsilon_{n+1}}$ and can be calculated by a lengthy derivation process using the chain rule, please see Appendix for the steps of its derivation. The general structure of the stress update algorithm is given in Algorithm 2.

Before closing this section, it is important to note that very rarely, local Newton-Raphson Algorithm may converge to non-positive γ values (Van Der Meer, 2016). Since γ is ever increasing positive quantity, it is not possible for γ to take negative values. In such cases, a less accurate bi-section method is used. Consequently, positive γ values are obtained.

2.3. Incorporation of Failure

Previously mentioned plasticity models tends to yield indefinitely increasing stress values. Such response is physically unrealistic and failure has to be taken into account. This incorporation can be realized by using fracture mechanics based approaches or continuum damage mechanics based approaches. In case of fracture mechanics based approaches, a discontinuity must be included into the kinematics. Consequently, with formation

Algorithm 1 Local Newton Raphson Algorithm

WHILE DIFF>TOL **and** iternum < itermax

• Calculate $\triangle\boldsymbol{\varepsilon^p}$, $\triangle\varepsilon^p_{eq}$, $\varepsilon^{p,n+1}_{eq}$ and ϕ_{cur} with respect to γ_{cur}

• Update stresses σ_t, σ_c

• Compute $\dfrac{\partial\phi}{\partial\gamma}$

• Update γ, $\gamma_{next} = \gamma_{cur} - \dfrac{\partial\phi}{\partial\gamma}$

IF$\gamma_{next} < 0.0$

• Go to bi-section algorithm.

ELSE

• Using γ_{cur} calculate $\Delta\boldsymbol{\varepsilon^p}$, $\Delta\varepsilon^p_{eq}$, $\varepsilon^{p,n+1}_{eq}$ and ϕ_{cur}

• $DIFF = \phi_{next} - \phi_{cur}$

• iternum = iternum + 1

ENDIF

ENDWHILE

Algorithm 2 Implementation of Elasto-Plastic Material Model

• Read Solution Dependent Variables (SDV)

• Read Material Properties (PROPS)

Elastic Predictor

• Update Strain

• Compute trial stress $\left(\sigma^{tr}_{n+1}\right)$

• Compute yield function $\left(\phi^{tr}_{n+1}\right)$

IF$\phi^{tr}_{n+1} < 0$

• Material Tangent $\leftarrow \mathbb{C}^{el}$

• $\sigma_{n+1} \leftarrow \sigma^{tr}_{n+1}$

• $SDV_{n+1} \leftarrow SDV_n$

ELSE

Plastic Corrector

• Compute γ_{n+1} by local Newton Raphson

IF$\gamma_{n+1} < 0$

Use bi-section algorithm

ENDIF

• Update Plastic strain

• Update Stress

• Compute and Update Consistent Tangent Modulus $\mathbb{C}^{ep}$ (Please see Appendix)

• Update SDV

ENDIF

of multiple cracks or with the coalescence of cracks computational cost of the fracture mechanics based models increase dramatically. On the other hand, continuum damage mechanics based approaches can be embedded into current finite element frameworks rather easily. Therefore, in this study continuum damage mechanics based approach is used.

In continuum damage mechanics, the effect of cracks are reflected by means of a damage variable D takes the initial value of zero and grows until unity with further loading and evolution of damage at the material point. Therefore in its simplest form, stress response is obtained by $(1-D)\,\sigma$ where σ is the undamaged elastic response of the material. Although its simple conceptual form, continuum damage mechanics in its local form results in non-physical response. To demonstrate this, a uni-axial tension specimen with a varying cross-section is discretized by a number of different element sizes as shown in Figure 2.3. Assuming a stress based damage initiation criteria, the initiation of damage is expected in the narrowest section (in this case in the element with the smallest cross-section) and deformation localizes within a single element upon further loading. The total energy dissipation is controlled by the critical element size and upon mesh refinement diminishing dissipation values are obtained, please see the force-displacement graphs shown in Figure 2.3. In the limit of further mesh refinement, this simple example suggests that dissipation would approach to zero. Since damage corresponds to a cracking process and creation of new surfaces, the dissipated energy cannot be zero. This problem is called as pathological mesh dependency problems, (Geers et al., 2000). Crack Bandwidth Approach (Bažant and Oh, 1983), integral type non-local models (Voyiadjis et al., 2001, 2010) and Gradient Enhanced Models (Jirasek, 1998, Geers et al., 2000) are some of the remedies for the pathological mesh dependency problem. Even the mesh dependency problems may be solved with those models, there are still some inconsistencies about the initiation and the distribution of the damage (Sarkar et al., 2019). An effective remedy to both mesh dependency problems and inconsistencies about damage distribution is proposed by Poh (Poh and Sun, 2017) and called as Localizing Implicit Gradient Damage Model (LIGD) due to its resemblance to conventional implicit gradient damage (CIGD) method.

Both CIGD and LIGD resolves mesh dependency problem by introducing a physical averaging domain, which does not depend on the discretization, namely, the internal length scale l_c, (Poh and Sun, 2017). This introduces a non-locality to the response and solves the mesh dependency problem effectively by acting as a localizer limiter. The

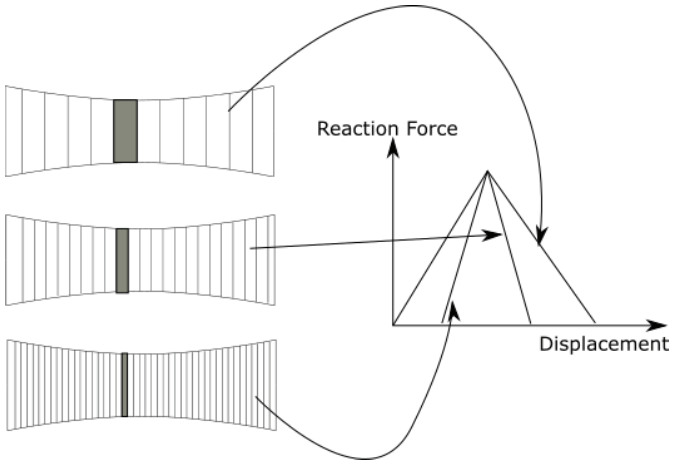

Figure 2.3. Material response changes significantly with mesh refinement.

domain size controlled by l_c is called as interaction domain and in case of CIGD, it stays constant throughout the localization process. However, as seen from Figure 2.4, such interaction domain reduces due to weakening of interactions between micro-cracks and material failure is localized to a narrower zone as compared to initial interaction domain.

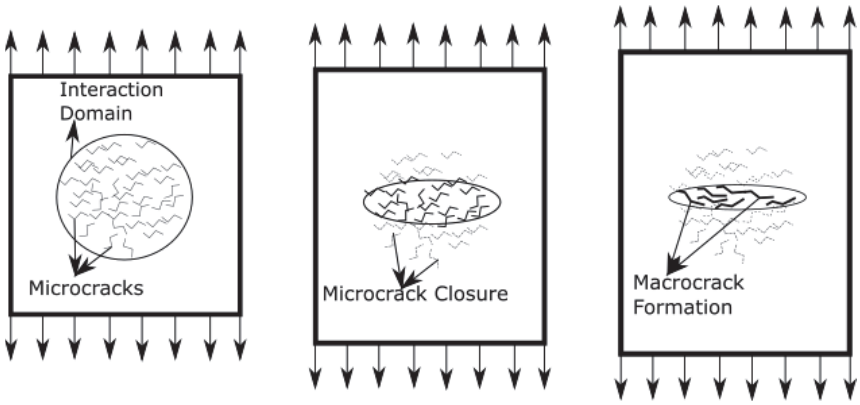

Figure 2.4. Schematic presentation formation of macrocrack from diffused network of microcracks with decreasing non-local interaction domain as damage progresses

Since this change in the interaction domain is disregarded, some inconsistencies exist in CIGD for the initiation and evolution of damage (Poh and Sun, 2017). In the study of Poh (Poh and Sun, 2017; Sarkar et al., 2022), such inconsistencies are solved by changing the constant nature of the internal length scale which is consistently done by introducing interactions between micro and macro processes. The resulting damage formulation is called as Localizing Implicit Gradient Damage (LIGD) model. Borrowing some ideas from higher order continuum theories, LIGD formulation results in a framework that is thermodynamically consistent for elasticity coupled with damage. The distribution of

non-local equivalent strain is governed by the following equation

$$\bar{\varepsilon} - \varepsilon = \nabla \cdot \left(g \, l_c^2 \nabla \bar{\varepsilon} \right) \tag{2.23}$$

which is obtained by following the Coleman-Noll procedure. In Equation 2.23, g is the interaction function that depends on damage and the following form

$$g = \frac{(1 - R) \exp(\eta D) + R - \exp(-\eta)}{1 - \exp(-\eta)} \tag{2.24}$$

has been successfully used where, η and R are model properties reflecting the nature of the interactions as damage grows. η describes the reduction rate in interaction. Also, the other parameter R, is called the residual interaction parameter. It is worthy to note that when interaction function is set to unity, CIGD model is recovered, (Sarkar et al., 2019).

Referring back to plasticity, it is plausible to expect that with physical damage mechanisms taking place at the micro level, the yield strength of material would drop. Therefore a shrinkage in yield surface could be a viable way of accounting for damage. In this thesis, the effect of damage is described by reducing the yield surface which was also used for both J2 type plasticity and crystal plasticity models, (Engelen et al., 2003). To give an insight, in Figure 2.5 yield loci with and without damage are presented. In Figure 2.5 blue surface represents the undamaged yield surface and red surface represents the damaged one. Since a distinction between tensile and compressive response is considered,

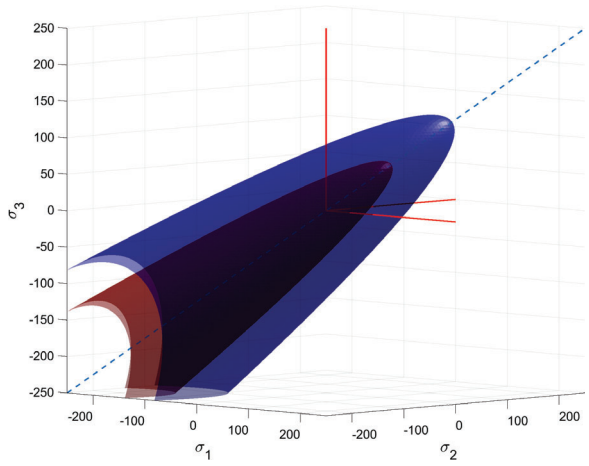

Figure 2.5. Elastic domain for undamaged (blue) and damaged (red) material.

two damage variables, namely D^t and D^c are introduced. Therefore, current yield strength

values σ_t and σ_c are obtained from the initial undamaged ones $\bar{\sigma}_t$ and $\bar{\sigma}_c$ as,

$$\begin{aligned} \sigma_t &= \left(1 - D^t\right) \bar{\sigma}_t \\ \sigma_c &= \left(1 - D^c\right) \bar{\sigma}_c \end{aligned} \tag{2.25}$$

The initiation and evolution of damage is proportional with plastic deformation. Therefore it is reasonable to link evolution of damage variables to equivalent plastic strains. However, to avoid mesh dependency problems, non-local equivalent plastic strain fields $\hat{\varepsilon}_{eq}^{p+}$ and $\hat{\varepsilon}_{eq}^{p-}$ for tension and compression are introduced, respectively. Adapting the LIGD formulation directly, the distribution of non-local equivalent plastic strain fields are governed by the following Helmholtz type equations,

$$\begin{aligned} \bar{\varepsilon}_{eq}^{p,\,+} - \nabla \cdot \left(g\, l_c^2 \nabla \bar{\varepsilon}_{eq}^{p,\,+} \right) &= f\left(\boldsymbol{\sigma}\right) \varepsilon_{eq}^{p,\,+} \\ \bar{\varepsilon}_{eq}^{p,\,-} - \nabla \cdot \left(g\, l_c^2 \nabla \bar{\varepsilon}_{eq}^{p,\,-} \right) &= f\left(\boldsymbol{\sigma}\right) \varepsilon_{eq}^{p,\,-} \end{aligned} \tag{2.26}$$

and complemented by Neumann type boundary conditions,

$$\begin{aligned} \nabla \bar{\varepsilon}_{eq}^{p,\,+} \cdot \mathbf{n} &= 0 \\ \nabla \bar{\varepsilon}_{eq}^{p,\,-} \cdot \mathbf{n} &= 0 \end{aligned} \tag{2.27}$$

where $\mathbf{n}$ is the outward normal vector of the boundary. As seen from Equation (2.26) $f\left(\boldsymbol{\sigma}\right)$ term is used as multiplier for local damage driving terms. In case of tensile tri-axiality an acceleration in damage evolution is expected. On the contrary, in case of compressive tri-axiality evolution of damage must be hindered (Asp et al., 1996; Chevalier et al., 2016; Fiedler et al., 2001; Nguyen et al., 2016). In order to capture these effects in a continuum setting, $f\left(\boldsymbol{\sigma}\right)$ is introduced and defined as,

$$f\left(\boldsymbol{\sigma}\right) = 1 + \left(\frac{\sigma_H}{||\boldsymbol{\sigma}||} \right) \tag{2.28}$$

where σ_H is the hydrostatic stress, i.e. $\sigma_H = 1/3\left(\sigma_{xx} + \sigma_{yy} + \sigma_{zz}\right)$. Norm of the stress tensor $||\boldsymbol{\sigma}||$ is used to normalize and convert it in a non-dimensional form.

2.4. Implementation of the Damage-Plasticity Model

The presented damage-plasticity model involves solution of three coupled differential equations which are

$$\begin{aligned} \nabla \cdot \boldsymbol{\sigma} &= \mathbf{0} \\ \bar{\varepsilon}_{eq}^{p,+} - \nabla \cdot \left(g l_c^2 \nabla \bar{\varepsilon}_{eq}^{p,+} \right) &= f\left(\boldsymbol{\sigma}\right) \varepsilon_{eq}^{p,+} \\ \bar{\varepsilon}_{eq}^{p,-} - \nabla \cdot \left(g l_c^2 \nabla \bar{\varepsilon}_{eq}^{p,-} \right) &= f\left(\boldsymbol{\sigma}\right) \varepsilon_{eq}^{p,-} \end{aligned} \tag{2.29}$$

which are complemented with boundary conditions. Weak forms of these equations are obtained by employing weighted residual technique. A monolithic solution algorithm is preferred and a user element is developed that is integrated in finite element solver Abaqus. An 8-noded element with brick topology is developed that has 5 degrees of freedom per node. The first three degree of freedoms are related to the displacements in x-, y- and z-directions, respectively. The fourth and fifth degree of freedoms are related to tension non-local solution variable, $\left(\hat{\varepsilon}_{eq}^{p+}\right)$, and compression non-local solution variable, $\left(\hat{\varepsilon}_{eq}^{p-}\right)$, respectively. The implemented user element is similar to Abaqus' Coupled Temperature displacement elements (C3D8T).

Since post-processing module of Abaqus does not support user elements, Abaqus' C3D8T elements are used as 'host' elements for post-processing purposes. The mesh is dublicated such that C3D8T elements and user elements share the same coordinates and connectivity. During the analysis User Elements' integration point data are copied to a Common Block. Afterward, using Abaqus UVARM (user defined variable) subroutine, data in Common Block is copied to Abaqus C3D8T elements so that the results of User Elements can be viewed in Abaqus post-processor. Since the resulting coupled partially differential equations are solved by Newton-Rapahson method, internal force columns resulting from the weak form and consistent tangent operators resulting from the consistent linearization are presented in Appendix. Algorithmic details of the stress update and User Element Implementation are given in Algorithm 3 and Algorithm 4, respectively.

Algorithm 3 Stress Update Algorithm

• Read History Variables Material properties
• Check for damage initiation & evolution
IF$\bar{\kappa}^{+,\,-}_{n+1} \geq \bar{\kappa}^{+,\,-}_{n}$
• Check for damage evolution
• Update Damages
ELSE
• $D^{+,\,-}_{n+1} \leftarrow D^{+,\,-}_{n}$
ENDIF
• Calculate trial values
• Update $\sigma_{t,c}$
• Calculate Φ^{tr}_{n+1}
IF $\Phi^{tr}_{n+1} < 0.0$
• $(.)_{n+1} \leftarrow (.)^{tr}_{n+1}$
• Update element tangent: $\dfrac{\partial \sigma_{n+1}}{\partial \bar{\kappa}_{n+1}}, \dfrac{\partial \sigma_{n+1}}{\partial \boldsymbol{\varepsilon}_{n+1}}, \dfrac{\partial \varepsilon^{eq}_{p}}{\partial \bar{\kappa}_{n+1}}, \dfrac{\partial \sigma_{n+1}}{\partial \boldsymbol{\varepsilon_p}_{n+1}}$
ELSE
• Compute $\Delta\gamma$
• Update local equivalent plastic strain ε^{eq}_{p}
• Update Plastic strain $\boldsymbol{\varepsilon_p}_{n+1}$
• Compute positive local plastic strain $\left(\varepsilon^{pl,+}_{eq,\,n+1}\right)$ and negative local plastic strain $\left(\varepsilon^{pl,-}_{eq,\,n+1}\right)$
• Update Stress
• Update element tangent: $\dfrac{\partial \sigma_{n+1}}{\partial \varepsilon^{pl,+}_{eq,\,n+1}}, \dfrac{\partial \sigma_{n+1}}{\partial \varepsilon^{pl,-}_{eq,\,n+1}}, \dfrac{\partial \sigma_{n+1}}{\partial \boldsymbol{\varepsilon}_{n+1}}, \dfrac{\partial \varepsilon^{pl+}_{eq}}{\partial \boldsymbol{\varepsilon}_{n+1}}, \dfrac{\partial \varepsilon^{pl-}_{eq}}{\partial \boldsymbol{\varepsilon}_{n+1}}, \dfrac{\partial \sigma_{n+1}}{\partial \boldsymbol{\varepsilon_p}_{n+1}}$
ENDIF

2.5. Assessment of the Model

Before using the material model in micro-mechanical analysis, the material properties are calibrated through experimental results of Fiedler (Fiedler et al., 2001) and compared with the predictions of the model proposed by Melro (Melro et al., 2013a). For this purpose, firstly the mesh objectivity of the model and effectiveness of LIGD formulation is investigated. Afterward, the response of material model is calibrated by using uni-axial tension and uni-axial compression test results. Once good correlation with experimental results is obtained, then without changing any material parameter, the prediction capabilities of the material model is investigated by considering a torsion test.

Algorithm 4 Abaqus Element Implementation

Loop over integration points:

- Calculate element matrices: $\boldsymbol{N}$, $\boldsymbol{B}$, $\bar{\boldsymbol{N}}$, $\bar{\boldsymbol{B}}$, Jacobian
- Transform Nodal values to integration points
- Call stress update algorithm
- Update history variables
- Copy integration point data from User Elements to Dummy Element
- Compute Internal Force Column (Please see Appendix)
- Compute Element Stiffness Matrix (Please see Appendix)

2.5.1. Mesh Objectivity of the Model

To present the mesh objectivity of the material model implementation, the specimen in Figure 2.6 (Fiedler et al., 2001) is discretized with different element sizes of 0.250, 0.350 and 0.500 mm which are designated as fine mesh, medium mesh and coarse mesh, respectively. To reduce the computational costs $\frac{1}{8}$ of the model is used and symmetry boundary conditions are applied (Figure 2.7) and uni-axial tensile displacement is applied as shown in Figure 2.7. Upon completion of the analysis, displacement versus reaction force diagram for each discretization are gathered and compared in Figure 2.8. As far as reaction force-displacement response is concerned, this curve confirms that the results are mesh objective.

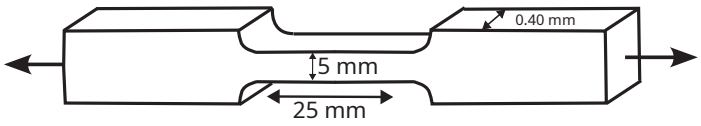

Figure 2.6. Dimensions of the specimen

In Figure 2.9, the distribution of tension damage at the end of the analysis for each discretization is presented. Even thought the mesh sizes are different, the damage localizes into similar volumes in each discretization. This volume is described by the internal length scale parameter (Please check Section 2.3); and does not depend on the discretization of the model. Hence, with the implementation the mesh objectivity of the damage distribution is provided.

As a consequence of the constant nature of the internal length scale parameter, damage zone artificially widens in CIGD model. In Figure 2.10 and Figure 2.11, damage distributions obtained by LIGD and CIGD at different instants are presented, respectively. As seen from Figure 2.11, in case of CIGD the damage zone tends to artificially widens

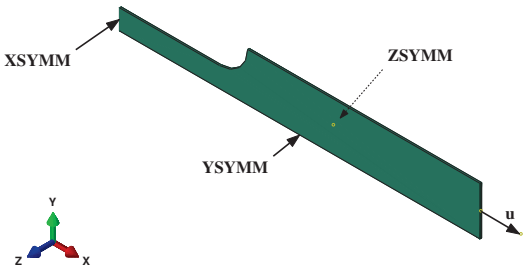

Figure 2.7. Boundary conditions of the specimen

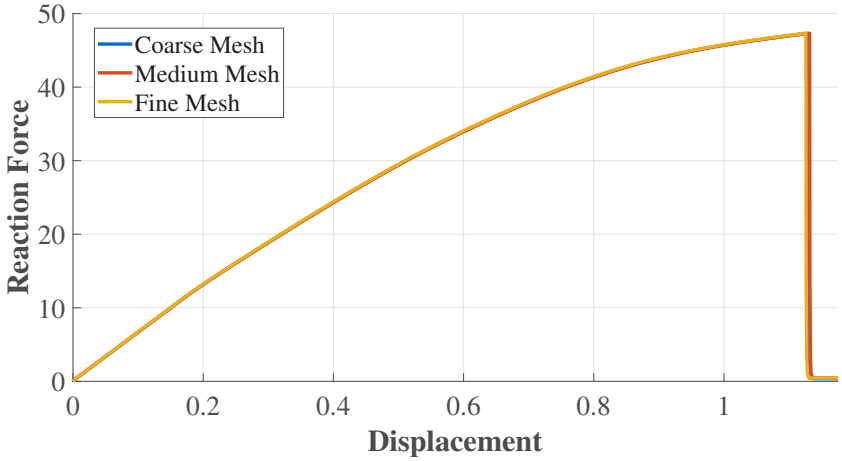

Figure 2.8. Displacement vs. Reaction Force diagrams for coarse (0.500 mm), medium (0.375 mm) and fine (0.250 mm) mesh models

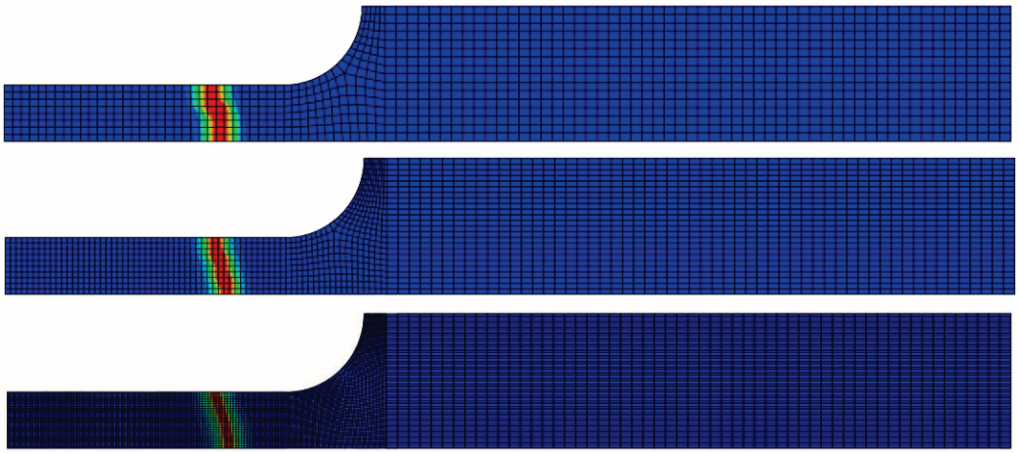

Figure 2.9. Distribution of damage for the mesh sizes of 0.500, 0.375 and 0.250 mm

with further deformations. However, in the case of LIGD model damage zone localizes into a narrow band (Figure 2.10). Hence, with the material model implementation the artificial widening of damage zone is prevented.

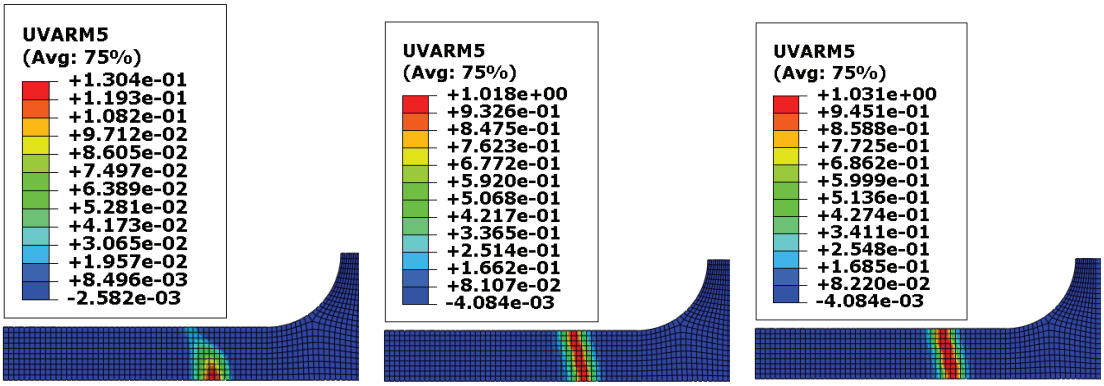

Figure 2.10. Step-by-step evolution of damage for LIGD Model

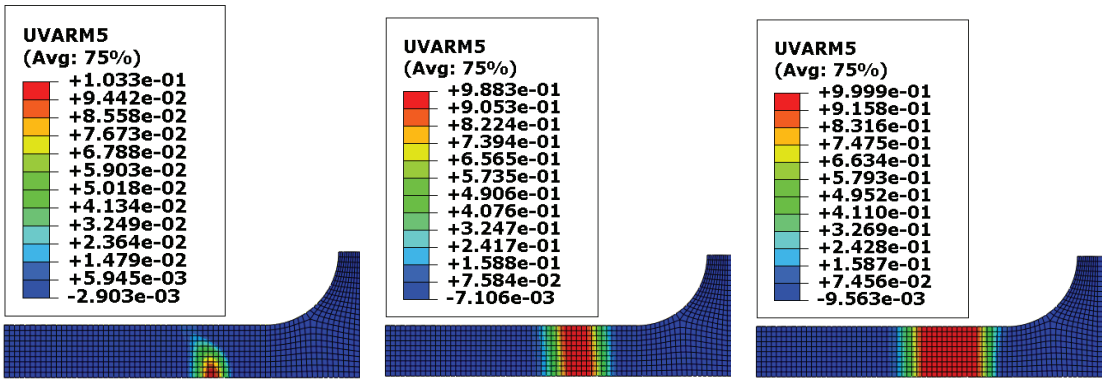

Figure 2.11. Step-by-step evolution of damage for CIGD Model

2.5.2. Calibration of the Model

For the purpose of model calibration, experimental results of Fiedler (Fiedler et al., 2001) are used. Firstly uni-axial tension specimen presented in Figure 2.6 is modeled. To reduce the computational cost symmetry boundary conditions are applied; and $\frac{1}{8}$ of the specimen is modeled. The boundary conditions and the discretization of the model are presented in Figure 2.7. The material properties used throughout the verification process are presented in Table 2.1.

The distribution of non-local tension equivalent plastic strain, $\bar{\varepsilon}_{pl}^{eq+}$, and tension damage, D^{+}, at the end of the analysis are presented in Figure 2.12 and Figure 2.13, respectively. Failure pattern obtained from uni-axil tension test of Fiedler's work (Fiedler et al., 2001) is also presented in Figure 2.14. By comparing those figures, it is observed that the implementation predicts failure pattern accurately.

The averaged strain stress diagrams from the material model implementation and Fiedler's experimental study are compared in Figure 2.15. As seen from Figure 2.15, in

Table 2.1. Material properties

E (MPa)	ν	ν_p	β^+	β^-	η	R	κ_i^+	κ_i^-
3760	0.33	0.39	5	7	1	0.005	2.5×10^{-2}	15×10^{-2}

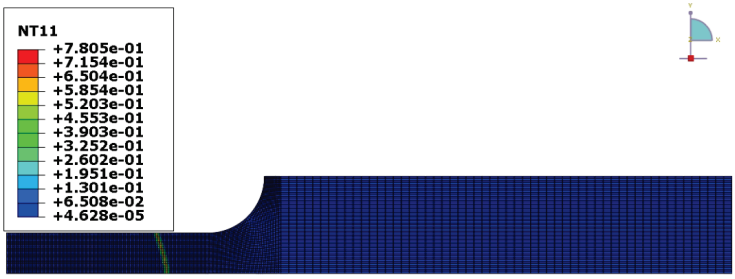

Figure 2.12. Distribution of non-local positive equivalent plastic strain

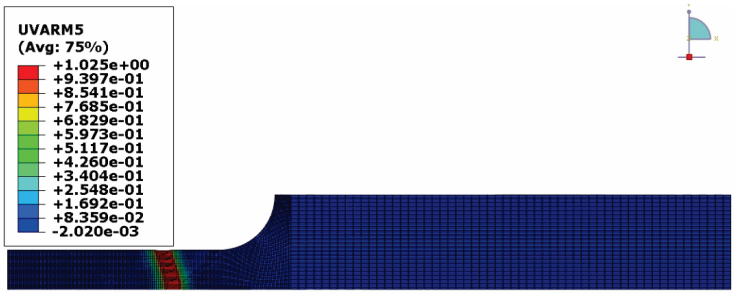

Figure 2.13. Distribution of tension damage

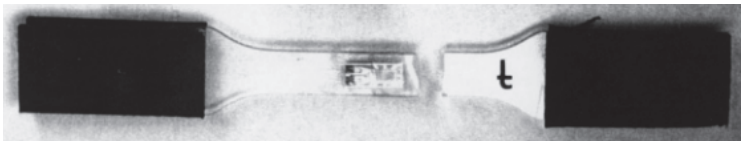

Figure 2.14. Experimental result from Fiedler (Fiedler et al., 2001)

both cases significant amount of non-linearity is observed. Furthermore, curves for each study are almost coincident up to the softening point. In Fiedler's study an abrupt failure is obtained without any softening. However, in the implementation exponential softening is observed. Nevertheless, with the implementation typical response characteristic of epoxy material is captured (Fiedler et al., 2001; Melro et al., 2013b; Van Der Meer, 2016).

To investigate the accuracy of the material model implementation under uni-axial compression load, the cube specimen in Figure 2.16 is modeled, and analyzed. The dimensions of the specimen are presented in Figure 2.16a. To reduce the computational cost symmetry boundary conditions are applied, and $\frac{1}{8}$ of the specimen is modeled (Figure 2.16b). Similar to experimental study (Fiedler et al., 2001), the displacement is applied by means of a rigid plate. For this purpose a rigid plate is placed on top of the specimen (Figure 2.16b). Afterward an interaction between specimen and the rigid plate is defined.

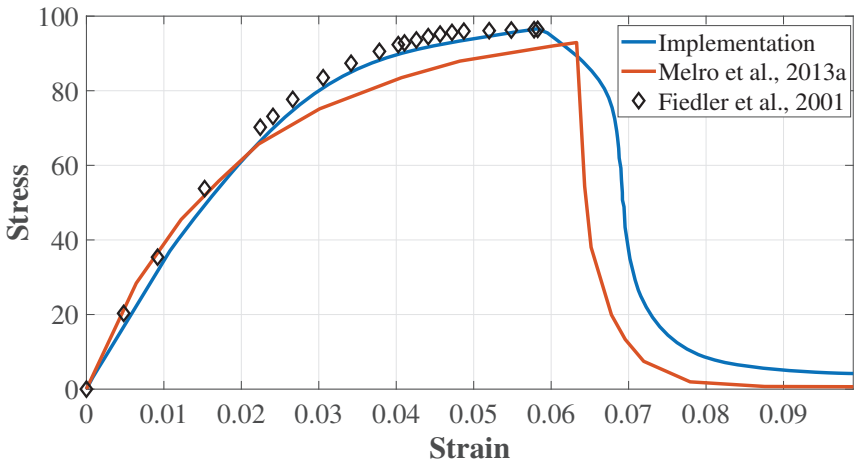

Figure 2.15. Strain vs. Stress curve for tension specimens

Finally, displacement is applied to rigid plate; and analysis is conducted. The configuration of the numerical model is presented in Figure 2.16b.

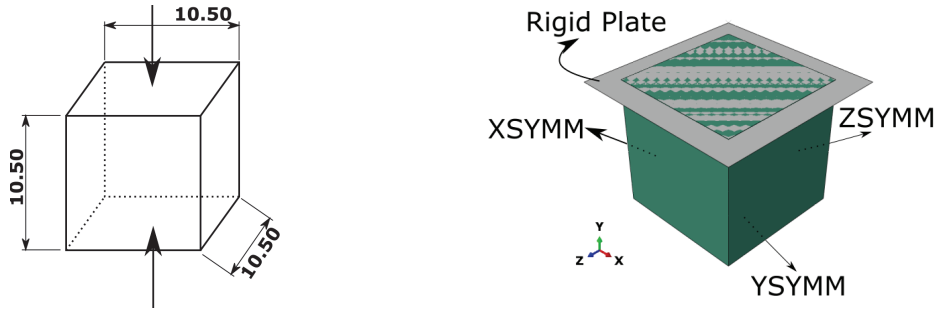

(a) Dimensions of the specimen

(b) Boundary conditions of the specimen

Figure 2.16. Dimensions and Boundary Condition details for compression specimen

The distribution of the compression non-local equivalent plastic strain and the distribution of the compression damage at the end of the analysis are presented in Figure 2.17 and Figure 2.18, respectively. As seen from Figure 2.17 and Figure 2.18, both the distribution of the compression non-local equivalent plastic strain and the distribution of the damage are localized into a band with an inclination. Typical epoxy resins fail with the formation of localized shear bands (Fiedler et al., 2001; Melro et al., 2013a). In Figure 2.18 such localized shear band is observed. From this perspective, the damage distribution predictions from the implementation is accurate; and in a good agreement with experimental studies (Fiedler et al., 2001).

In Figure 2.19, strain vs. stress diagrams from the current model and the experimental results from Fiedler (Fiedler et al., 2001) are compared. As seen from Figure

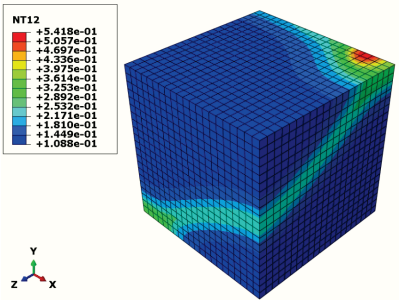

Figure 2.17. Distribution of the compression non-local equivalent plastic strain $\bar{\varepsilon}_{eq}^{p,-}$

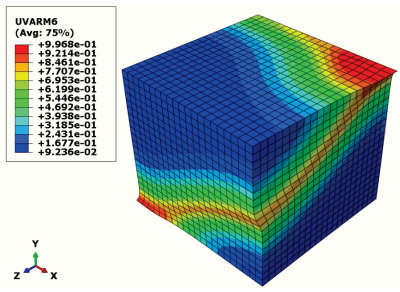

Figure 2.18. Distribution of the compression damage D^{-}

2.19 significant non-linearity is observed for the compression loading. Actually, almost a plateau of perfect plasticity is obtained after the initiation of the non-linear behavior. In Fiedler's experimental study an abrupt failure is achieved with very large strain value around 70% (Fiedler et al., 2001). Since the implementation is based on small strain theory, such large strain levels are not within the scope of the model. In the current model, failure is initiated when the compressive non-local equivalent plastic strain value reaches to 0.15. Total strain-stress response for the implementation is presented in Figure 2.19. As seen from the Figure 2.19, curves from the implementation and the experimental results are coincident until the strain value of 0.25. However, after this point two curves start to deviate. It is worthy to note that the predictions of the current model covers a larger strain range as compared to the model proposed by Melro. Furthermore, the ultimate goal is to employ this model in micro-mechanical models (please see next Chapter) which have almost always a heterogeneous stress state and which fails under combined state of stress at much lower strain levels.

To investigate the shear response of the implementation, a torsion specimen (Fiedler et al., 2001) is modeled. In this model, displacement are applied by means of coupling constraints. For this purpose coupling constraints between face and reference point are defined (Figure 2.20a). Afterward, rotation about Y axis is applied to those reference points. The dimensions and boundary conditions of the specimen are presented in Figure

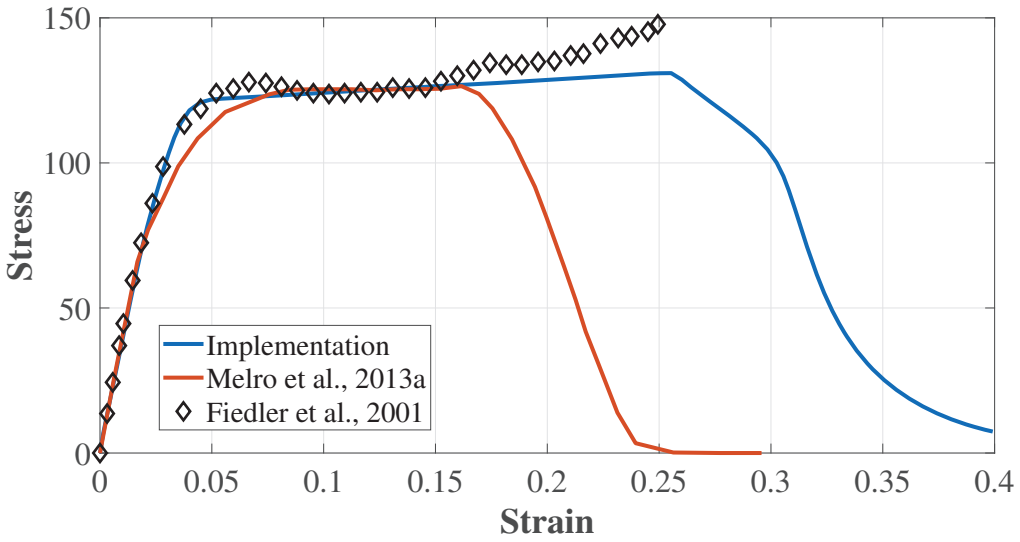

Figure 2.19. Strain vs. Stress curve for compression specimens

2.20.

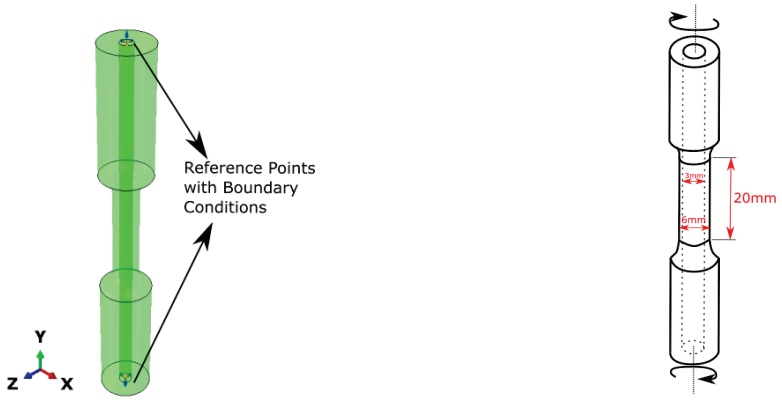

(a) Boundary conditions of the specimen (b) Dimensions of the specimen

Figure 2.20. Dimensions and Boundary Conditions details for torsion specimen

In Figure 2.21 the distribution of the tension damage at the end of the analysis is presented. As seen from the figure damage is accumulated in the middle section of the specimen and have an inclination of approximately $45°$.

In Figure 2.22, strain stress diagrams for the torsion specimen and experimental study of Fiedler (Fiedler et al., 2001) are presented. By investigating Figure 2.22, it is also observed that up to the very large strain values of around 0.50 both curves are almost overlapping. The presented model captures the experimental behaviour very closely.

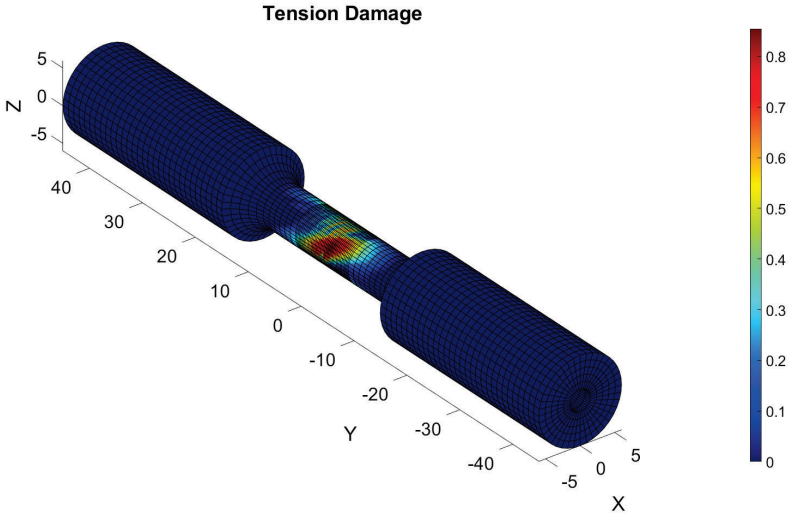

Figure 2.21. Distribution of tension damage obtained from Matlab

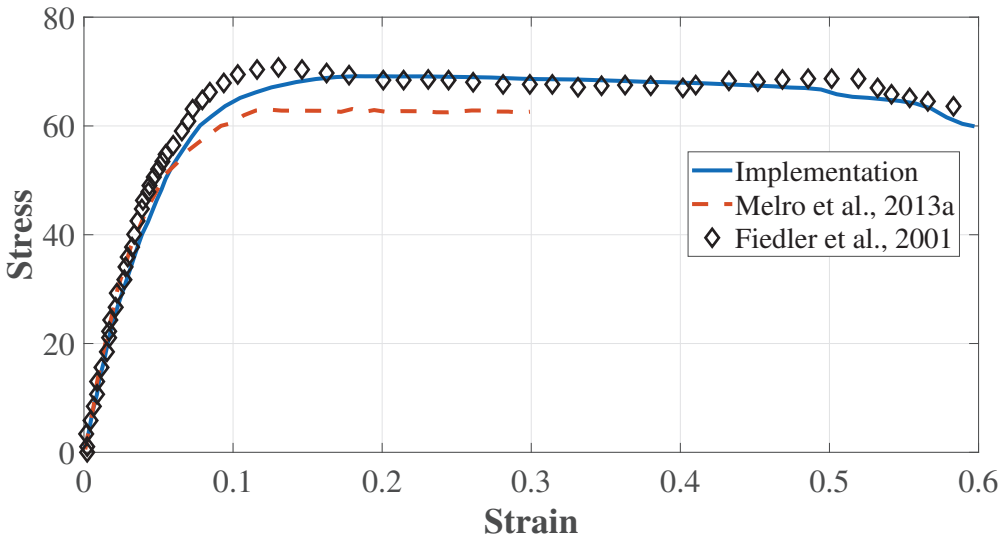

Figure 2.22. Strain vs. Stress curve for torsion specimens

2.6. Results and Discussion

In this chapter, a plasticity model is implemented and afterwards extended by using the Localizing Implicit Gradient Damage formulation. The extended framework is implemented in commercial Finite Element software Abaqus. For this purpose an eight noded brick element is implemented to Abaqus through User Element (UEL) subroutine. After the implementation of user element is completed, firstly the mesh objectivity of model is verified. Afterward, the artificial widening of damage band is investigated. For this purpose, same tension specimen is analyzed by LIGD and CIGD formulations. After comparing the damage distribution for each analysis (Figure 2.10 and Figure 2.11), it is

concluded that artificial widening of damage problem is almost completely avoided with LIGD model.

Once the mesh objectivity of the implementation is proved, calibration of the model parameters is considered to be the next task. For this purpose, tension and compression test data are used for calibration and torsion test results are used for validation. In other words, the identified set of parameters by means of tension and compression test results are fixed and the torsion test results are reproduced numerically. From the comparison, it is concluded that the model can be considered very good for tension and shear tests. In case of compression, very large strains are reached before failure in experiments. However, as mentioned before, in case of complex stress states (which are typically observed in micromechanical models), the failure occurs at much lower strain levels. Therefore the presented model is sufficient for the purpose of next chapter.

CHAPTER 3

COMPUTATIONAL MICRO-MECHANICAL MODELING

3.1. Introduction

Due to their heterogeneous micro-structure, failure mechanics of FRP composites is rich in failure modes that are controlled primarily by complex stress state at micro-structural level. Furthermore, manufacturing process chain of composites made them vulnerable to emergence of manufacturing defects, e.g., micro-voids and imperfect matrix-fiber interfaces, (Ashouri Vajari et al., 2014). Therefore determination of failure envelopes particularly under complex stress states with inherent uncertainties is a challenging task. To this end, a number of phenomenological failure criteria have been proposed and used for design purposes, (Azzi and Tsai, 1965; Davila et al., 2005; Hashin, 1980; Puck, 1998; Tsai and Wu, 1971). To assess the predictive capabilities of these models, world-wide-failure exercises (WWFE) (Kaddour and Hinton, 2013; Soden et al., 2004), have been conducted which provided a reference on the performance of different criteria and particularly their weaknesses. However, it is worthy to note that physical response of the test specimen under certain stress states could not have been investigated due to experimental difficulties associated with the imposition of required boundary conditions. This in turn implies that by physical testing it is not possible to cover the whole spectrum of stress states and validate failure envelopes under arbitrary loading conditions. To address this shortcoming, computational micro-mechanical modeling has been used successfully in a number of studies, see for example (Herraez et al., 2015; Naya et al., 2017; Romanowicz, 2014; Sun, Meng, et al., 2018) and arises as a promising tool that can effectively be used to complement physical testing. However, for this purpose, reliable and calibrated material models for different phases and interfaces are essential. Computational micro-mechanical modeling framework provides flexibility regarding the imposition of boundary conditions and also allows one to incorporate micro-structural imperfections in a controlled manner.

To this end, in this chapter, three-dimensional representative volume element (RVE) based micro-mechanical models are constructed and analyzed. RVE models consist of matrix, fibers embedded in matrix and fiber-matrix interfaces. Plasticity-damage

model presented in Chapter 2 is used for the matrix phase and meanwhile the fibers are assumed to stay within the elastic range. For the failure of matrix-fiber interfaces, cohesive contact surfaces technique available in Abaqus are used due to their flexibility and robust performance even under compressive tractions and closure of cracks/openings. Two RVEs of different sizes are used and a sufficient number of analysis are conducted to construct failure envelopes which are compared with corresponding curves of the Puck's criteria. A systematic analysis on the influence of matrix-fiber interface imperfections is carried out as well in order to find the threshold above which failure envelopes become insensitive to any further imperfections. Apart from the resulting discrete failure envelopes, RVE analysis have also been used to investigate the significance and consistency of phenomenological parameters of Puck's model such as η_{w1} which was introduced in the extended version (Knops, 2008) to capture the influence of out-of-plane normal stress on failure envelope.

In the next section, constitutive models for fiber phase and matrix-fiber interfaces are introduced separately. Thereafter general lay-out of RVE analysis framework including the imposition of boundary conditions at RVE level and extraction of mascroscopic stress response, is presented. Analysis results and comparison of discrete failure criteria are presented in the same section including a critical assessment. Significance of these results are reiterated in the conclusion and outlook section including some pointers for future research directions.

3.2. Computational Micro-mechanical Model

Micro-mechanical models are very instrumental to investigate the influence of different micro-structural parameters on macroscopic properties. In combination with physically based, calibrated models for individual phases and interfaces, micro-mechanical models are very flexible to realize multi-axial stress states, which may require sophisticated set-ups and control systems in case of physical experimentation. Furthermore, such models are also very valuable to assess the capabilities and limitations of commonly used failure criteria.

Geometrically, a statistically representative (in terms of fiber shape, fiber volume fraction and distribution) and computationally feasible domain is in fact the essence of the micro-mechanical modeling approach. Determination of the size of the so-called representative volume elements (RVEs) is a delicate task and typically requires a number of analysis with increasing RVE sizes. Furthermore, boundary conditions imposed on the

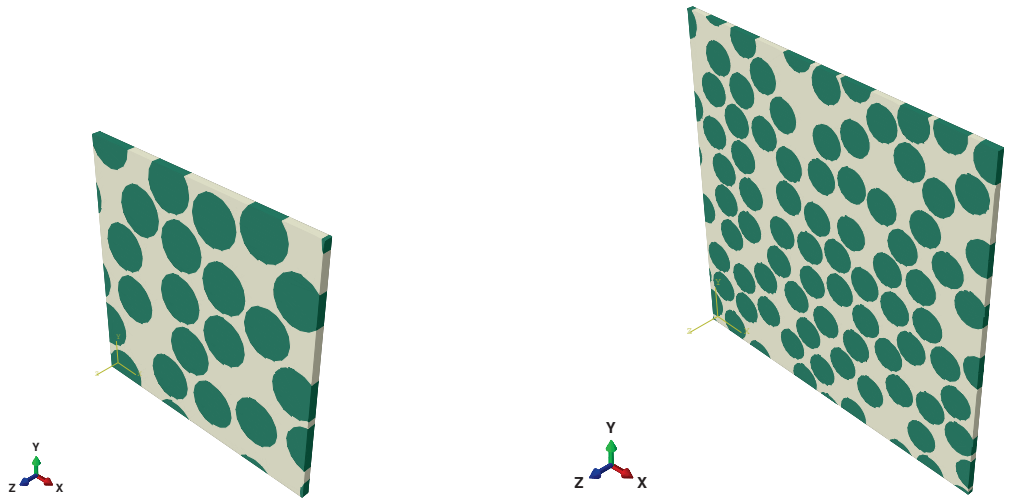

Figure 3.1. Left: RVE-I which is $25\mu m \times 25\mu m$, Right: RVE-II which is $50\mu m \times 50\mu m$. Both RVEs have identical thickness of 0.75 μm.

RVE is also decisive in this matter.

3.2.1. Representative Volume Element (RVE) Generation

Two different prismatic RVEs with constant out-of-plane dimension of 0.75 μm are used in this study. As shown in Figure 3.1, in plane dimensions of the two RVEs are $25\mu m \times 25\mu m$ and $50\mu m \times 50\mu m$, respectively. In both RVEs, fiber volume fraction is almost 60 %. The sizes, fiber volume fraction and fiber distribution of the smaller RVE (RVE-I) is based on Melro's study (Melro et al., 2013b). RVEs consist of randomly distributed (Melro et al., 2008) circular fibers with constant diameter of $5\mu m$ (Canal et al., 2009; Melro et al., 2013b; Totry et al., 2008).

Most of the macroscopic failure criteria designate fiber direction as 1, and transverse directions as 2 and 3 axis (Catalanotti et al., 2013; Puck, 1998), respectively. Thence, throughout the chapter fiber direction (Z axis in Figure 3.1) is also labeled as 1, and in-plane directions (X and Y axis in Figure 3.1) are denoted as 2 and 3 axis, respectively. A closer look at fiber distribution, particularly the ones cut by the edges, reveals that geometric periodicity in both directions are enforced, please see Figure 3.2. In other words, fibers cut by the boundaries of RVE complete each other.

Deformation process at any macroscopic point is driven by the macroscopic strain tensor ε_M. It is to be noted that each RVE is in fact associated with a macroscopic material point. Therefore macroscopic deformation measure ε_M has to be imposed on the underlying micro-level computational domain. Among various alternatives, periodic

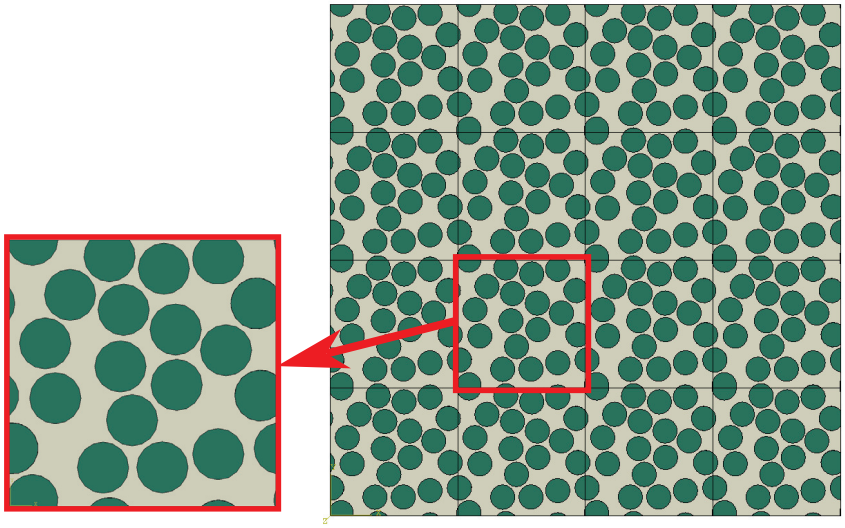

Figure 3.2. Geometric periodicity of Representative Volume Elements

boundary conditions (PBCs) which essentially impose periodicity on the fluctuation field, are used over the RVE. By means of the macroscopic strain tensor, $\boldsymbol{\varepsilon}_{\mathrm{M}}$, the displacements are applied to the nodes of the RVE. For the rest of the discussion, positive X, positive Y and positive Z faces in Figure 3.3 are denoted by l, n and p, respectively. Similarly, negative counterparts are denoted by k, m and q, respectively. Then the displacement relation between nodes only on faces is defined as follows,

$$\mathbf{u}_l = \mathbf{u}_k + \boldsymbol{\varepsilon}_{\mathrm{M}}\,\mathrm{l}_3; \quad \mathbf{u}_p = \mathbf{u}_q + \boldsymbol{\varepsilon}_{\mathrm{M}}\,\mathrm{l}_1; \quad \mathbf{u}_n = \mathbf{u}_m + \boldsymbol{\varepsilon}_{\mathrm{M}}\,\mathrm{l}_2 \tag{3.1}$$

where the vectors $\mathrm{l}_1, \mathrm{l}_2$ and l_3 are defined as,

$$\mathrm{l}_1 = \mathbf{X}_4 - \mathbf{X}_1; \quad \mathrm{l}_2 = \mathbf{X}_2 - \mathbf{X}_1; \quad \mathrm{l}_3 = \mathbf{X}_5 - \mathbf{X}_1 \tag{3.2}$$

In Equation 3.1, matrix-column notation is used and vectors vectors $\mathrm{l}_1, \mathrm{l}_2$ and l_3 are written as columns. To complete the imposition of PBCs, the relation between corner nodes (Black

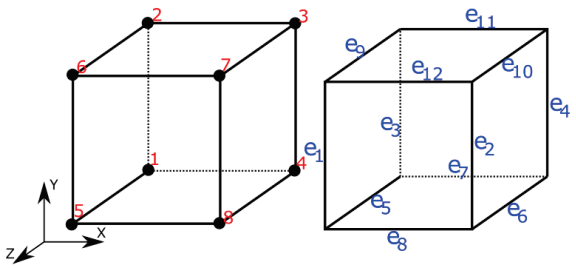

Figure 3.3. Node (left) and edge (right) numbering of RVE model

dots in Figure 3.3) must be defined. Since u_1 is prescribed, the displacement of corner nodes 2, 4 and 5 are defined as follows,

$$\mathbf{u}_2 = \boldsymbol{\varepsilon}_{\mathrm{M}}\, \mathbf{l}_2; \quad \mathbf{u}_4 = \boldsymbol{\varepsilon}_{\mathrm{M}}\, \mathbf{l}_1; \quad \mathbf{u}_5 = \boldsymbol{\varepsilon}_{\mathrm{M}}\, \mathbf{l}_3; \tag{3.3}$$

and the displacement at remaining corner nodes are defined as,

$$\begin{aligned} \mathbf{u}_3 = \mathbf{u}_2 + \mathbf{u}_4; \quad \mathbf{u}_6 = \mathbf{u}_2 + \mathbf{u}_5 \\ \mathbf{u}_7 = \mathbf{u}_8 + \mathbf{u}_2; \quad \mathbf{u}_8 = \mathbf{u}_5 + \mathbf{u}_4 \end{aligned} \tag{3.4}$$

Finally, the displacement relations between edges are written as,

$$\begin{aligned} \mathbf{u}_{e1} = \mathbf{u}_{e3} + \mathbf{u}_5; \quad \mathbf{u}_{e2} = \mathbf{u}_{e3} + \mathbf{u}_4 + \mathbf{u}_5; \quad \mathbf{u}_{e4} = \mathbf{u}_{e3} + \mathbf{u}_4 \\ \mathbf{u}_{e8} = \mathbf{u}_{e7} + \mathbf{u}_5; \quad \mathbf{u}_{e6} = \mathbf{u}_{e5} + \mathbf{u}_4; \quad \mathbf{u}_{e9} = \mathbf{u}_{e5} + \mathbf{u}_2 \\ \mathbf{u}_{e10} = \mathbf{u}_{e5} + \mathbf{u}_4 + \mathbf{u}_2; \quad \mathbf{u}_{e11} = \mathbf{u}_{e7} + \mathbf{u}_2; \quad \mathbf{u}_{e12} = \mathbf{u}_{e7} + \mathbf{u}_4 + \mathbf{u}_5 \end{aligned} \tag{3.5}$$

Constraint equations are used to impose these periodicity conditions, (Yuan and Fish, 2008). To this end, it is ensured that there are matching nodes on the opposite surfaces e.g., left-right, top-bottom and front-back surfaces, of RVE at the matching coordinates. By varying the components of ϵ_M, various in-plane deformation modes are imposed on the RVE. Upon completion of the analysis, macroscopic stress tensor σ is obtained as the volume average of microscopic stress distribution as,

$$\sigma_M = \frac{1}{V} \int_V \sigma_m \, dV \tag{3.6}$$

which holds due to Hill-Mandel condition of homogenization theory, (Nemat-Nasser, 1999).

It is important to note that PBCs put restrictions on the set of probable orientation of microscopic localization band and therefore under PBCs, the orientation of the resulting microscopic localization band might not be representative of the physically observed ones, particularly under multi-axial stress/strain states, (Coenen, Kouznetsova, Bosco, and Geers, 2012; Coenen, Kouznetsova, and Geers, 2012; Hofman et al., 2023). However, until the onset of localization within the RVE, peak load capacity is reached and therefore this information can be conveniently used to construct computationally obtained failure envelope.

3.3. Constitutive Models

In the RVEs, three different constituents, namely, fiber, matrix and fiber-matrix interactions, are considered. Hence, three different material models are used. In the following paragraphs constitutive models for each material is briefly explained.

3.3.1. Fiber Response

Failure of fibers, especially under the influence of longitudinal compressive load, i. e. fiber kinking, is not the central issue in this study. However, it is known that modeling of fiber failure has been a long standing problem and requires special modeling frameworks (Naya et al., 2017; Poulios and Niordson, 2016; Romanowicz, 2014).

If the loading is dominated by in-plane deformations, damage and final failure spread over matrix and matrix-fiber interactions. Thence, for loading scenarios where longitudinal (parallel to fiber) directions component is weak, it is convenient to assume that fibers stay within elastic limits. Therefore, linear elasticity at small strains is used for fibers. Consequently, the stress tensor, $\boldsymbol{\sigma}$, is defined as,

$$\boldsymbol{\sigma} = \mathbb{C}_f : \boldsymbol{\varepsilon}_f \tag{3.7}$$

where, $\mathbb{C}_f$ is fourth order elasticity tensor and " : " denote double contraction. To construct $\mathbb{C}_f$ two elasticity constant, Young's Modulus (E_f) and Poisson's ratio (ν_f), are used where subscript f refers to fiber phase. The values of E_f and ν_f are 74 GPa and 0.20, respectively. Those values are extracted from World Wide Failure Exercise's input data (Kaddour and Hinton, 2013).

3.3.2. Matrix Response

Damage-plasticity mode presented in Chapter 2 is used for the matrix along with the parameters identified in Section 2.5.2. For the sake of completeness, calibrated material properties for the matrix phase are presented in Table 3.1.

Table 3.1. Material properties

E (MPa)	ν	ν_p	β^+	β^-	$\eta^{+,-}$	R	κ_i^+	κ_i^-	l_c
3760	0.33	0.39	5	7	1	0.005	0.025	0.15	0.001

3.3.3. Matrix-Fiber Interaction

The matrix-fiber interaction is modeled using cohesive contact. For this purpose a surface-to-surface contact between matrix and fibers are defined. The response of the cohesive contact is controlled by bi-linear traction-separation law upon the initiation of damage. The traction vector, $\boldsymbol{t}$, consists of two shear components t_s, t_t, and normal component t_n, respectively. Similarly, the separation (opening) vector, $\boldsymbol{\delta}$, also consists of two shear δ_s, δ_t and a normal δ_n component. In this work, the coupling between shear and normal separation is dropped, (Melro et al., 2013b; Wan et al., 2020). Furthermore, same values are assigned to stiffness values in two shear directions, K_{ss} and K_{nn}. There is a wide range for K_{nn} values in literature. Thence, following (J. F. Chen et al., 2014), for K_{nn} is set to 10^6 MPa. Therefore the elastic behavior of cohesive contact is defined as,

$$\begin{bmatrix} t_n \\ t_s \\ t_t \end{bmatrix} = \begin{bmatrix} K_{nn} & 0 & 0 \\ 0 & K_{ss} & 0 \\ 0 & 0 & K_{tt} \end{bmatrix} \begin{bmatrix} \delta_n \\ \delta_s \\ \delta_t \end{bmatrix} \tag{3.8}$$

The initiation of damage is based on the following quadratic stress criteria,

$$\left(\frac{<t_n>}{t_n^0}\right)^2 + \left(\frac{t_s}{t_s^0}\right)^2 + \left(\frac{t_t}{t_t^0}\right)^2 = 1 \tag{3.9}$$

where $<>$ is Macaulay brackets, which returns the value in brackets if it is positive, and returns zero otherwise. Furthermore, t_n^0, t_s^0, t_t^0 represent the peak stress values of normal stress when separation is purely normal to the interface, and purely in the first and second shear directions, respectively. As an outcome of the Macaulay brackets only tensile traction initiates damage. After the initiation of damage the initial traction stress, t^0, is reduced by means of the damage parameter. The damage variable monotonically increases from 0 (in the absence of any damage) to 1.0 (at the final failure) and the traction drops linearly upon damage initiation as shown in Figure 3.4. An effective separation defined in terms of separation components as $\delta_{eff} = \sqrt{\delta_n^2 + \delta_s^2 + \delta_t^2}$ is used to describe damage evolution. Representing the effective separation at damage initiation by δ_{eff}^0 and

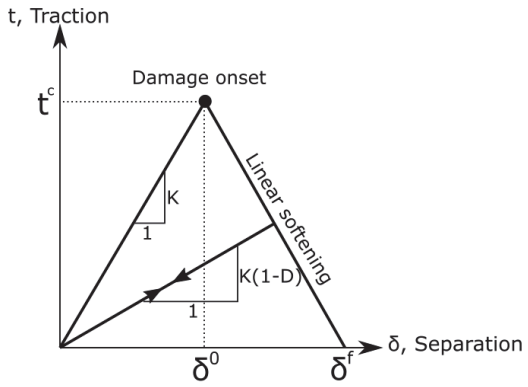

Figure 3.4. Traction separation law for contact

the maximum effective separation reached δ_{eff}^{max}, the following linear damage evolution law,

$$D = \frac{\delta_{eff}\,(\delta_{eff}^{max} - \delta_{eff}^{0})}{\delta_{eff}^{max}\,(\delta_{eff}^{f} - \delta_{eff}^{0})} \tag{3.10}$$

is used in this work. The effective separation at complete failure is defined in terms of critical mixed-mode fracture energy G_C and effective traction at damage initiation t_{eff}^{f} as $\delta_{eff} = \frac{2\,G_C}{T_{eff}^{f}}$. Critical mixed-mode energy G_C is based on the work of Benzeggagh and Kenane (Benzeggagh and Kenane, 1996) and is given as,

$$G_C = G_n^C + (G_s^C - G_n^C)\left(\frac{G_S}{G_T}\right)^{\eta_f} \tag{3.11}$$

where $G_S = G_s^c + G_n^c$ and $G_T = G_n^C + G_s^C$. Mode-mixity is controlled by the model parameter η_f and critical fracture energy in normal mode and orthogonal shear modes are designated by G_n^C, G_s^C and G_t^C, respectively. The parameters for the cohesive contact used in RVE analysis is summarized in Table 3.2.

3.4. Abaqus Implementation & Work Flow

RVE models consist of matrix, fiber, and matrix-fiber interactions. Python scripts are generated to create each geometric part and assign contact between fiber and matrix. Furthermore, with this script, as long as locations of fibers are prescribed, the whole model is generated, and geometric periodicity is provided. Once the model is generated using the first Python script, periodic boundary conditions are imposed by means of constraint equations tying periodic surface pairs. Since the total number of constraint equations is

Table 3.2. Interaction properties

Property	Value
K_{nn}	10^6 MPa
K_{ss}	10^6 MPa
K_{tt}	10^6 MPa
t_n^0	50 MPa
t_s^0	70 MPa
t_t^0	70 MPa
G_n^c	$2 \times 10^{-3} J/mm^2$
G_s^c	$6 \times 10^{-3} J/mm^2$
G_t^c	$6 \times 10^{-3} J/mm^2$

quite large, another Python script is developed to apply PBC. To construct discrete failure loci large number of RVE analysis have to be conducted. Thence, a third Python script is defined to impose different in-plane loading states by varying the macroscopic strain tensor. With these three scripts, the model is generated in Abaqus CAE. For the next phase of model generation, the Abaqus input file is modified. Thence, a fourth Python script is used to add user elements in the model. Finally, upon completion of RVE analysis, homogenized stress tensor is computed through the volume integral given by Equation (3.6). Thence, the last Python script simply computes the homogenized stress through a numerical integration over user elements and the stress components extracted from each integration point.

3.5. RVE Response under Basic Deformation Modes

As mentioned in Section 3.2.1, by varying the macroscopic strain tensor, $\boldsymbol{\varepsilon_M}$, different load combinations can be applied to RVE model and different stress states can be realized. To investigate the performance of RVE model under the influence of basic deformation modes, three different macroscopic loading mode are realized by tuning the components of $\boldsymbol{\varepsilon_M}$. These basic modes correspond to macroscopic uni-axial tension, macroscopic in-plane shear and an almost macroscopic uni-axial compression stress states, respectively. Since the ratio of shear to compression ratio in the third model is $\frac{1}{10}$, that model is denoted as almost uni-axial compression load. Element size of the RVE model is sufficiently small, $(0.0005$ mm$)$, and based on a mesh convergence study. Furthermore, to increase stability of the computation, viscosity parameter of 2×10^{-5} is used which is

still much smaller than the default value, i.e., one tenth of Abaqus' suggested value.

In Figure 3.5, the distribution of matrix damage at the end of the analysis for basic macroscopic deformation modes are presented. It must be mentioned that, to prevent numerical instabilities the maximum value for damage is limited to 0.99. Failure of cohesive surfaces are clearly visible for uni-axial tension and in-plane shear models. For the in-plane shear load and uni-axial compression the maximum damage value is observed in small volumes. On the contrary to that, for the case of uni-axial tension load the maximum damage is distributed over a band.

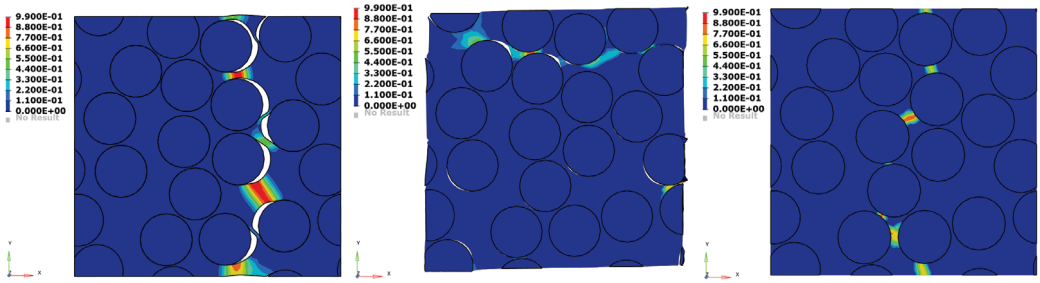

Figure 3.5. Left: Bulk tensile damage distribution under macroscopic uni-axial tension in X-direction, Middle: Bulk tensile damage distribution under macroscopic in-plane shear, Right: Bulk compressive damage distribution under almost uni-axial macroscopic compression in Y-direction.

Macroscopic strain-macroscopic stress components of RVE model can be obtained through Equation (3.6). Such components for uni-axial tension and bi-axial tension (in a macroscopic sense) are presented in Figure 3.6. Peak stress values in those macroscopic strain and macroscopic stress diagrams are key ingredients to construct discrete failure envelopes. It must also be mentioned that due to heterogeneous nature of RVE models, both uni-axial and bi-axial macroscopic strain states result in shear stress response as well (Figure 3.6).

3.6. Effect of Boundary Conditions on Non-local Quantities

There are two different boundary condition options for non-local equivalent plastic strain fields. In the first option natural boundary conditions, i. e. $\nabla \bar{\varepsilon}_{eq}^{p,(+,-)} \cdot \boldsymbol{n} = 0$ is imposed on the boundaries of the RVE model (Melro et al., 2013b; Sarkar et al., 2019). However, in the second option, similar to the periodicity of the displacement field, periodicity of non-local equivalent plastic strain fields (left-to-right, top-to-bottom

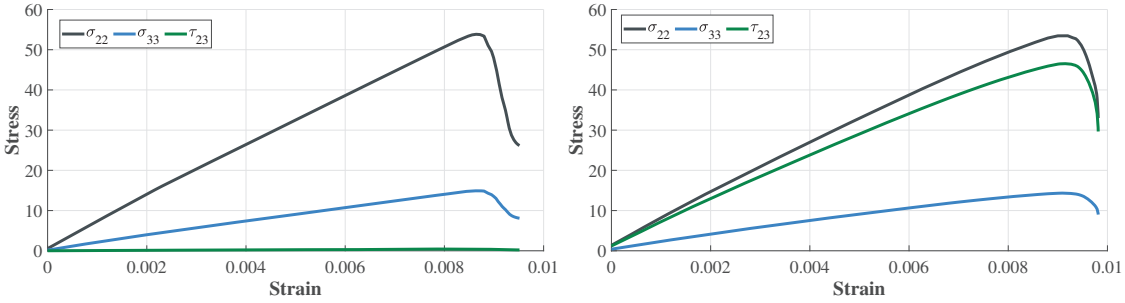

Figure 3.6. Left: Macroscopic strain (uni-axial tension) versus macroscopic stress components, Right: Macroscopic strain (bi-axial tension) versus macroscopic stress components

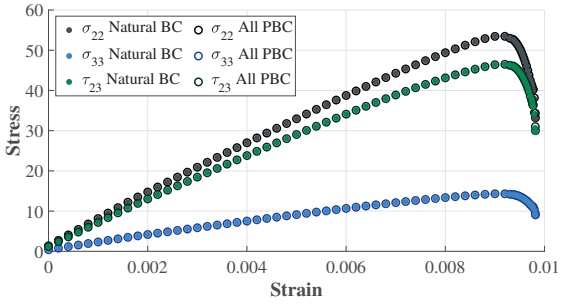

Figure 3.7. Comparison of the boundary conditions on non-local equivalent plastic strain fields.

and front-to-back faces of RVE model) are enforced by using constraint equations. The resulting macroscopic strain - macroscopic stress diagrams for both options are presented in Figure 3.7. As seen from the graphs, there is a slight different between curves after peak stress values. Since, only peak stress values are used for the construction of discrete failure loci, the first option, i.e. natural boundary conditions, are chosen in this study. Furthermore, with the choice of natural boundary conditions the number of constraint equations in model is reduced significantly. As mentioned in Section 3.4, for RVE generation, discretization, imposition of periodic boundary conditions and evaluation of macroscopic stress tensor, a set of Python scripts are generated and all the work-flow is automatized.

3.7. Influence of Fiber Distribution and RVE size

Macroscopic stress curves obtained through homogenization are key ingredient for constructing discrete failure locus. Peak stress value for specific macroscopic stress curve is considered to be the onset of failure. Furthermore, by marking peak stress values on relevant plane of stress space discrete failure locus can be constructed. In other words,

by marking peak stress values of sufficient number of RVE analysis on relevant plane of stress space discrete failure locus can be constructed. Such discrete failure locus is considered to be a reliable way to evaluate the predictive capabilities of phenomenological failure criteria. Furthermore, by imposing some level of uncertainty into RVE model and constructing failure locus statistical analysis of RVE may be carried out (Wongsto and Li, 2005; Yu et al., 2015).

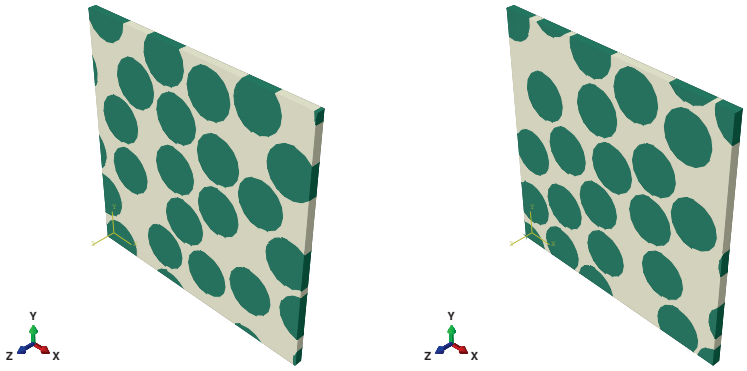

Figure 3.8. RVE-I with two different fiber distributions (designated as RVE-I-D-A and RVE-I-D-B; fiber volume fractions are identical) (Melro et al., 2013b)

As far as properties associated with RVE geometry are concerned, the size of RVE, fiber volume fraction and the distribution of fibers are very important. Furthermore, those parameters may influence the resulting RVE response significantly. In this thesis, fiber volume fraction of approximately 60% is used since this fiber volume fraction is widely used in literature (Canal et al., 2009; Melro et al., 2013b; Totry et al., 2008). To address the effects of fiber distribution, two different fiber distributions with RVE-I (Figure 3.1) are generated. Distributions are designated as RVE-I-D-A and RVE-I-D-B (Figure 3.8). To construct failure loci for each RVE model, various load combinations are applied and peak stress values are obtained through an automated work-flow. These peak stress values are marked in $\sigma_2 - \tau_{23}$ stress space. Consequently, discrete failure loci for each fiber distribution is constructed. Discrete failure loci for each distribution is compared in Figure 3.9. As seen from the figure, both RVE models yield very close results for tensile σ_2 half of the stress plane. However, for negative half of σ_2 stress plane, a few analysis results drift from main trend. The reason of such drift may be the slightly premature failure of matrix due to localization of deformation within narrow bands between fibers, under the influence of large compressive and axial stress states.

To investigate the effects of RVE dimensions, RVE-II model is used (Figure 3.10).

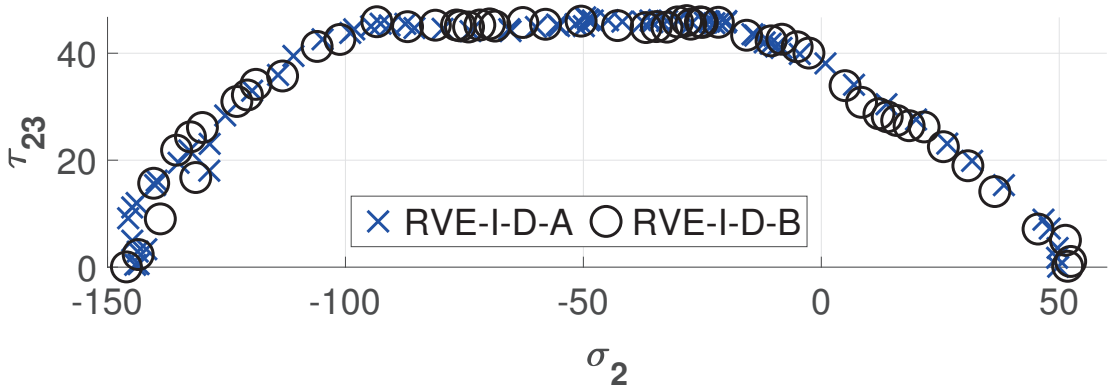

Figure 3.9. Comparison of the failure loci from RVE analysis for different fiber distributions

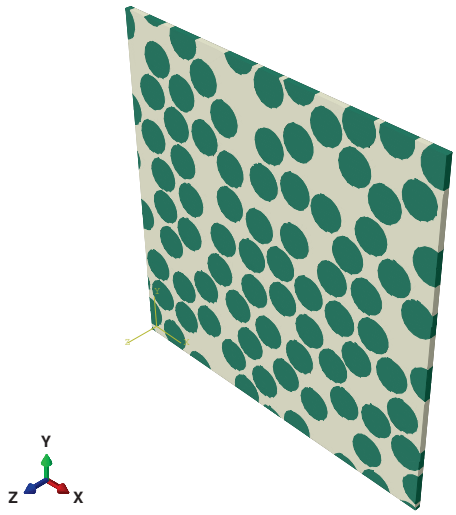

Figure 3.10. RVE-II (Melro et al., 2013b)

RVE-II model is analyzed under the influence of various in-plane loads similar to RVE-I model. In Figure 3.11 failure envelopes obtained from RVE-I and RVE-II are compared which supports that RVE-I and RVE-II results are quite close. Furthermore, in Figure 3.12 curves are fitted to RVE-I-D-A, RVE-I-D-B and RVE-II results. As seen from the fitted curves, the results are indeed very close. From Figure 3.11 and Figure 3.12 it is understood that both the dimensions of RVE-I-D-A and the corresponding fiber distribution are adequate to represent the response of RVE. Therefore, for the rest of the study RVE-I-D-A is used. Furthermore, for the sake of simplicity RVE-I-D-A model is denoted as RVE-I in the rest of this chapter.

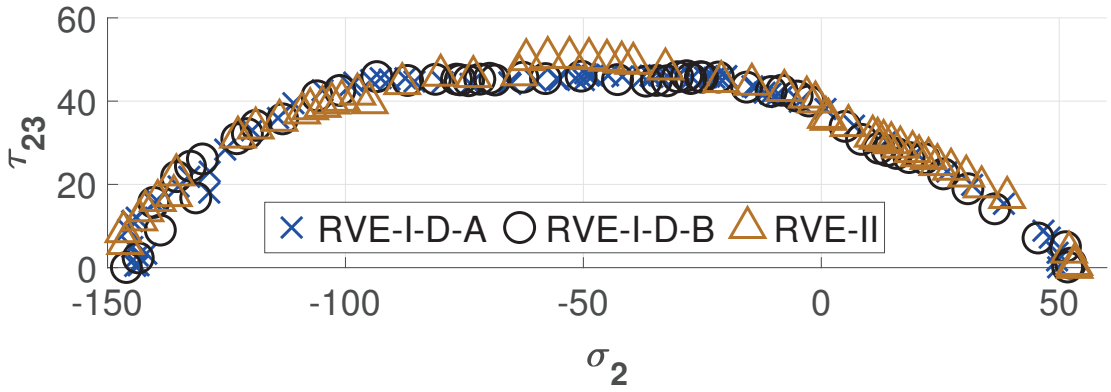

Figure 3.11. Failure loci from RVE analysis with various distributions and sizes.

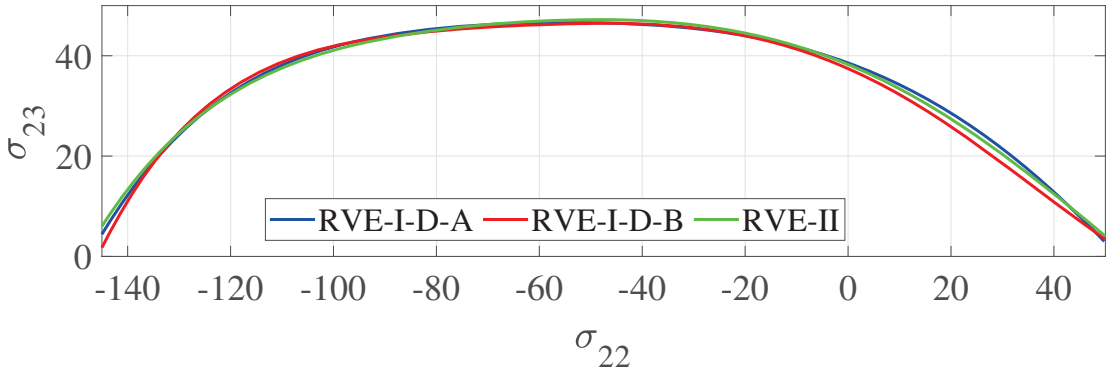

Figure 3.12. Failure loci from RVE analysis with various distributions and sizes.

3.8. Comparison with Macroscopic Failure Criteria

As mentioned in the introduction of this Chapter, statistically representative computational micro-mechanical models with calibrated constitutive models can be used to assess the capacities of macroscopic (or phenomenological) failure criterion. Since Puck's Failure Criteria outperforms many of the phenomenological models in both world wide failure exercise I and II (Kaddour and Hinton, 2012; Soden et al., 2004), particular attention is paid to Puck's Failure Criteria. Furthermore, Puck's Failure Criteria provides not only a quantitative prediction of the failure stress but also the mode of failure (Deuschle and Puck, 2013). Such feature is missing in many of the commonly used failure criteria, (Azzi and Tsai, 1965; Tsai and Wu, 1971). Puck's failure criteria is going to be discussed in more detail in the next Chapter. To construct failure envelope of Puck's criteria, strengths and inclination parameters are required. Strength values are taken from WWFE input parameters (Kaddour and Hinton, 2012) and inclination parameters are taken from Deuschle and Puck, 2013, respectively. These values are summarized in Table 3.3. In table 3.3, Y^t, Y^c and S_{23} denote transverse tension, transverse compression and through-thickness

shear strengths, respectively. A sufficiently large number of RVE analysis are conducted on RVE-I by varying the components of macroscopic strain tensor ε_M. Resulting failure macroscopic (homogenized) stress components are used to construct the discrete failure loci.

Table 3.3. Material properties

$p^t_{\perp\perp}$	$p^c_{\perp\perp}$	$p^t_{\perp\parallel}$	$p^c_{\perp\parallel}$	Y^t (MPa)	Y^c (MPa)	S_{23} (MPa)
0.35	0.30	0.25	0.30	45	145	40

Discrete failure loci from RVE analysis and continuous failure loci obtained from Puck's Failure Criteria for stress planes of $\sigma_2\tau_{23}$, $\sigma_2\sigma_3$ and $\sigma_2\tau_{12}$ are compared in Figure 3.13, Figure 3.14 and Figure 3.15, respectively. As seen from these figures, RVE results and Puck's Failure Criteria results are generally in good agreement. However, for the predictions for $\sigma_2\tau_{23}$ stress plane (Figure 3.13), there is discrepancy between results, particularly for tensile σ_2 dominated region. From RVE analysis, particularly for tensile stress dominated points, it is observed that the stiffness value of contact surfaces have a great influence on the resulting failure initiation. As mentioned previously material properties are calibrated through the experimental study of Fiedler (Fiedler et al., 2001). However, stiffness values for contact surfaces are taken from (J. F. Chen et al., 2014). Generally, the stiffness values for contact surfaces could not measured directly and typically use of sufficiently large value, which provides load redistribution, is recommended. Furthermore, there is a large range of stiffness values ranging in between 10^6 Mpa to 10^8 Mpa in literature (J. F. Chen et al., 2014; Melro et al., 2013b; Palizvan et al., 2020; Sun et al., 2019). In the context of this study, stiffness values for contact surfaces seem to be 'fitting parameters'. Furthermore, since the characterization of interfaces including stiffness values is quite complex task, prediction of contact stiffness values does not have a simple or practical solution. Inconsistencies regarding the stiffness values for contact surfaces may be solved by explicit modeling the interphase regions around fibers (Sun, Guo, et al., 2018; Sun, Meng, et al., 2018; Sun et al., 2019; Zhang et al., 2018). If the interphase region around fibers has different properties from matrix then the influence of contact stiffness over results may cease. However, since the element size for such interphase regions are very small, the computational costs of RVE analysis may increase drastically with the addition of interface regions. Unfortunately, due to limited computational power, in this study interface regions are not introduced around the fibers.

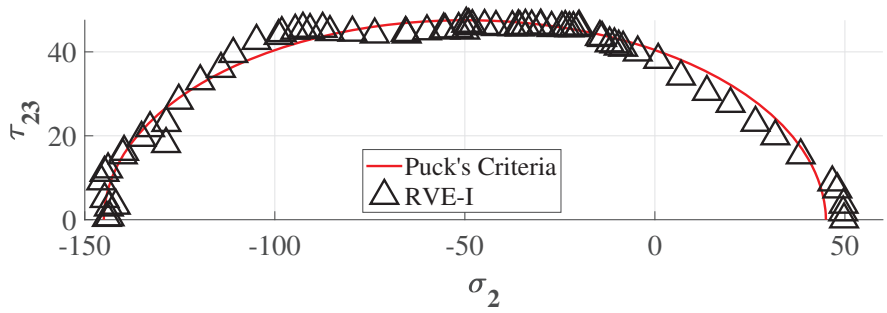

Figure 3.13. Discrete failure points and Puck's envelope within $\sigma_2 - \tau_{23}$ plane

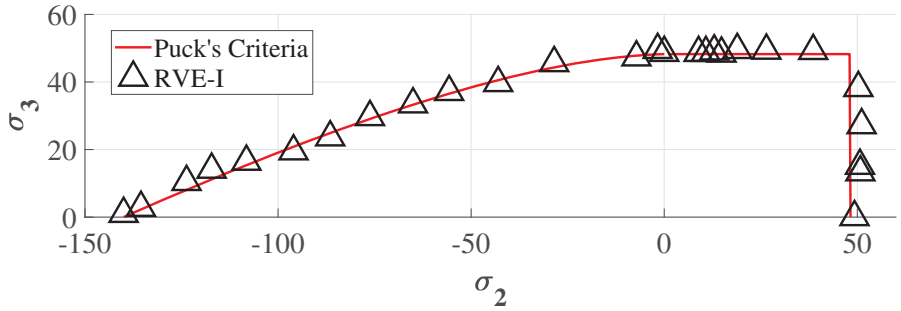

Figure 3.14. Discrete failure points and Puck's envelope within $\sigma_2 - \sigma_3$ plane

3.9. Influence of Microscopic Imperfections

Computational micro-mechanics model can be effectively used to investigate the effects of micro-structural imperfections (Ashouri Vajari et al., 2014; Palizvan et al., 2020; Skovsgaard and Jensen, 2018; Zhang et al., 2018). In this study, the effects of interface imperfections at matrix fiber interactions are considered. Such imperfections may result from air pockets entrapped at matrix fiber interfaces. By halving the initial strength values of cohesive surfaces, i.e. t_n^0, t_s^0, t_t^0, such imperfections are introduced. To investigate the effects of the fraction of imperfect interfaces, various fractions of imperfect interfaces are used. The percentage of imperfect interface starts from 10% and increased up to 100%. For all fractions, imperfect interfaces are chosen randomly and to investigate the effects of the distribution of imperfect interfaces two different distributions are generated. It must be mentioned that percentages reflect the fraction of imperfect interfaces not the degree of imperfection. In Figure 3.16 distribution of imperfect interfaces for fractions of $10, 20$ and 40% are presented. Using the RVE models in Figure 3.16 the effects of the distribution of imperfect interfaces are investigated. In Figure 3.17, comparison of intact model, imperfect interface model and continuous failure locus for Puck's Failure Criteria for imperfect interface fractions of $10, 20$ and 40% are compared. As seen from figure, as long as the same fraction of imperfect interfaces are introduced, RVE models yield

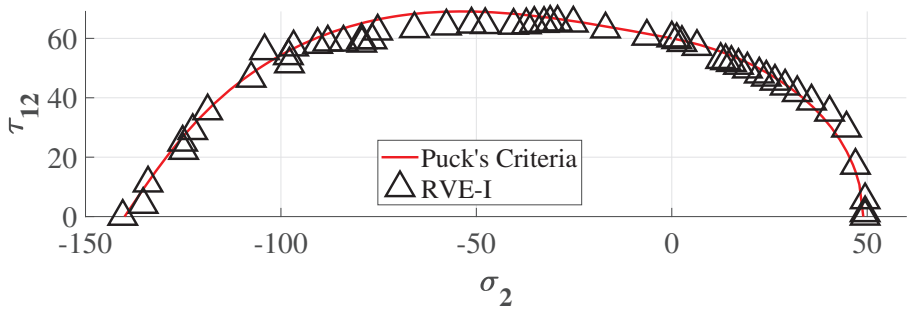

Figure 3.15. Discrete failure points and Puck's envelope within $\sigma_2 - \tau_{12}$ plane

very close results. Thence, it is understood that the reduction in discrete failure locus for imperfect interface models is a function of the fraction of imperfect interface, not the location of imperfect interface.

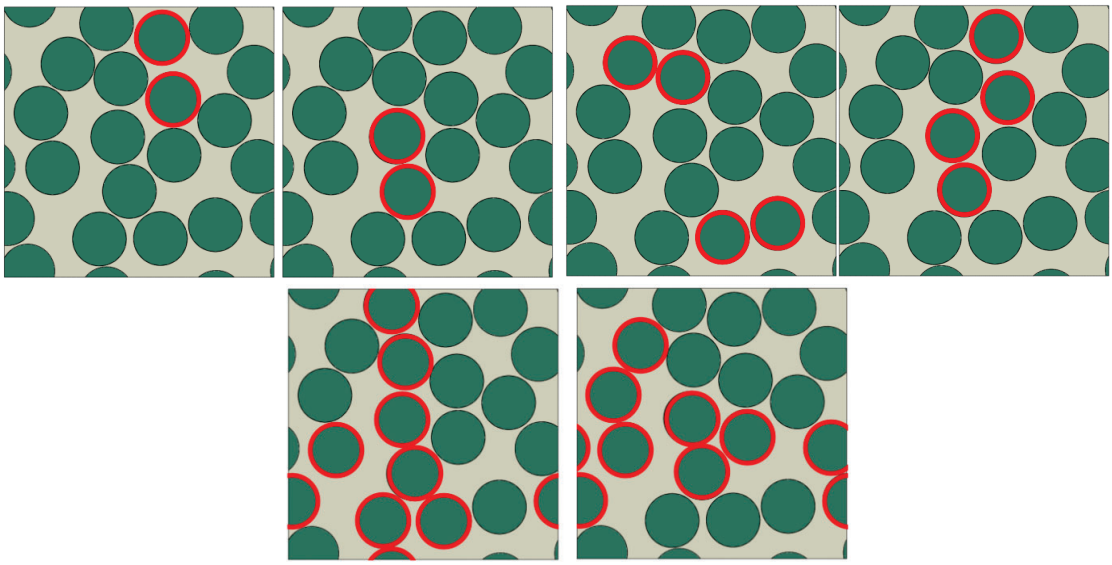

Figure 3.16. Distribution of imperfect interfaces (I. I.)

In Figure 3.18 discrete failure loci from intact RVE, RVEs with imperfect interface fractions of 10%, 20% and 40% and continuous failure locus from Puck's Failure Criteria are compared. As seen from figure, for 10% and 20% imperfect interface fractions similar drops are obtained. However, for the case of 40% imperfect interface fraction there is a significant drop in peak stress values, i.e. discrete failure locus shrinks significantly. Similarly in Figure 3.19, discrete failure loci from intact RVE, RVEs with imperfect interface fractions of 50%, 60% and 100% and continuous failure locus from Puck's Failure Criteria are compared. As seen from Figure 3.19, models with imperfect interface fraction larger than 40% yield very close results. In Figure 3.20 fitted curves to discrete failure

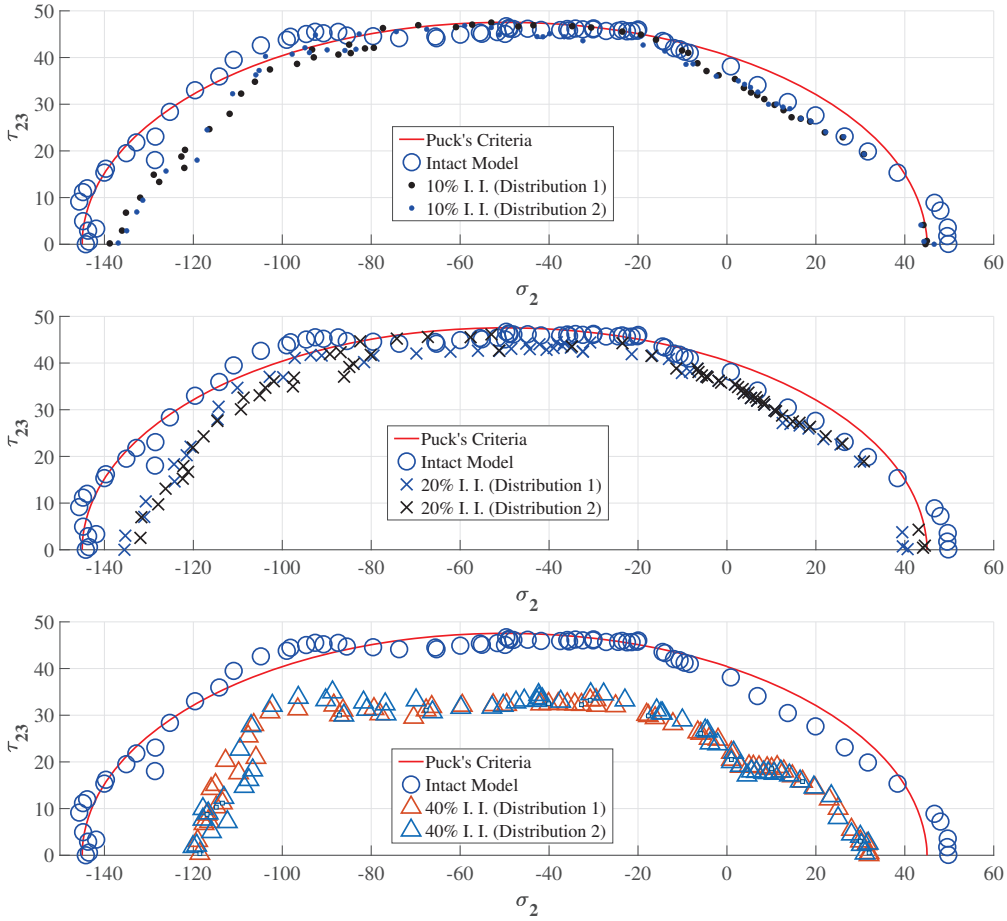

Figure 3.17. 0%, 10%, 20% and 40% imperfect interface failure loci are compared

loci for intact RVE model and RVE models with various imperfect interface fractions are presented. From the figure it is observed that on the tension dominated part, ($+\sigma_2$ half), above 40% of imperfect interfaces fraction, discrete failure loci become insensitive to any increment in imperfect interface fraction. On the compression dominated part, ($-\sigma_2$ half), insensitivity to the fraction of imperfect interface starts between fraction values of 40% and 50%. The reason of insensitivity to imperfect interface may be explained by the existence of imperfect interface chains from one side to opposite side of RVE, please see Figure 3.16. Due to imperfect interface chains, stress is distributed within the matrix material. Consequently, the response of RVE after 40% of imperfect interface is dominated by matrix material. Therefore, the effect of imperfect interfaces after 40% become insignificant. It has to be noted that drops in uni-axial compression, in-plane shear and uni-axial tension strength values for 40% of imperfect interface are 17%, 35% and 46%, respectively.

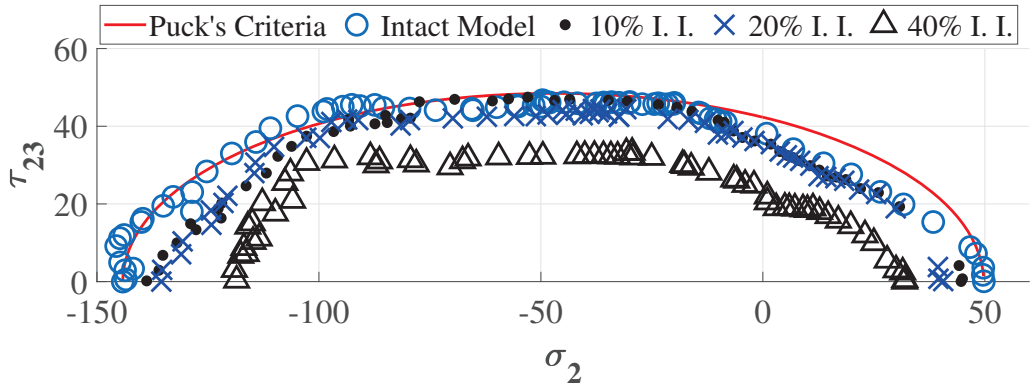

Figure 3.18. 0%, 10%, 20% and 40% imperfect interface failure loci are compared.

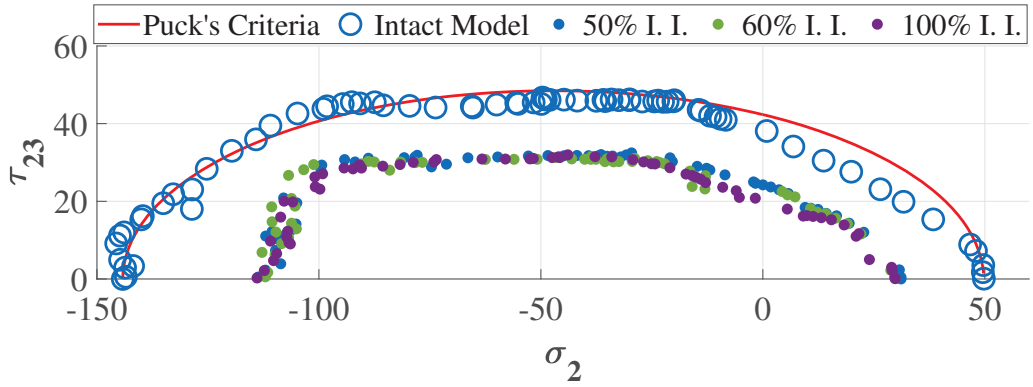

Figure 3.19. 50%, 60% and 100% imperfect interface failure loci are compared.

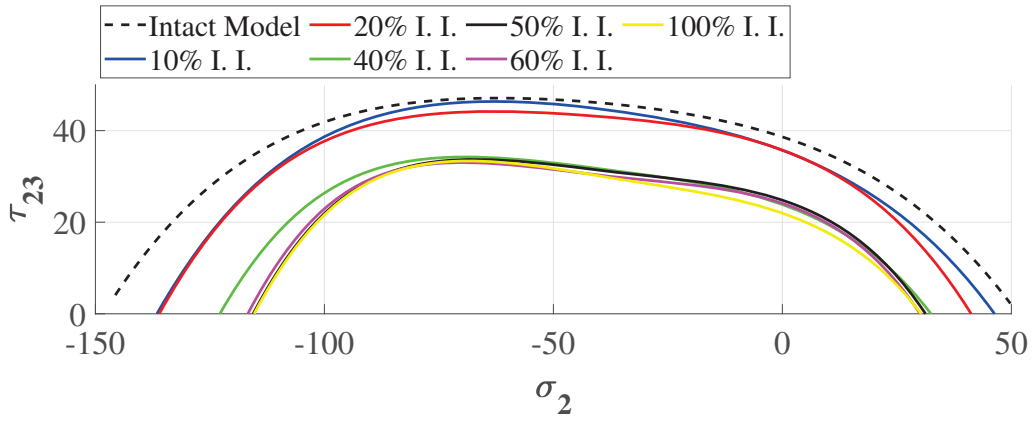

Figure 3.20. Curves fitted to increasing imperfect interface failure points compared.

3.10. Effect of Longitudinal Normal Stress

In original version of Puck's Failure Criteria (Puck, 1998) the effects of normal stresses parallel to fiber direction, σ_1, over Inter Fiber Failure are neglected. However, under the influence of normal stresses parallel to fiber direction, due to local imperfections or statistical nature of fiber strengths (Yu et al., 2015), premature failure of fibers may be observed. Such failures may cause local damage in lamina. Hence, separation of matrix-fiber interfaces or initiation of matrix damage may be formed (Knops, 2008). These mechanisms are introduced in Puck's Failure Criteria utilizing weakening factor, η_{w1} (Knops, 2008; Puck et al., 2002). Weakening factor is used to modify exposure factor associated with Inter Fiber Failure as follows,

$$f_{E,IFF}^{+,-} = \frac{f_{E,IFF}^{+,-}}{\eta_{w1}} \tag{3.12}$$

where, fiber exposure factor, i.e. σ_1, based computation of η_{w1} is presented in Knops, 2008. To investigate the effects of σ_1 various RVE models under the influence of out-of-plane loads are constructed. By setting the corresponding components in $\boldsymbol{\varepsilon}^M$ stress state with out-of-plane tension load is constructed. This process is repeated for various normal tension loads. Consequently, upon homogenization discrete failure locus for each load combination is generated. In Figure 3.21, discrete failure loci for each normal stress state is compared with modified Puck's Failure criteria for various η_{w1} values. From Figure 3.21 it is observed that for the tension side of failure loci, failure points are almost insensitive to out-of-plane tension loads. However, for compression side there is a significant reduction in failure stress values. Although extended version of Puck's criteria allows for different weakening factors for tension and compression sides, it is worthy to note that on the tension side a weakening factor doesn't seem to be necessary. The reduction in the capacity for compression side may be explained with the contractile strains, which are formed due to out-of-plane load, in matrix. When, contractile strains are combined with in-plane compression stress matrix damage may initiate early. Hence, the stress capacity of RVE model may reduce for compression side of failure locus. On the tensile side, an opposite effect may be expected. However, due to limited tensile strain capacity of matrix material, this effect is not observed.

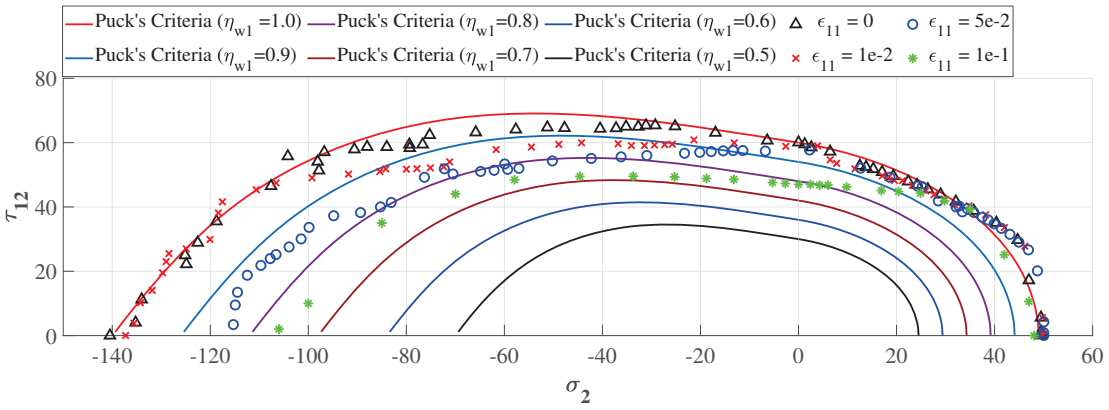

Figure 3.21. Discrete failure points with increasing out-of-plane tensile loading.

3.11. Results and Discussion

In this chapter computational micro-mechanics is used to evaluate the predictive capabilities of Puck's Failure Criteria for long fiber reinforced polymers. Main findings of this chapter can be summarized as follows,

- Even though at some points there exists deviation between RVE results and Puck's Failure Criteria, discrete failure loci and failure loci regarding Puck's Failure Criteria are generally in good agreement. Since, there is not any universally accepted difference margin, it is hard to asses quantitative agreement between Puck's and RVE's results. Deviations for uni-axial compressive load dominated regions may be related to pre-mature failure of thin volume of matrix material which is between fibers within RVE. Furthermore, deviation for tension dominated regions, stiffness of cohesive surfaces have great influence. By introducing interphase regions at matrix-fiber interfaces the effects of stiffness of cohesive surfaces may reduce. However, such modeling strategy may increase computational costs drastically.

- As expected matrix-fiber imperfections cause shrinkage in discrete failure loci. For this RVE modeling, it is observed that the shrinkage is function of the fraction of imperfect interfaces, not the distribution of imperfect interfaces. However, after some fraction of imperfect interfaces discrete failure loci become insensitive to any increment in the fraction of imperfect interfaces. For tension and compression dominated stress planes those threshold imperfect interfaces fractions are 40% and 60%, respectively.

- The effects of out-of-plane loading is investigated to a limited extend. By varying tensile out-of-plane loading, series of RVE analysis are conducted. RVE analysis results are

compared with failure loci of modified Puck's Failure Criteria for various η_{w1} values. From those analysis it is observed that, out-of-plane tensile loads cause reduction in compressive (in-plane) capacity, and do not influence failure initiation loads for tensile (in-plane) capacity. To the best of the author's knowledge this has not reported elsewhere and has not investigated from a micro-mechanical perspective.

CHAPTER 4

MACROSCOPIC MODELING OF FAILURE IN UNI-DIRECTIONAL COMPOSITES

4.1. Introduction

Fiber reinforced composites (FRC) have started to replace conventional (engineering) materials in many engineering fields. These advances are made possible by the progress in manufacturing techniques and reliable predictive failure models.

Among various choices, as proved by World Wide Failure Exercise (WWFE) I and II, Puck's criteria predicts the failure of uni-directional composites both under 2D and 3D stress states, (Kaddour and Hinton, 2013; Soden et al., 2004). Furthermore, the agreement between Puck's criteria and micromechanically constructed failure envelopes presented in the previous chapter is noteworthy. As far as failure analysis is concerned, typically failure initiation within a ply is considered as the complete failure of the component which ignores the remaining capacity which may reach to non-negligible levels in case of multi-ply components. Therefore progressive failure analysis might be necessary to assess the post-peak response of composites. In fact, in this chapter, for the purpose of developing a tool suitable for progressive failure analysis, Puck's failure criteria is combined with a continuum damage mechanics. More precisely, Puck's criteria and localizing implicit gradient damage model is fused so that complete stress-strain can be predicted. In addition to that, an important challenge that has to be overcome is to achieve consistency between the failure angle predicted at material point and the orientation of the emerging macroscopic damage band. This chapter first focuses on Puck's failure criteria in detail. Afterwards, integration of Puck's criteria both in a local damage formulation and gradient based treatment are discussed. Computational implementation is briefly summarized and the model is assessed by means two different problems from the literature.

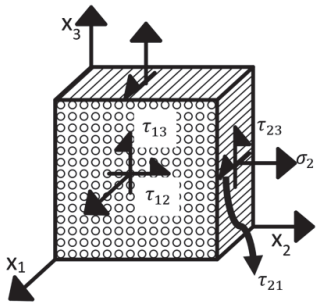

Figure 4.1. Micro-structure of uni-directional conposite

4.2. Puck's Failure Criteria

One of the major features of Puck's failure criteria is the fact that failure of fibers and matrix are treated separately by means of so called Fiber Failure (FF) and Inter Fiber Failure (IFF) criterion. Furthermore for both phases, tension and compression stress states are treated separately as well. IFF takes places on a special plane which is denoted as the action plane. Since all of the stresses contributing to IFF and strength terms related to IFF are computed on this plane, identification of the action place has great importance. In what follows, firstly the stress and strength terms used in Puck's Failure Criteria are briefly discussed. Afterwards, the concept of action plane is explained followed by details of the treatment of Inter Fiber Failure and Fiber Failure, respectively.

In Figure 4.1, typical micro-structure of uni-directional composite is shown where axis x_1 denotes to fiber direction and directions which are transverse to fiber direction are denoted as axis x_2 and x_3, respectively. In the sequel, two shear stress components ($\tau_{\perp\perp}$ and $\tau_{\perp\parallel}$) and one normal stress $\sigma_\perp$ are going to be used frequently. Here $\tau_{\perp\perp}$ and $\tau_{\perp\parallel}$ denote through thickness shear stress (i.e. out-of-plane shear stress) and in-plane shear stress, respectively. As a result of transverse isotropy, the resultant of the normal stresses transverse to fiber direction (σ_2 and σ_3) are equal. In Puck's criteria, the term 'stressing' is introduced to reflect the effect of stresses ($\sigma_1, \sigma_2, \sigma_3, \tau_{12}, \tau_{13}, \tau_{23}$) through $\sigma_\perp$-stressing, $\tau_{\perp\perp}$-stressing and, $\tau_{\perp\parallel}$-stressing. Stresses and different stressing states are presented in Figure 4.2.

In any failure criteria, strength terms are essential to assess the state at any material point. For example, Tsai-Hill (Azzi and Tsai, 1965) and Tsai-Wu (Tsai and Wu, 1971) criterion use strength terms $R_\perp$, $R_{\perp\parallel}$ and $R_{\perp\perp}$ which correspond to strengths obtained under the corresponding stressing state. Hence, these values are the maximum limits which, the material point can resist and; they do not indicate the type of failure, e.g. inter

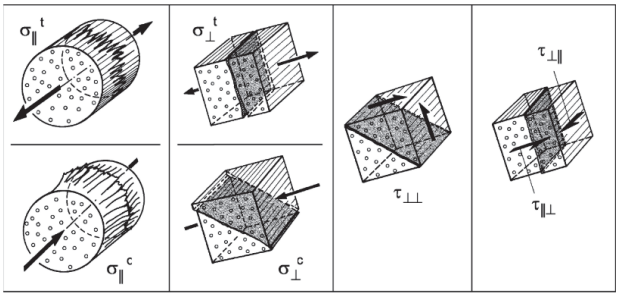

Figure 4.2. Designation of stressing (Knops, 2008)

fiber or fiber, shear failure or tensile failure. Measured strength values act as anchor point in analytic curves, in other words they have no physical meaning. On the contrary, Puck's Failure Criteria gives information about the type and location of failure explicitly.

Following Mohr's hypothesis, Puck claims that failure occurs on the specific plane for which he introduces and uses the action plane concept, (Puck, 1998). Any plane on which the resultant of stresses cause stressing is called as an action plane, see Figure 4.3. In principle there are infinitely many action planes and to define a specific one, axis triad X_1, X_2 and X_3 is rotated about X_1 axis by an angle θ, which results in the new coordinate system and the associated action plane, see Figure 4.3.

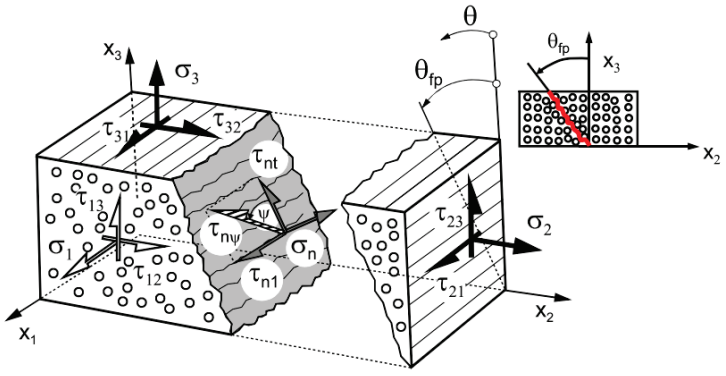

Figure 4.3. Action Plane (Deuschle and Puck, 2013)

In action plane, X_n axis denotes action plane's normal, X_{nt} denotes axis transverse fiber direction and X_{n1} denotes axis parallel to fiber direction. σ_n, τ_{nt} and τ_{n1} are acting on the action plane where σ_n is normal stress and, τ_{nt} & τ_{n1} are shear stress transverse to fiber direction (through thickness direction) and shear stress parallel to fiber direction, respectively. Thus, σ_n is similar to $\sigma_\perp$, τ_{nt} is similar to $\tau_{\perp\perp}$ and τ_{n1} is similar to $\tau_{\perp\parallel}$. Subscript n denotes all the stresses acting on the same action plane. Whereas, subscripts

1 and t denote parallel to fiber direction and transverse to fiber direction, respectively.

The resistance of the action plane is basically denoted by (R^A). To be precise, failure resistance of an action plane against $\sigma_{\perp}^{t,c}$, τ_{nt} and τ_{n1} are denoted as $R_{\perp}^{At,Ac}$, $R_{\perp\perp}^{A}$ and $R_{\perp\parallel}^{A}$, respectively. Please note that, the superscripts t and c denote tension and compression, respectively. The difference between the material strength (resistance against up to failure at any point within the sample) and resistance of the action plane (maximum bearable stress resultant causing failure on the action plane) has to be emphasized here. If failure occurs on the action plane, then that action plane is denoted as failure plane. To calculate the failure resistance of action plane, it must be known whether the failure occurs in that action plane or not. Details of the calculation of failure resistance of action planes are given in Section 4.2.1.

In Puck's Failure Criteria, there are three stresses σ_n, τ_{nt} and τ_{n1} acting on the action plane. From micro-mechanical point of view, the behavior under the influence of shear stresses τ_{nt} and τ_{n1} are different. Once the stresses τ_{nt} and τ_{n1} are used separately in the analysis, they can be combined into one shear stress $\tau_{n\Psi}$ as

$$\tau_{n\Psi} = \sqrt{(\tau_{nt})^2 + (\tau_{n1})^2} \tag{4.1}$$

where subscript n denotes action plane and subscript Ψ denotes the angle between τ_{nt} and τ_{n1}. By this simplification, on the action plane one shear and one normal stress are obtained.

Since, Puck's Failure Criteria is based on the concept of action plane, for general $3D$ state of stress there is infinitely many number of action planes which are potentially failure plane. Among all those action planes, the one with the highest risk of failure is denoted as the failure plane and; the angle of the failure plane is denoted as the failure angle, designated as θ_{fp}. Thus, to carry out failure analysis, action plane has to be identified.

To calculate the risk of failure, the stress vector $\boldsymbol{\sigma} = \{\sigma_n, \tau_{nt}, \tau_{n1}\}$ on the action plane has to be stretched by a factor. By this scaling, stress vector reaches the stress values which would cause failure on that action plane. That factor is called as stretch factor, and designated as f_s. On the action planes without any stress or only compressive normal stress (σ_n^c), f_s takes value of ∞, which causes numerical problems. To overcome such issues, reciprocal value of f_s, so-called exposure factor, f_E, is used. Exposure factor (f_E) increases linearly with applied stress, and it is the direct measure for the risk of failure on the action plane. The action plane with the highest f_E is obtained by calculating f_E

for large number of planes, see Figure 4.4. This search for the largest f_E is one of the drawbacks of Puck model, and increases computational cost significantly. There are a number of methods for calculating the largest value of f_E in (Schirmaier et al., 2014; Thomson et al., 2017; Wiegand et al., 2008). In this thesis, Extended Golden Section Search (EGSS) Algorithm is used to reduce the computational costs. In fact EGSS is an optimization algorithm and its details and the way it is implemented are presented in previous sections.

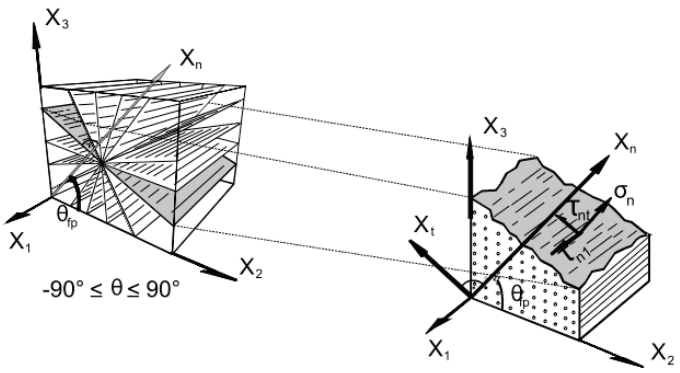

Figure 4.4. Angle Search (Knops, 2008)

4.2.1. Inter Fiber Failure

Since failure analysis is performed on the action plane, applied stresses must be transformed to action plane's local coordinate system. To do that, the following transformation

$$\begin{bmatrix} \sigma_n(\theta) \\ \tau_{nt}(\theta) \\ \tau_{n1}(\theta) \end{bmatrix} = \begin{bmatrix} \cos(\theta)^2 & \sin(\theta)^2 & 0 & 0 & 2\cos(\theta)\cos(\theta) \\ -\cos(\theta)\sin(\theta) & \cos(\theta)\sin(\theta) & 0 & 0 & \cos(\theta)^2 - \sin(\theta)^2 \\ 0 & 0 & \cos(\theta) & \sin(\theta) & 0 \end{bmatrix} \begin{bmatrix} \sigma_2 \\ \sigma_3 \\ \tau_{12} \\ \tau_{13} \\ \tau_{23} \end{bmatrix} \quad (4.2)$$

is used. If applied stress causes only tensile σ_n^t on any plane, then the failure occurs at the plane with the largest σ_n^t. Such behavior is called as intrinsically brittle behavior (Paul, 1960). Due to intrinsically brittle nature of unidirectional composites, under such circumstances, material's strength $(R_\perp^t)$ equals to failure resistance of the action plane

$(R_{\perp}^{At})$, i.e.,

$$R_{\perp}^{t} = R_{\perp}^{At} \tag{4.3}$$

In case of $\tau_{\perp\parallel}$, embedded fibers force failure to occur in a fiber parallel to action plane. Then the action plane of $\tau_{\perp\parallel}$ has the largest $\tau_{\perp\parallel}$. Thus, failure occurs in the action plane of $\tau_{\perp\parallel}$. This yields,

$$R_{\perp\parallel} = R_{\perp\parallel}^{A} \tag{4.4}$$

In case of pure $\tau_{\perp\perp}$ stressing, rather than it's action plane, failure occurs in an oblique plane. Thus, calculating failure resistance of the action plane $(R_{\perp\parallel}^{A})$ is quite difficult. $R_{\perp\perp}^{A}$ is calculated by imposing σ_n^c, which causes failure at a failure angle of $\theta_{fp} = \pm 53^{\circ}$ due to $\tau_{\perp\perp}$. Although the largest $\tau_{\perp\perp}$ is obtained when $\theta = 45^{\circ}$, the presence of σ_n^c at the same plane impedes failure (Knops, 2008). Then, with the reduced value of σ_n^c, failure occurs at an angle of $\theta \approx \pm 53^{\circ}$. Since $R_{\perp\perp}^{A}$ is calculated by imposing σ_n^c, to calibrate the strength value, an inclination parameter $(p_{\perp\perp}^{c})$ is introduced by which $R_{\perp\perp}^{A}$ is calculated as,

$$R_{\perp\perp}^{A} = \frac{R_{\perp}^{c}}{2\left(1 + p_{\perp\perp}^{c}\right)} \tag{4.5}$$

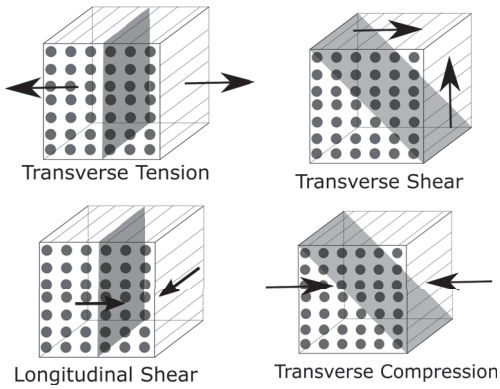

Figure 4.5. Type of stress and related failure plane (Grey areas are failure planes)

By using action plane stresses $\left(\sigma_n^{t,c}, \tau_{nt}, \tau_{n1}\right)$, and related action plane strengths $\left(R_{\perp}^{At,c}, R_{\perp\perp}^{A}, R_{\perp\parallel}^{A}\right)$ a $3D$ surface that envelopes all admissible stresses can be constructed.

This $3D$ surface is called as Master Fracture Body (MFB) (Figure 4.6) (Knops, 2008). As a result of different behavior under the influence of σ_n^t and σ_n^c, MFB consists of two parts joining at $\sigma_n = 0$ plane, τ_{nt}-τ_{n1} plane (Puck et al., 2002).

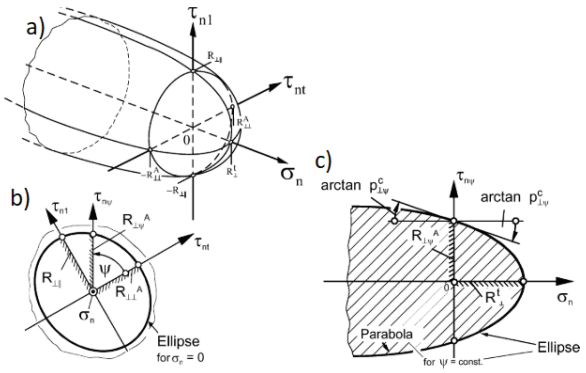

Figure 4.6. Master Fracture Body (Knops, 2008)

Since both τ_{nt} and τ_{n1} acts on the same fiber-parallel action plane, related action plane strengths $R^A_{\perp\perp}, R^A_{\perp\parallel}$ must be similar. Thus, Puck assumed simple elliptical failure criterion for combined τ_{nt}-τ_{n1} stress state $(\tau_n\Psi)$, when $\sigma_n = 0$. A failure ellipse is defined

$$\left(\frac{\tau_n\Psi}{R^A_{\perp\Psi}}\right)^2 = \left(\frac{\tau_{n1}}{R^A_{\perp\parallel}}\right)^2 + \left(\frac{\tau_{nt}}{R^A_{\perp\perp}}\right)^2 = 1 \text{ for } \sigma_n = 0 \tag{4.6}$$

at the plane corresponding to $\sigma_n = 0$. To calculate f_E, stress vector on the action plane is stretched. The direction of the stress vector does not change when it is stretched (Knops, 2008). Thus, the extension of stress vector takes place in the longitudinal sections. Hence, after fixing the cross section at $\sigma_n = 0$, longitudinal sections are employed for constructing the rest of MFB. As a result of this simplification, the computational cost of the calculation of f_E is reduced substantially (Knops, 2008).

It is experimentally observed (Deuschle and Kröplin, 2012) that in-plane shear stress combinations (σ_2-τ_{21}) causes failure in their action plane (i.e. failure angle $\theta_{fp} = 0$). This is valid for all positive range of σ_2 and negative range with the limit of $-0.4R^c_\perp$. Thus, for the range of $-0.4R^c_\perp < \sigma_2 < +\infty$, it is observed that $\sigma_n = \sigma_2; \tau_{n1} = \tau_{21}; \tau_{nt} = 0$. That means, all the failures are placed on the $\tau_{nt} = 0$ plane, see Figure 4.6. For the positive range of σ_n, failure envelope is described by an ellipse. Ellipse cuts σ_n axis perpendicularly at $R^{At}_\perp$, and cuts τ_{n1} axis with the declining slope of $\frac{\partial\tau_{n1}}{\partial\sigma_n} = -0.3$ at $\pm R^A_{\perp\parallel}$, see Figure 4.6. On the other hand, for the negative range of σ_n, parabolic contour lines are used to describe

the failure envelope. This completes the general form of MFB construction for a constant Ψ value.

For positive σ_n, MFB looks like a culotte with utmost point on the σ_n axis at $\sigma_n = R_{\perp}^{At}$ and $\tau_{n\Psi} = 0$. For negative σ_n values, MFB looks like an open, slightly widening tunnel. This corresponds to the fact that, σ_n^c can never cause failure alone, e.g. some amount of $\tau_{n\Psi}$ is always necessary for failure initiation. In the light of previous discussions, MFB is described by the following ellipse equation,

$$\left(\frac{\tau_{n\Psi}}{R_{\perp\Psi}^{A}}\right)^2 + c_1\frac{\sigma_n}{R_{\perp}^{At}} + c_2\left(\frac{\sigma_n}{R_{\perp}^{At}}\right)^2 = 1 \text{ for } \sigma_n \geq 0 \tag{4.7}$$

for positive σ_n values, and for negative values of σ_n, MFB is described by means of parabola with the following equation,

$$\left(\frac{\tau_{n\Psi}}{R_{\perp\Psi}^{A}}\right)^2 + c\sigma_n = 1 \text{ for } \sigma_n < 0 \tag{4.8}$$

The ellipse in Equation 4.7 has the anchor points $R_{\perp}^{At}$ on σ_n axis and $\pm R_{\perp\Psi}^{A}$ on the $\tau_{n\Psi}$ axis.

From geometric relations it is observed that $\tau_{nt} = \tau_{n\Psi}\cos(\Psi)$ and $\tau_{n1} = \tau_{n\Psi}\sin(\Psi)$. Then by using those relations with Equation 4.6 yields the following,

$$\left(R_{\perp\Psi}^{A}\right)^2 = \left(\frac{\cos(\Psi)}{R_{\perp\perp}^{A}}\right)^2 + \left(\frac{\sin(\Psi)}{R_{\perp\parallel}^{A}}\right)^2 \tag{4.9}$$

Even though the ellipse crosses σ_n axis perpendicularly, as experimentally observed it must cross $\tau_{n\Psi}$ with a certain inclination (Puck et al., 2002). Therefore, so-called inclination parameter $p_{\perp\Psi}^{t}$ is introduced,

$$\left(\frac{\partial\tau_{n\Psi}}{\partial\sigma_n}\right)_{\sigma_n=0}^{ellipse} = \begin{cases} -p_{\perp\Psi}^{t}, & \text{if } \tau_{n\Psi} > 0. \\ p_{\perp\Psi}^{t}, & \text{if } \tau_{n\Psi} < 0. \end{cases} \tag{4.10}$$

Parabola for describing MFB starts at anchor points of $\sigma_n = 0$ and $\tau_{n\Psi} = \pm R_{\perp\Psi}^{A}$ and its inclination parameters may be slightly different from ellipse's inclination parameters. Therefore another inclination parameter $p_{\perp\Psi}^{c}$ is introduced to describe the slope at $\sigma_n = 0$

as,

$$\left(\frac{\partial \tau_{n\Psi}}{\partial \sigma_n}\right)^{parabola}_{\sigma_n=0} = \begin{cases} -p^c_{\perp\Psi}, & \text{if } \tau_{n\Psi} > 0. \\ p^c_{\perp\Psi}, & \text{if } \tau_{n\Psi} < 0. \end{cases} \tag{4.11}$$

It is worthy to note that these inclination parameters need to be identified experimentally. Finally by using inclinations and anchor points c, c_1 and c_2 are calculated and the following results

$$c = 2\frac{p^c_{\perp\Psi}}{R^A_{\perp\Psi}} \tag{4.12}$$

$$c_1 = 2\frac{p^c_{\perp\Psi} R^{At}_{\perp}}{R^A_{\perp\Psi}} \tag{4.13}$$

$$c_2 = 1 - 2\frac{p^c_{\perp\Psi} R^{At}_{\perp}}{R^A_{\perp\Psi}} \tag{4.14}$$

are obtained. If inclination angle (Ψ) is $90°$, which corresponds to longitudinal section of MFB where only (σ_n, τ_{n1}) are acting, then $p^t_{\perp\Psi}$ and $p^c_{\perp\Psi}$ are denoted as $p^t_{\perp\parallel}$ and $p^c_{\perp\parallel}$, respectively. Similarly, if Ψ is $90°$, $p^t_{\perp\Psi}$ and $p^c_{\perp\Psi}$ becomes $p^t_{\perp\perp}$ and $p^c_{\perp\perp}$, respectively. Some recommended values for $p^t_{\perp\parallel}$, $p^c_{\perp\parallel}$, $p^t_{\perp\perp}$ and $p^c_{\perp\perp}$ are given in Table 4.1.

	$p^t_{\perp\parallel}$	$p^c_{\perp\parallel}$	$p^t_{\perp\perp}$, $p^c_{\perp\perp}$
CFRP	0.30	0.25	0.20 to 0.25
GFRP	0.35	0.30	0.25 to 0.30

Table 4.1. Recommended inclination parameters (Puck and Schürmann, 2002)

By using the specific inclination parameter values at $\Psi = 90°$ and $\Psi = 0°$, Puck proposed the following interpolation procedure to define $p^{t,c}_{\perp\Psi}$

$$\frac{p^{t,c}_{\perp\Psi}}{R^A_{\perp\Psi}} = \frac{p^{t,c}_{\perp\perp}}{R^A_{\perp\perp}} \cos^2(\Psi) + \frac{p^{t,c}_{\perp\parallel}}{R^A_{\perp\parallel}} \sin^2(\Psi) \tag{4.15}$$

for arbitrary Ψ values where,

$$\cos^2(\Psi) = \frac{\tau_{nt}^2}{\tau_{nt}^2 + \tau_{n1}^2} \tag{4.16}$$

$$\sin^2(\Psi) = \frac{\tau_{n1}^2}{\tau_{nt}^2 + \tau_{n1}^2} \tag{4.17}$$

MFB is completely defined by Equations 4.6, 4.7 and 4.8. Since the failure criteria is met when the right hand sides of these equations reached to unity, they described the failure state. Stated differently, whenever one of Equations 4.6, 4.7, 4.8 is satisfied by the stress components, failure is reached. As mentioned previously, stress exposure factor f_E, can be conveniently used to assess the failure risk at a material point. However in combination with Equations 4.6, 4.7, 4.8, the determination of f_E is not straightforward. The failure criteria expressed by these equations and stress exposure factor only coincide if the failure criteria is homogeneous in the first degree with respect to stress. Only in this special case, Equations 4.6, 4.7, 4.8 can be used as a direct measure of failure risk (Knops, 2008). In case of homogeneous in the first degree functions, the factor α can be factored out when the independent variables (e.g., stress components) of the function are all scaled by α. This fits well to the concept of stress exposure factor, which reflects the required scaling factor to reach failure and requires a function of homogeneous in the first degree. It can be shown that, if linear (L) and quadratic (Q) terms are present in the failure criteria, stress exposure factor f_E can be written as (Knops, 2008),

$$f_E = \frac{1}{2}\left(\sum L + \sqrt{\sum L^2 + 4\sum Q}\right) \tag{4.18}$$

Therefore combining Equation 4.18 and Equations 4.6, 4.7, 4.8, stress exposure factors for Puck's Inter Fiber Failure for tension and compression are defined as,

$$\begin{aligned} f_{E,IFF}^{+}(\theta) = &\sqrt{\left[\left(\frac{1}{R_{\perp}^{At}} - \frac{p_{\perp\Psi}^{t}}{R_{\perp\Psi}^{A}}\right)\sigma_n(\theta)\right]^2 + \left(\frac{\tau_{nt}(\theta)}{R_{\perp\Psi}^{A}}\right)^2 + \left(\frac{\tau_{n1}(\theta)}{R_{\perp\Psi}^{A}}\right)^2} + \\ &\frac{p_{\perp\Psi}^{t}}{R_{\perp\Psi}^{A}}\sigma_n(\theta) \text{ for } \sigma_n \geq 0 \end{aligned} \tag{4.19}$$

$$f_{E,IFF}^{-}(\theta) = \sqrt{\left(\frac{\tau_{nt}(\theta)}{R_{\perp\perp}^{A}}\right)^2 + \left(\frac{\tau_{n1}(\theta)}{R_{\perp\parallel}^{A}}\right)^2 + \left(\frac{p_{\perp\Psi}^{c}}{R_{\perp\Psi}^{A}}\sigma_n(\theta)\right)^2} + \frac{p_{\perp\Psi}^{c}}{R_{\perp\Psi}^{A}}\sigma_n(\theta) \text{ for } \sigma_n < 0 \tag{4.20}$$

where,

$$\frac{p_{\perp\Psi}^{c}}{R_{\perp\Psi}^{A}} = \frac{p_{\perp\perp}^{t,c}}{R_{\perp\perp}^{A}}\cos^2\Psi + \frac{p_{\perp\parallel}^{t,c}}{R_{\perp\parallel}^{A}}\sin^2\Psi \tag{4.21}$$

Obviously failure angle θ_{fp} is the one which satisfies,

$$f_{E,IFF}(\theta_{fp}) = \max\left(f_{E,IFF}(\theta)\right) \tag{4.22}$$

The search of failure angle is a computationally demanding task that has to be repeated at every material point during analysis. The simplest approach is based on scanning the interval $[-90^\circ \quad 90^\circ]$ by means of a small incremental value (e.g. with an increment of 1° in Deuschle's work (Deuschle and Puck, 2013) and 0.1° in Reinoso's work (Reinoso et al., 2017)) and for each value calculating the exposure factor. Instead of testing each action plane and finding the largest exposure factor, an optimization method can be employed.

Golden Section Search Method (GSSM) is one of the available optimization methods to reduce the computational cost of Puck's Failure Model (Vinícius et al., 2018; Wang et al., 2018). The Golden Section Search, which is maximization/minimization technique, can be applied to functions, where an extreme is known to exist within the given range. In GSSM, by evaluating the function in triples of points, the search range is successively narrowed. The distances between these points form golden ratios from where the method's name originates.

Referring to Figure 4.7, if the maximum is searched within the range $[\theta_1, \theta_2]$, then the third point θ_3 is computed by,

$$\frac{b}{a} = \varphi = \frac{1+\sqrt{5}}{2} \Rightarrow \theta_3 = \theta_2 + \frac{\theta_2 - \theta_1}{1+\varphi} \tag{4.23}$$

which is folllowed by the calculation of the additional point, θ_4,

$$\frac{b}{a} = \frac{a}{c} \Rightarrow \theta_4 = \theta_3 + c \tag{4.24}$$

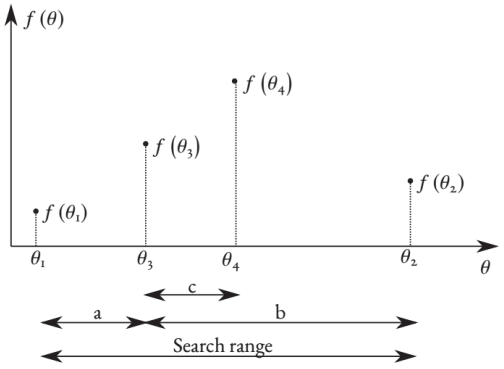

Figure 4.7. Schematic form of Golden Section Search

Equation 4.24 guarantees that θ_3 is symmetric to θ_4 in the original search range. Then, by comparing $f(\theta_3)$ and $f(\theta_4)$ new search range is chosen. If $f(\theta_3) \geq f(\theta_4)$, then new range is chosen as $[\theta_1, \theta_4]$ range. Otherwise, new range is chosen as $[\theta_3, \theta_2]$ range. This search continues until the difference between the outer points becomes tolerably small. The amount of the term tolerably small is decided with respect to expected accuracy of failure angle, θ_{fp}.

Even though, the Golden Section Search method quickly brackets the maximum of the given function, large number of iterations are required to obtain the accurate value of the maximum (i.e. θ_{fp}). To overcome this drawback, as proposed by Wiegand (Wiegand et al., 2008), a curve interpolation technique called as Inverse Parabolic Interpolation is combined with Golden Section Search Method. The new method is denoted as Extended Golden Section Search Method (EGSSM).

In Extended Golden Section Search Method, initially Golden Section Search is employed to bracket the maximum sufficiently close. Afterwards, a parabola is fit by using point triples $(\theta_1, \theta_2, \theta_3)$ to find the maximum value of function, $f\left(\theta_{fp}\right)$. The θ_{fp} term, where function becomes maximum is computed from,

$$\theta_{fp} \simeq \theta_2 - \frac{1}{2}\frac{(\theta_2-\theta_1)^2\left(f(\theta_2)-f(\theta_3)\right)(\theta_2-\theta_3)^2\left(f(\theta_2)-f(\theta_1)\right)}{(\theta_2-\theta_1)\left(f(\theta_2)-f(\theta_3)\right)(\theta_2-\theta_3)\left(f(\theta_2)-f(\theta_1)\right)} \tag{4.25}$$

Since in the Puck's Failure Model the failure angle is in the range of $\left(-90^\circ \leq \theta_{fp} \leq 90^\circ\right)$, in this thesis, EGSSM is used to find the maximum exposure factors, $\left(f^{+}_{E,IFF}, f^{-}_{E,IFF}\right)$. By this methodology numerical efficiency of the implementation is improved significantly. Algorithmic structure of EGSSS is presented in Algorithm 5.

Algorithm 5 Extended Golden Section Search Algorithm

• Define tolerance and initial values
• Compute a, b, φ and θ_3 by Equation (4.23)
• Compute c and θ_4 by Equation (4.24)
WHILE $|DIFF| > TOL$
  IF$f\ (\theta_4) > f\ (\theta_3)$
    $\theta_1 \leftarrow \theta_3$
  ELSE
    $\theta_2 \leftarrow \theta_4$
  ENDIF
  Compute a, b, φ, θ_3 and θ_4 by Equation (4.23) and (4.24)
  DIFF $\leftarrow (\theta_3 - \theta_4)$
ENDWHILE
• Compute θ_{fp} by Equation (4.25)

4.2.2. Extension of Puck's Model

As more experimental results have become available, shortcomings of the original Puck's criteria have been detected and a number of improvements have been introduced. Influence of normal stress along fiber direction on IFF and inclusion of stresses which act on parallel-to-fiber planes but not on fracture plane were considered to be the most significant ones, (Knops, 2008). In the original version, in accordance with Mohr's hypothesis, it was assumed that normal stresses parallel to fiber direction σ_1, does not influence the inter fiber fracture (IFF), i.e., matrix damage and failure. However, under normal stresses along fiber direction, premature failure of fibers might take place due to statistical nature of fiber strength and local imperfections. These failures might in turn cause local damage in the lamina in the form of debonding of matrix-fiber interfaces and alteration of damage evolution in the matrix, (Knops, 2008). These mechanisms are introduced in the extended version of Puck's model through a weakening factor η_{w1} that is used to modify stress exposure factor associated with IFF; (J. F. Chen et al., 2014; Knops, 2008). More precisely, the reduction in fracture resistance is taken into account by,

$$f_{E,IFF}^{+,-} = \frac{f_{E,IFF}^{+,-}}{\eta_{w1}} \tag{4.26}$$

which increases the exposure factor since $\eta_{w1} < 1.0$. In (Knops, 2008), a procedure that utilizes experimental results and two additional fitting parameters, is introduced to determine weakening factor. It is important to note that, this extension does not influence the identification of θ_{fp} and can be conducted as before neglecting normal stress along

the fiber direction, (Knops, 2008).

4.2.3. Fiber Failure

In his first publication, Puck assumed unidirectional laminate as homogenized material, and he used the maximum stress criteria for fiber failure. As a result of this assumption, the effects of transverse stresses were not included. Thus, using such failure criteria may yield unrealistic and unreliable results in case of $3D$ stress states. The maximum stress based fiber failure criteria defined as follows,

$$f_{EFF} = \begin{cases} \dfrac{\sigma_1}{R^t_{\parallel}} & \text{if } \sigma_1 > 0 \\ \\ \dfrac{\sigma_1}{-R^c_{\parallel}} & \text{if } \sigma_1 < 0 \end{cases}$$

Due to Poisson's effects, transverse stresses (σ_2, σ_3) influence the strain in fiber direction. Thus different stress states occur in the fiber direction under the influence of uni-axial and combined stresses. By taking this effect into account, Puck modified his fiber failure criteria such that the effects of transverse stresses are considered as well. It is observed that, the stress in the fibers is higher than the stress in matrix. This causes in-homogeneous distribution of stress. To include the effect of in-homogeneity in the stress distribution, Puck introduced the stress magnification factor $m_{\sigma f}$ with the values of 1.1 for Carbon Fiber Reinforced Polymers (CFRP) and 1.3 for Glass Fiber Reinforced Polymers (GFRP). Then, the strain in the fibers due to combined state of stress is defined as,

$$\varepsilon_{1f} = \frac{\sigma_{1f}}{E_{\parallel f}} - \frac{\nu_{\parallel\perp f}}{E_{\perp f}} m_{\sigma f} \left(\sigma_2 + \sigma_3\right) \tag{4.27}$$

where,

$$\frac{\nu_{\parallel\perp f}}{E_{\perp f}} = \frac{\nu_{\perp\parallel f}}{E_{\parallel f}} \tag{4.28}$$

$$\varepsilon_{1f} = \varepsilon_1 \tag{4.29}$$

Following that, longitudinal stress in fibers is defined as,

$$\sigma_{1f} = E_{\parallel f}\varepsilon_1 + \nu_{\parallel\perp f} m_{\sigma f}\,(\sigma_2 + \sigma_3) \;\text{ with,} \tag{4.30}$$

$$\varepsilon_1 = \frac{\sigma_1}{E_\parallel} - \frac{\nu_{\perp\parallel}}{E_\parallel}\,(\sigma_2 + \sigma_3) \tag{4.31}$$

$$R_{\parallel f} = \frac{E_{\parallel f}}{E_\parallel} R_\parallel \tag{4.32}$$

If longitudinal strain ε_1 is combined with the elastic law of UD lamina (Equation 4.32) and the fiber stress σ_{1f} is replaced by the failure strength of fiber $R_{\parallel f}$; the following Fiber Failure condition

$$f^+_{E,FF} = \frac{1}{R^t_\parallel}\left[\sigma_1 - \left(\nu_{\perp\parallel} - \nu_{\perp\parallel} m_{\sigma f}\frac{E_\parallel}{E_{\parallel f}}\right)(\sigma_2 + \sigma_3)\right] \tag{4.33}$$

$$f^-_{E,FF} = \frac{1}{-R^c_\parallel}\left[\sigma_1 - \left(\nu_{\perp\parallel} - \nu_{\perp\parallel} m_{\sigma f}\frac{E_\parallel}{E_{\parallel f}}\right)(\sigma_2 + \sigma_3)\right] \tag{4.34}$$

is obtained.

4.3. Modeling Framework and Incorporation of Damage

In conventional analysis, the initiation of failure i.e., fulfillment of the failure criteria, is considered to be the complete failure at a material and typically also the complete failure of the structural component. This in turn implies that the potential capacity of a component after failure initiation is neglected. However, this capacity could reach to non-negligible levels particularly for multi-ply composite components. In this section, continuum damage mechanics along with Puck's failure criteria is going to be used as the main framework to address the complete stress-strain response of a component at lamina level.

4.3.1. Incorporation of Damage

The focus is on matrix failure since a large fraction of observed failures are controlled primarily by matrix failure. Since Puck's model distinguishes between compressive and tensile failure IFF, two different damage variables associated with tension (D^+_m) and compression (D^-_m) are going to be specified. In combination with these damage variables,

effective stress concept is used to define the stress at a material point as,

$$\boldsymbol{\sigma} = \tilde{\boldsymbol{\sigma}}_f + (1 - D_m^+)(1 - D_m^-)\, \tilde{\boldsymbol{\sigma}}_m \tag{4.35}$$

Where, $\tilde{\boldsymbol{\sigma}}_f$ and $\tilde{\boldsymbol{\sigma}}_m$ are elastic stress tensors, i.e. stress response without any damage, for fiber and matrix, respectively. Since any damage in fibers is disregarded, there is no damage term for $\tilde{\boldsymbol{\sigma}}_f$ in Equation 4.35. For the computations of $\tilde{\boldsymbol{\sigma}}_f$ and $\tilde{\boldsymbol{\sigma}}_m$, elastic stiffness tensor $\tilde{\boldsymbol{C}}$ is decoupled into $\tilde{\boldsymbol{C}}_f$ and $\tilde{\boldsymbol{C}}_m$, such that $\tilde{\boldsymbol{C}} = \tilde{\boldsymbol{C}}_f + \tilde{\boldsymbol{C}}_m$. For the computation of $\tilde{\boldsymbol{C}}$ elastic stiffness tensor for orthotropic materials

$$\tilde{\boldsymbol{C}} = \begin{bmatrix} C_{11} & C_{12} & C_{13} & 0 & 0 & 0 \\ C_{21} & C_{22} & C_{23} & 0 & 0 & 0 \\ C_{31} & C_{32} & C_{33} & 0 & 0 & 0 \\ 0 & 0 & 0 & C_{44} & 0 & 0 \\ 0 & 0 & 0 & 0 & C_{55} & 0 \\ 0 & 0 & 0 & 0 & 0 & C_{66} \end{bmatrix} \tag{4.36}$$

is used. The explicit form of these coefficients are given as,

$$\begin{aligned}
C_{11} &= E_1(1 - \nu_{23}\nu_{32})\Upsilon \\
C_{22} &= E_2(1 - \nu_{13}\nu_{31})\Upsilon \\
C_{33} &= E_3(1 - \nu_{12}\nu_{21})\Upsilon \\
C_{12} &= E_1(\nu_{21} + \nu_{31}\nu_{23})\Upsilon = E_2(\nu_{12} + \nu_{32}\nu_{13})\Upsilon \\
C_{13} &= E_1(\nu_{31} + \nu_{21}\nu_{32})\Upsilon = E_3(\nu_{13} + \nu_{12}\nu_{23})\Upsilon \\
C_{23} &= E_2(\nu_{32} + \nu_{12}\nu_{31})\Upsilon = E_3(\nu_{23} + \nu_{21}\nu_{13})\Upsilon \\
C_{44} &= G_{12}, C_{55} = G_{13}, C_{55} = G_{23} \\
C_{21} &= C_{12}, C_{31} = C_{13}, C_{32} = C_{23} \\
\Upsilon &= \frac{1}{1 - \nu_{12}\nu_{21} - \nu_{32}\nu_{23} - \nu_{31}\nu_{13} - 2\nu_{21}\nu_{32}\nu_{13}}
\end{aligned}$$

$\tilde{\boldsymbol{C}}_f$ and $\tilde{\boldsymbol{C}}_m$ are extracted from $\tilde{\boldsymbol{C}}_f$ as

$$\tilde{\boldsymbol{C}}_m = \begin{bmatrix} 0 & C_{12} & C_{13} & 0 & 0 & 0 \\ C_{21} & C_{22} & C_{23} & 0 & 0 & 0 \\ C_{31} & C_{32} & C_{33} & 0 & 0 & 0 \\ 0 & 0 & 0 & C_{44} & 0 & 0 \\ 0 & 0 & 0 & 0 & C_{55} & 0 \\ 0 & 0 & 0 & 0 & 0 & C_{66} \end{bmatrix}; \; \tilde{\boldsymbol{C}}_f = \begin{bmatrix} C_{11} & 0 & 0 & 0 & 0 & 0 \\ 0 & 0 & 0 & 0 & 0 & 0 \\ 0 & 0 & 0 & 0 & 0 & 0 \\ 0 & 0 & 0 & 0 & 0 & 0 \\ 0 & 0 & 0 & 0 & 0 & 0 \\ 0 & 0 & 0 & 0 & 0 & 0 \end{bmatrix} \tag{4.37}$$

which simply means that the normal contribution related to fibers is decoupled from matrix response. Hence, matrix damage is applied to only matrix related parts.

At this point, it is convenient to recall that for Puck's failure criteria $f^{+,-}_{E,IFF}$ are the indicators of failure risk at a material point. Therefore, it is reasonable to relate damage initiation and evolution to $f^{+,-}_{E,IFF}$. For this purpose, history variables $r^{+}_{E,IFF}$ and $r^{-}_{E,IFF}$ are introduced. These variables in fact the largest exposure factors ever reached at a material point. They are formally defined as,

$$\begin{aligned} r^{+}_{E,IFF} &= max\left(f^{+}_{E,IFF}\left(\tau\right)\right) \qquad \tau \leq t \\ r^{-}_{E,IFF} &= max\left(f^{-}_{E,IFF}\left(\tau\right)\right) \qquad \tau \leq t \end{aligned} \tag{4.38}$$

Where τ is time-like parameter used to parametrize the loading. Damage initiation and evolution can be conveniently described by adopting exponential laws,

$$\begin{aligned} D^{+}_{m} &= 1 - \frac{r^{+}_{init}}{r^{+}_{E,IFF}}\left(1 - \alpha^{+} + \alpha^{+} exp\left(-\beta^{+}\left(r^{+}_{E,IFF} - r^{+}_{init}\right)\right)\right) \\ D^{-}_{m} &= 1 - \frac{r^{-}_{init}}{r^{-}_{E,IFF}}\left(1 - \alpha^{-} + \alpha^{-} exp\left(-\beta^{-}\left(r^{-}_{E,IFF} - r^{-}_{init}\right)\right)\right) \end{aligned} \tag{4.39}$$

Where r^{+}_{init} and r^{-}_{init} are initiation thresholds and both set to unity. It is important to realize that in this form the description is local and can be implemented in Abaqus as a user defined material model through UMAT subroutine (Systemes, 2013). In fact, algorithmic structure of the local version is concisely presented in Algorithm 6.

Even-though such implementations seem very attractive, unless some precautions are taken, they are prone to mesh dependency problems, (Dean et al., 2020; Peerlings et al., 1998; Reinoso et al., 2017). To illustrate pathological mesh dependency, tension hole specimen shown in Figure 4.8, is analyzed by using the local damage mechanics summarized in this sub-section. In Figure 4.8, total reaction versus displacement graphs

Algorithm 6 Implementation of Puck's Failure Criteria in local sense

- Update Internal Variables
- Compute $\tilde{\boldsymbol{C}}$ and $\tilde{\boldsymbol{\sigma}}$.
- Construct $\tilde{\boldsymbol{C}}_m, \tilde{\boldsymbol{C}}_f, \tilde{\boldsymbol{\sigma}}_f$ and $\tilde{\boldsymbol{\sigma}}_m$

Compute Fiber exposure factors.
IF No Matrix Damage has been initiated yet
  ▷ Compute θ_{fp}
  ▷ Compute Action plane stresses
  ▷ Compute Matrix Exposure Factors
ELSE
  ▷ Use θ_{fp} from previous step
  ▷ Compute Action plane stresses
  ▷ Compute Matrix Exposure Factors
ENDIF

- Compute Damages
- Update Stress tensor
- Compute Material stiffness tensor
- Store History variables

are presented for four different element sizes, e.g. $1.0, 1.5, 3.0$ and 4.0 mm. As the element sizes decreases, the total dissipation which is proportional with the area under the force-displacement curve, decreases and there is clearly no tendency of convergence.

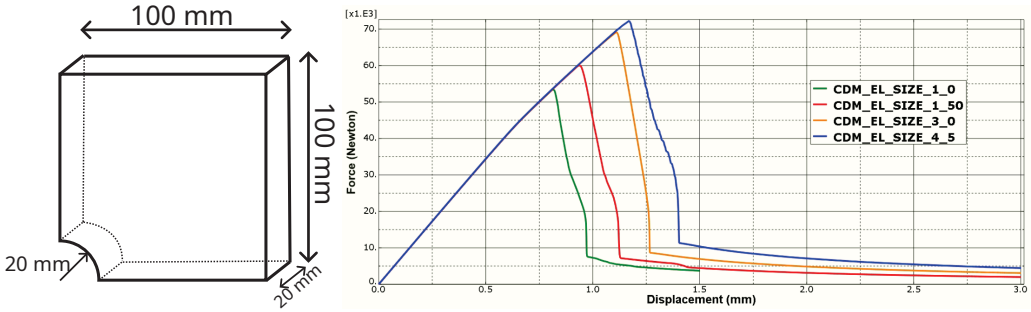

Figure 4.8. Left: Dimensions of open hole tension specimen; Right: Force-displacement response for four different elment sizes

A practical remedy to resolve pathological mesh dependency problem was proposed by Bazant (Bažant and Oh, 1983) and is known as the crack band approach. In this method, dissipation characteristics are correlated with the element size used to solve the specific problem under consideration. The implementation of the method is rather straight forward and solves the mesh dependency problem observed in force-displacement graphs. However, crack band method yields crack/damage bands which are aligned with the specific mesh used. In Figure 4.9, predicted band directions with two different meshes

are shown. It is important to emphasize that these responses correspond to the same physical problem, which are supposed to be very close in terms of predicted crack/damage bands.

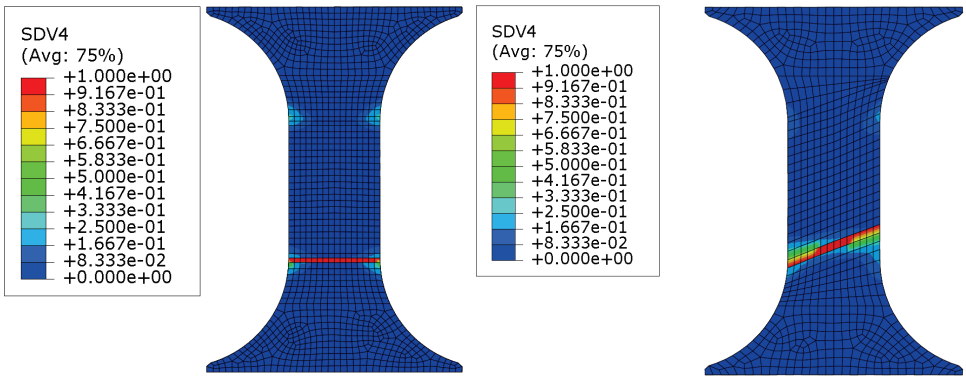

Figure 4.9. Crack patterns due to mesh alignments

In the next section, localizing implicit gradient damage formulation is going to be used which alleviates the mesh dependency observed both in force-displacement response and crack/damage band orientation predictions.

4.4. Localizing Implicit Gradient Damage Based Treatment

As stated in Section 4.3.1, failure initiation in Pcuk's criteria are described by non-dimensional exposure factors. Therefore it is reasonable to link damage initiation and evolution to these factors. Furthermore, in order to suppress mesh dependency, non-local exposure factors, $\left(\bar{f}^{+}_{E,IFF} \text{ and } \bar{f}^{-}_{E,IFF}\right)$, are introduced which are the key field variables in the description of damage evolution. To set-up a consistent framework, first non-local threshold values $\bar{r}^{+}_{E,IFF}$ and $\bar{r}^{-}_{E,IFF}$ are introduced. These threshold values take the initial value of one; and their evolution is described by the corresponding non-local exposure factors. Once the related non-local exposure factor exceeds value of one, the corresponding non-local threshold values takes that value. For that purpose, the following Karush Kuhn Tucker (KKT) conditions

$$\begin{aligned} \dot{\bar{r}}^{+}_{E,IFF} \geq 0; \bar{f}^{+}_{E,IFF} - \bar{r}^{+}_{E,IFF} \leq 0; \dot{\bar{r}}^{+}_{E,IFF}\left(\bar{f}^{+}_{E,IFF} - \bar{r}^{+}_{E,IFF}\right) = 0 \\ \dot{\bar{r}}^{-}_{E,IFF} \geq 0; \bar{f}^{-}_{E,IFF} - \bar{r}^{-}_{E,IFF} \leq 0; \dot{\bar{r}}^{-}_{E,IFF}\left(\bar{f}^{-}_{E,IFF} - \bar{r}^{-}_{E,IFF}\right) = 0 \end{aligned} \tag{4.40}$$

are used. By the KKT conditions in Equation (4.40) each non-local threshold value, $\bar{r}^{+}_{E,IFF}$ and $\bar{r}^{-}_{E,IFF}$, are forced to be largest of related non-local exposure factor, $\bar{f}^{+}_{E,IFF}$ and $\bar{f}^{-}_{E,IFF}$. Hence the largest values of $\bar{f}^{+}_{E,IFF}$ and $\bar{f}^{-}_{E,IFF}$ are utilized for the initiation and evolution of each damage term.

As opposed to local formulations, in gradient type formulations, non-local fields, in the current context non-local exposure factors for tension $\bar{f}^{+}_{E,IFF}$ and for compression, $\bar{f}^{-}_{E,IFF}$ appear as new fields, i.e. variables, in the problem formulation. As shown by Poh (Poh and Sun, 2017), localizing implicit gradient damage formulation results in the following partial differential equations

$$\begin{aligned} \bar{f}^{+}_{E,IFF} - \nabla \cdot \left(g\left(D^{+}\right) l_c^2 \nabla \left(\bar{f}^{+}_{E,IFF} \right) \right) - f^{+}_{E,IFF} = 0 \\ \bar{f}^{-}_{E,IFF} - \nabla \cdot \left(g\left(D^{-}\right) l_c^2 \nabla \left(\bar{f}^{-}_{E,IFF} \right) \right) - f^{-}_{E,IFF} = 0 \end{aligned} \tag{4.41}$$

governing the distribution of non-local fields, where g is damage dependent interaction function and l_c is the internal length scale controlling the extent of non-locality. It is important to emphasize that Equations 4.41 are derived in a consistent manner by using higher-order continuum mechanics arguments and thermo-dynamically consistent. For each PDE standard Neumann type Boundary Conditions presented in Equation (4.42) are used.

$$\begin{aligned} \nabla \left(\bar{f}^{+}_{E,IFF} \right) \cdot \boldsymbol{n} = 0 \\ \nabla \left(\bar{f}^{-}_{E,IFF} \right) \cdot \boldsymbol{n} = 0 \end{aligned} \tag{4.42}$$

Interaction function initially takes value of one and with further evolution in related damage value takes very small values (Poh and Sun, 2017) . Furthermore, for an arbitrary damage of D, the interaction function can be described as follows,

$$g = \frac{(1-R)\exp\left(\eta D\right) + R - \exp\left(-\eta\right)}{1 - \exp\left(-\eta\right)} \tag{4.43}$$

where η and R are model parameters which describe the rate of reduction in g and the residual value of g once related damage variable reaches unity, respectively. It is also worth mentioning that if the value of one is assigned to R, then Conventional Implicit Gradient Damage model is retrieved. In the thesis R value of 0.005 is used (Poh and Sun, 2017; Sarkar et al., 2019). It must also be mentioned that for both PDEs in Equation (4.41), the same g function with different damage variables are used.

4.5. Finite Element Implementation

In a geometrically linear setting, as long as no body force is applied, the static equilibrium of a deformable body is described by,

$$\nabla \cdot \boldsymbol{\sigma} = \mathbf{0} \tag{4.44}$$

As mentioned in Section 4.4, to achieve mesh objective results non-local counterparts of damage driving quantities must be computed. For this purpose, the PDEs in Equation (4.41) must also be solved. Thence to implement Localizing Implicit Gradient Damage model based version of Puck's criteria three PDEs in Equations (4.41) and (4.44) must be solved simultaneously.

For this purpose a user element is implemented within commercial Finite Element software Abaqus. The user element is eight noded and fully integrated brick element, which is very similar to Abaqus coupled temperature displacement element, C3D8T (Systemes, 2013). In user element implementation each node has five degrees of freedoms. First three degree of freedoms of user element are related to displacement in x, y and z directions. Whereas fourth and fifth degree of freedoms are related to non-local matrix tension exposure factor and non-local matrix compression exposure factor, respectively. To be able to use Abaqus post-processor, dummy element concept is used. For this purpose, on top of Abaqus C3D8T elements user elements are placed. Elastic response is used for dummy elements along with very small material properties (e.g. $E = 1.0E^{-12}, \nu = 0.0$), so that their effect on the resulting response is negligible. Basically, user elements and Abaqus Elements share the same geometry and connectivity. During the analysis the integration point data is copied from User Elements to a common block and written to the output database file of Abaqus by means of user defined variable (UVARM) subroutine. These results are accessible by Abaqus for post-processing purposes.

In Abaqus implementation, three coupled PDEs presented in Equations (4.41) and (4.44) are solved simultaneously. For temporal discretization, Backward Euler Algorithm is used. Hence an implicit solution scheme is utilized. For such solution schemes Abaqus uses Newton Raphson Solution Algorithm. To achieve quadratic convergence Newton Raphson Solution Algorithms requires consistent linearization of the weak forms with respect to solution (primary) variables. Upon discretization, the weak form of the governing differential equations lead to 'nodal force' balance equations designated by

$\hat{\boldsymbol{f}}_{\sigma}$, $\hat{\boldsymbol{f}}^{+}_{\boldsymbol{E,IFF}}$ and $\hat{\boldsymbol{f}}^{-}_{\boldsymbol{E,IFF}}$, respectively. Linearization of these force columns in the direction of incremental displacement and non-local variables lead to the unsymmetrical tangent stiffness matrix, $\boldsymbol{K}_{el}$. The derivation of the weak forms, and the generation of element tangent stiffness tensors are presented in Appendix.

The key components of the implementation can be split into two parts. The steps that have to be followed at material point level to obtain stress response and material tangent operators, i.e., so-called stress update algorithm at integration point level, are presented in Algorithm 7. Integration point algorithm is called within an element routine and the

Algorithm 7 Stress update algorithm at integration point level

- Load Material Properties and Internal Variables
- Load non-local variables
- Update Thresholds and Damages
- Compute Elastic Stresses

IF$\left(\bar{r}^{+}_{E,IFF} == 1.00\right)$ and $\left(\bar{r}^{-}_{E,IFF} == 1.00\right)$

- ▷ • Use Extended Golden Section Search Algorithm to compute θ_{fp}, $\bar{\sigma}_n$, $\bar{\tau}_{n1}$ and $\bar{\tau}_{nt}$
- ▷ • Compute **Local** Exposure factors $f^{+}_{E,IFF}$ and $f^{-}_{E,IFF}$

ELSE

- ▷ • Use θ_{fp} from previous step to compute $\bar{\sigma}_n$, $\bar{\tau}_{n1}$ and $\bar{\tau}_{nt}$
- ▷ • Compute **Local** Exposure factors $f^{+}_{E,IFF}$ and $f^{-}_{E,IFF}$

ENDIF

- Update Stress tensor
- Compute Tangent Terms, $\dfrac{\partial \boldsymbol{\sigma}}{\partial \boldsymbol{\varepsilon}}$, $\dfrac{\partial D^{+}}{\partial \bar{f}^{+}_{E,IFF}}$, $\dfrac{\partial D^{-}}{\partial \bar{f}^{-}_{E,IFF}}$, $\dfrac{\partial \bar{f}^{+}_{E,IFF}}{\partial \boldsymbol{\varepsilon}}$ and $\dfrac{\partial \bar{f}^{-}_{E,IFF}}{\partial \boldsymbol{\varepsilon}}$
- Update Internal Variables

corresponding element level computations are given in Algorithm 8. The performance of the formulation and the implemented element are assessed in the following section.

4.6. Assessment of the Model

In this section, firstly the mesh objectivity of the implementation is going to be investigated by means of a tension specimen. The same specimen is going to be used to highlight the significance of LIGD formulation by comparing the results obtained by LIGD and CIGD formulations. Finally, using dog bone shaped compression specimen, predictive capabilities of the model is tested particularly for damage band orientation prediction. Inclination parameters of 0.35, 0.30, 0.25 and 0.30 are assigned to $p^{t}_{\perp\perp}$, $p^{c}_{\perp\perp}$, $p^{t}_{\perp\parallel}$ and $p^{c}_{\perp\parallel}$, respectively. Strength and material properties are taken from Reinoso's study (Reinoso

Algorithm 8 Algorithmic steps of element level computations

Loop over integration points

- ▷ Calculate element matrices: $\boldsymbol{N}$, $\boldsymbol{B}$, $\bar{\boldsymbol{N}}$, $\bar{\boldsymbol{B}}$, Jacobian
- ▷ Transform Nodal values to integration points
- ▷ Call stress update algorithm (Algorithm 7)
- ▷ Update history variables
- ▷ Copy integration point data from User Elements to Dummy Element
- ▷ Compute Internal Force Column (Please see Appendix)
- ▷ Compute Element Stiffness Matrix (Please see Appendix)

End of loop over integration points

et al., 2017), and summarized in Table 4.2.

Table 4.2. Material properties for uni-directional composite

E_{11} (GPa)	$E_{22},\ E_{33}$ (GPa)	G_{12}, G_{13} (GPa)	$R^c_\perp$ (MPa)	$R^t_\perp$ (MPa)	$R_{\perp\parallel}$ (MPa)
139.7	12.9	6.9	253	44.54	106.8

Due to lack of experimental results on single ply specimens, a quantitative comparison could not be done and weakening factor associated with normal stress along the fiber direction is not taken into account, i.e., $\eta_{w1} = 1.0$.

4.6.1. Tension Specimen

To present the mesh objectivity of the implementation open hole tension specimen in Figure 4.10 is analyzed. To reduce the computation cost, $\frac{1}{8}$ of the specimen is modeled and symmetry boundary conditions are applied (Figure 4.10). To investigate the mesh objectivity, while keeping all other parameters same, open hole tension specimen is discretized with three different mesh densities under displacement applied along Y-direction, please see Figure 4.10. Displacement versus Reaction Force diagrams for three different mesh densities are presented in Figure 4.11. Force-displacement graphs are very close and almost coincident for medium and fine meshes. This result supports that the current formulation yields mesh convergent results.

By using Conventional Localizing Implicit Gradient Damage (CIGD) model, similar Displacement vs. Reaction Force diagrams may be obtained (Engelen et al., 2003; Peerlings et al., 2004). However, the localization zone obtained CIGD model may artifically widen although it should be limited to the initial band width, (Sarkar et al., 2019, 2021). Furthermore, in CIGD based models, there are some inconsistencies in damage

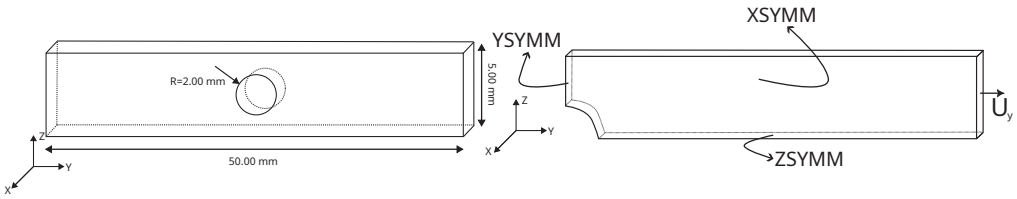

Figure 4.10. Dimensions and Boundary Conditions of Tension Specimen

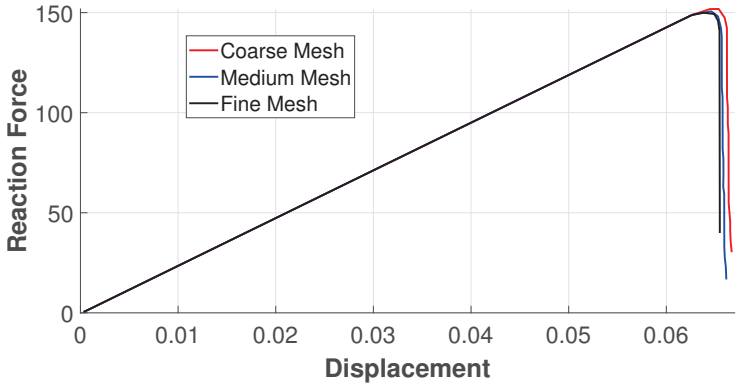

Figure 4.11. Displacement vs. Reaction Force Diagrams for different mesh sizes

initiation direction and distribution reported by different authors, e.g., (Poh and Sun, 2017; Wosatko, 2021, 2022).

To investigate the artificial widening issue, tension specimen in Figure 4.10 is discretized with the element size of 0.25 mm and internal length scale parameter, l_c, is chosen to be 0.50 mm. Afterward, specimen is analyzed with CIGD and LIGD based solution algorithms. In Figure 4.12 and Figure 4.13, step-by-step evolution of the distribution of matrix tension damage for CIGD and LIGD based algorithms are presented, respectively. For both cases damage is initiated at the same location. However, in the case of CIGD version, damage zone tend to diffuse with further deformations. Unlike CIGD, in the case of LIGD version damage localizes into a smaller volume, and this volume does not change with further deformations. Furthermore, the length of the volume in which damage is localizes almost the same as the internal length scale parameter (Figure 4.13). Therefore, it is understood that with the LIGD based implementation of Puck's failure criteria artificially widening of damage zone is prevented. Hence, physically accurate predictions matrix tension damage distribution is obtained.

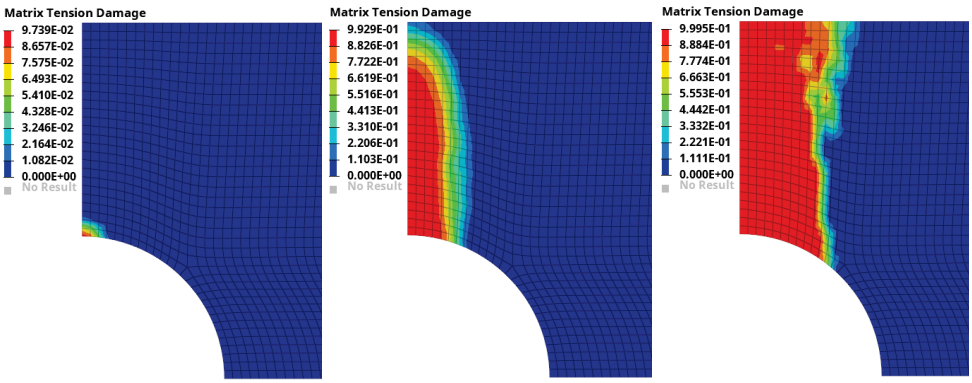

Figure 4.12. Evolution of matrix tension damage for CIGD

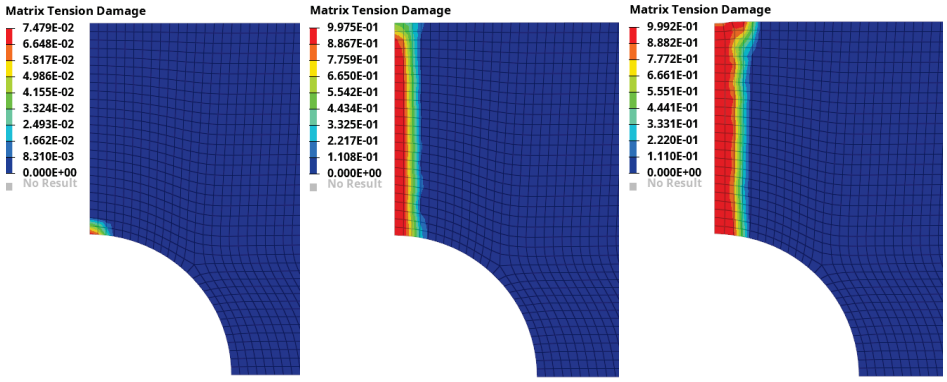

Figure 4.13. Evolution of matrix tension damage for LIGD

4.6.2. Compression Specimen

Experimental studies suggest that uni-directional composites fail with an angle of 53° under the influence of uni-axial transverse compression load (Cuntze and Freund, 2004; Kaddour and Hinton, 2013; Reinoso et al., 2017). Furthermore, at material point, Puck's Failure Criteria predicts failure angle, θ_{fp}, approximately 53° for Inter Fiber Failure under the influence of transverse uni-axial compression load (Puck et al., 2002). Therefore, transverse uni-axial compressive analysis is a good candidate to assess the predictive capabilities of the model and the implementation. It is worthy to note that crack band type regularization techniques are not successful in capturing the correct failure angle at specimen level.

Thence, in this section following Knops (Knops, 2008) a dog bone shaped specimen is modeled. The dimensions of the specimen is presented in Figure 4.14. As presented in Figure 4.14, specimen is fixed at one and and transverse uni-axial compressive load is applied from the other end. The fibers are parallel to $1(e_1)$ direction and therefore the depicted loading leads to transverse compression in the specimen.

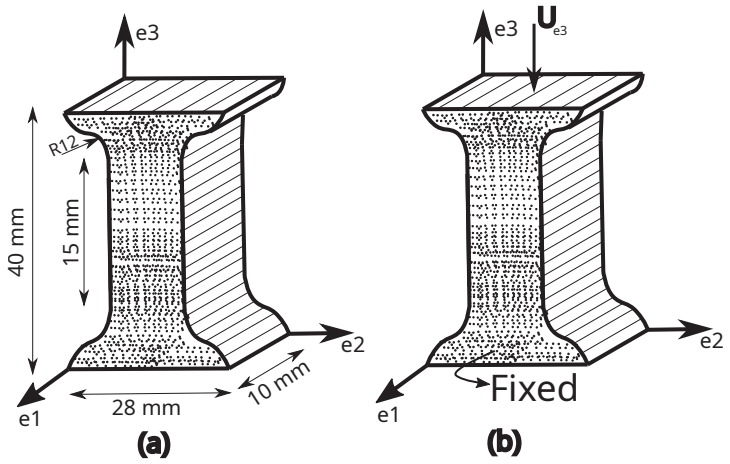

Figure 4.14. Dimensions and Boundary Conditions of Specimen (Knops, 2008)

Depending on a set of preliminary analysis, it was realized that one of the key parameters controlling the damage distribution is the internal length scale l_c. To investigate this aspect systematically, six different l_c values are considered. More precisely, dog bone specimen is discretized by element size of 0.05 mm and while keeping other material properties the same l_c sizes of $(0.10, 0.15, 0.25, 0.500, 1.000$ and 2.000 mm.) are used. The corresponding damage distributions are shown in Figure 4.15. As seen from Figure 4.15, a sufficiently small l_c value is essential to capture an inclined damage band similar to experimental results. For l_c values larger or equal to 0.50 mm damage diffuses into larger volume. Consequently, physically unrealistic results are obtained with such large l_c values. Particularly for l_c value less than or equal to 0.25 mm, the resulting damage localization band has an inclination of approximately $53°$. It is worthy to note that Puck's criteria predicts a failure angle of $53°$ at material point under transverse loading. In Figure 4.16, experimental results from Knops (Knops, 2008) and distribution of compression damage obtained with the current implementation are presented. As seen from the figure in both cases the distribution of damage has an inclination approximately $53°$. Furthermore, Knops' experimental results are in good agreement with the numerical results with small l_c values of $0.10, 0.15$ and 0.25 mm, see Figure 4.15.

To investigate the effects of element size and define the minimum element size to l_c ratio, dog bone shaped specimen in Figure 4.14 is discretized with two different element sizes of $(0.05, 0.10$ mm). Thence, while keeping other material properties the same uni-axial transverse compression load is applied to each discretization. The distribution of the compression damage for each discretization are presented in Figure 4.17. As seen from thid figure, for both discretization the distribution of compression damage is quite similar

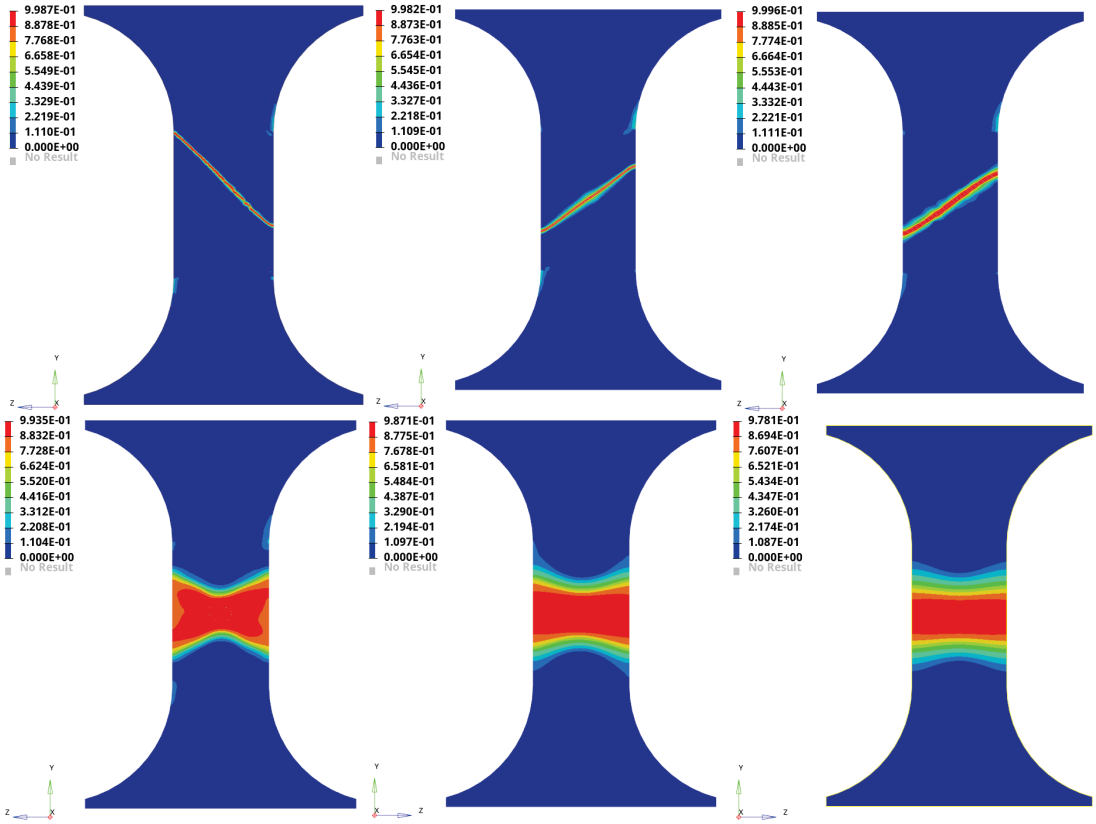

Figure 4.15. Distribution of compression damage with varying l_c values

and have an inclination approximately $53°$. Thence, it is understood that for this specific example, the minimum element size to l_c ratio to achieve physically realistic results should be at equal or smaller than one.

4.7. Conclusions

In this chapter, Puck's criteria is embedded in a damage mechanics framework that resolves mesh related problems.The resulting gradient based formulation is implemented in finite element software Abaqus through User Element. To reduce the computational cost of the search of the failure plane, Extended Golden Section Search Algorithm is used. Through the study Fiber Failure is disregarded and Inter Fiber Failure is considered.

After proving mesh objectivity and suppression of artifical widening, a challenging compression test from literature is used to assess the capacity of the model. As seen from Figure 4.15 and Figure 4.16, as long as appropriate l_c values are used, model prediction are in a very good qualitative agreement with experimental results. As mentioned also in main text, achieving such a consistency between material point failure angle and specimen level damage band orientation has not been reported by a continuum damage mechanics

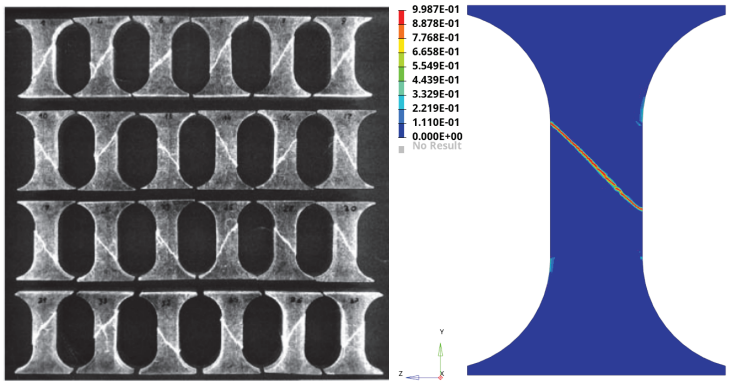

Figure 4.16. Experimental (Knops, 2008) and numerical results are similar

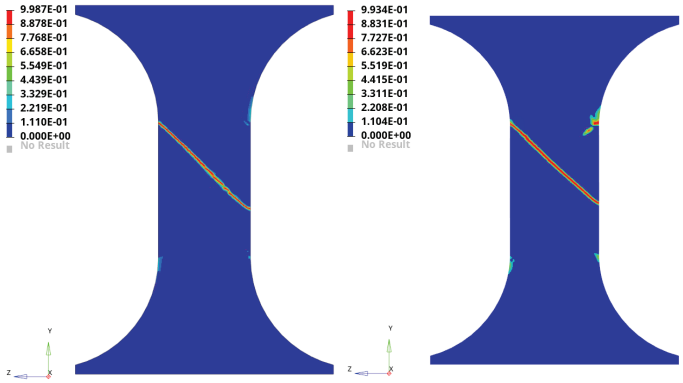

Figure 4.17. Distribution of compression damage for the same $l_c = 0.10$ mm

based approach before.

CHAPTER 5

CONCLUSION AND OUTLOOK

The point of departure for this thesis was to contribute to two major issues in computational modeling of failure in fiber reinforced composites. In a nutshell, the first issue can be summarized as complementing physical testing by computational micro-mechanical modeling and the second one is progressive analysis of failure at macro scale through a combination of Puck's failure criteria and continuum damage mechanics. To address these issues a number of developments and a large number of analysis have been realized.

In Chapter 2, to be employed as material model for the matrix phase, a plasticity model with tension-compression asymmetry is extended with a mesh objective damage mechanics formulation and implemented in Abaqus as a user defined element. The model is calibrated with experimental results and succesfully captures the failure mode without artificial widening. However the model has to improved if it is going to be used to model components made of matrix material (epoxy) only. The formulation is limited to small strains whereas the strain levels under compression tests on epoxy specimens reach to very large values. On the other hand, due to heterogeneous stress state developing within the RVE and failure mostly due to tensile and/or shear stress zones, damage-plasticity model can be used for RVE type micromechanical models.

In Chapter 3, the focus was on computational micromechanical modeling where damage-plasticity model is combined with cohesive contact surfaces used to capture interface failure are embedded in RVE type micro-mechanical models. Sufficiently large number of analysis were conducted to construct discrete failure envelope and compared with continuous failure envelopes associated with Puck's failure criteria. Additionally, a specific type of microstructural imperfection is taken into account and its influence is analyzed in a systematic manner and the main findings are given in Chapter 3. A lower cost alternative could be the use of generalized cell type models which incorporate plasticity and damage (Voyiadjis and Deliktas, 1997). In Chapter 3 the focus was on in plane failure excluding out-of-plane loading and failure scenarious especially under compressive loading that might lead to fiber kinking type failure. Unfortunately, solving such problems within implicit framework turns out to be a very challenging problem

numerically and typically requires robust arc-length type solvers. Due to existence of multiple fibers and heterogeneous nature of RVE response, existing arc-length solvers do not always give convergent results with arbitrary RVE configurations. Development and implementation of more general arclength solvers is a research problem on its own, see for example (Özdemir, 2019). Furthermore, to investigate the response of RVE models under the influence of out-plane compressive loads explicit frameworks (Sun, Meng, et al., 2018; Sun et al., 2019) may also be considered in future studies. Imperfections located at matrix-fiber interfaces are not the only type of micro-structural imperfections remaining from manufacturing processes. Micro-voids within the matrix and combination of different imperfection types can be considered in future studies as well.

In Chapter 4, the focus was shifted towards macroscopic modeling and progressive failure analysis where Puck's criteria and localizing implicit gradient damage formulation are combined under continuum damage mechanics framework.The number of modeling studies focusing on compressive failure is limited since capturing macroscopic failure orientations that are consistent with failure angles emerging at material point, in this specific case θ_{fp} of Puck's model. The proposed formulation is implemented in Abaqus again as a user element and tested with compression tests. It is shown that resulting macroscopic failure surfaces are in agreement with the microscopic failure angle predictions provided that the internal length scale is sufficiently small. Qualitative agreement between the model and experiments is also noteworthy. For the purpose of quantitative comparison with experiments the model has to be extended so that different ply orientations can be taken into account. This is relatively straight forward to realize as compared to fiber failure under compression along the fiber direction which needs some further theoretical elaboration.

There is growing interest in data science and associated techniques not only in computer science but also in almost all engineering disciplines. As far as composite mechanics and failure is concrned, RVE micro-mechanical analysis may used to generate datasets for machine learning applications. Those datasets can also be used to generate Deep Neural Networks that predict the response of uni-directional composites under influence of various loading schemes. Furthermore, datasets are provided by RVE analysis can be exploited by machine learning based approaches to predict mechanical response of composites. There is a vast and growing literature for such applications (J. Chen et al., 2021; Guo et al., 2021; Shah et al., 2022; Wan et al., 2023; Ye et al., 2019). Thence, using RVE to generate datasets for various model configurations and generating machine

learning models to predict to response of uni-directional composites may be considered in future studies.

REFERENCES

Arefi, A., van der Meer, F. P., Forouzan, M. R., & Silani, M. (2018). Formulation of a consistent pressure-dependent damage model with fracture energy as input. *Composite Structures*, *201*(April), 208–216. https://doi.org/10.1016/j.compstruct.2018.06.005

Ashouri Vajari, D., González, C., Llorca, J., & Legarth, B. N. (2014). A numerical study of the influence of microvoids in the transverse mechanical response of unidirectional composites. *Composites Science and Technology*, *97*, 46–54. https://doi.org/10.1016/j.compscitech.2014.04.004

Asp, L. E., Berglund, L. A., & Talreja, R. (1996). A criterion for crack initiation in glassy polymers subected to a composite-like stress state. *Composites Science and Technology*, *56*(11), 1291–1301. https://doi.org/10.1016/S0266-3538(96)00090-5

Azzi, V. D., & Tsai, S. W. (1965). *Anisotropic Strength of Composites Investigation aimed at developing a theory applicable to laminated as well as unidirectional composites, employing simple material properties derived from unidirectional specimens alone* (tech. rep.). https://link.springer.com/content/pdf/10.1007%2FBF02326292.pdf

Barbero, E. J. (n.d.). *Finite Element Analysis of Composite Materials using Abaqus*.

Bathe, K.-J. K. K. (1996). *Finite Element Procedures*. https://doi.org/10.2307/962758

Bažant, Z. P., & Oh, B. H. (1983). Crack band theory for fracture of concrete. *Matériaux et Constructions*, *16*(3), 155–177. https://doi.org/10.1007/BF02486267

Benzeggagh, M., & Kenane, M. (1996). Measurement of mixed-mode delamination fracture toughness of unidirectional glass/epoxy composites with mixed-mode bending apparatus. *Composites Science and Technology*, *56*(–), 439–449. https://doi.org/10.1016/0266-3538(96)00005-X

Bonet, J., & Wood, R. D. (2008). Nonlinear continuum mechanics for finite elements analysis, 318. https://doi.org/10.1007/s13398-014-0173-7.2

Borja, R. I. (2013). *Plasticity: Modeling & Computation*. https://doi.org/10.1007/978-3-642-38547-6 This book is used in CalTech Plasticity lectures ME204.

Canal, L. P., Segurado, J., & LLorca, J. (2009). Failure surface of epoxy-modified fiber-reinforced composites under transverse tension and out-of-plane shear.

International Journal of Solids and Structures, *46*(11-12), 2265–2274. https://doi.org/10.1016/j.ijsolstr.2009.01.014

Catalanotti, G., Camanho, P. P., & Marques, A. T. (2013). Three-dimensional failure criteria for fiber-reinforced laminates. *Composite Structures*, *95*, 63–79. https://doi.org/10.1016/j.compstruct.2012.07.016

Chen, J., Wan, L., Ismail, Y., Ye, J., & Yang, D. (2021). A micromechanics and machine learning coupled approach for failure prediction of unidirectional cfrp composites under triaxial loading: A preliminary study. *COMPOSITE STRUCTURES*, *267*. https://doi.org/10.1016/j.compstruct.2021.113876

Chen, J. F., Morozov, E. V., & Shankar, K. (2014). Simulating progressive failure of composite laminates including in-ply and delamination damage effects. *Composites Part A: Applied Science and Manufacturing*, *61*, 185–200. https://doi.org/10.1016/j.compositesa.2014.02.013

Chevalier, J., Morelle, X. P., Bailly, C., Camanho, P. P., Pardoen, T., & Lari, F. (2016). Micro-mechanics based pressure dependent failure model for highly cross-linked epoxy resins. *Engineering Fracture Mechanics*, *158*(-), 1–12. https://doi.org/10.1016/j.engfracmech.2016.02.039

Coenen, E. W. C., Kouznetsova, V. G., Bosco, E., & Geers, M. G. D. (2012). A multi-scale approach to bridge microscale damage and macroscale failure: A nested computational homogenization-localization framework. *International Journal of Fracture*, *178*(1-2), 157–178. https://doi.org/10.1007/s10704-012-9765-4

Coenen, E. W. C., Kouznetsova, V. G., & Geers, M. G. D. (2012). Multi-scale continuous-discontinuous framework for computational-homogenization-localization. *Journal of the Mechanics and Physics of Solids*, *60*(8), 1486–1507. https://doi.org/10.1016/j.jmps.2012.04.002

Cuntze, R., & Freund, A. (2004). The predictive capability of failure mode concept-based strength criteria for multidirectional laminates. *COMPOSITES SCIENCE AND TECHNOLOGY*, *64*(3-4), 343–377. https://doi.org/10.1016/S0266-3538(03)00218-5

Davila, C. G., Camanho, P. P., Rose, C. A., & Roberto Frias, R. (2005). Failure Criteria for FRP Laminates. https://doi.org/10.1177/0021998305046452

de Souza Neto, E. A., Peri, D., & Owen, D. R. J. (2008). *Computational Methods for Plasticity*. https://doi.org/10.1002/9780470694626

Dean, A., Kumar, P. K. A. V., Reinoso, J., Gerendt, C., Paggi, M., Mahdi, E., & Rolfes, R. (2020). A multi phase-field fracture model for long fiber reinforced composites based on the puck theory of failure. *Composite Structures*, *251*. https://doi.org/10.1016/j.compstruct.2020.112446

Deuschle, H. M., & Kröplin, B. H. (2012). Finite element implementation of puck's failure theory for fibre-reinforced composites under three-dimensional stress. *Journal of Composite Materials*, *46*, 2485–2513. https://doi.org/10.1177/0021998312451480

Deuschle, H. M., & Puck, A. (2013). Application of the Puck failure theory for fibre-reinforced composites under three-dimensional stress: Comparison with experimental results. *Journal of Composite Materials*, *47*(6-7), 827–846. https://doi.org/10.1177/0021998312462158

Engelen, R., Geers, M., & Baaijens, F. (2003). Nonlocal implicit gradient-enhanced elasto-plasticity for the modelling of softening behaviour. *INTERNATIONAL JOURNAL OF PLASTICITY*, *19*(4), 403–433. https://doi.org/10.1016/S0749-6419(01)00042-0

Fiedler, B., Hojo, M., Ochiai, S., Schulte, K., & Ando, M. (2001). Failure behavior of an epoxy matrix under different kinds of static loading. *Composites Science and Technology*, *61*(11), 1615–1624. https://doi.org/10.1016/S0266-3538(01)00057-4

Geers, M. G., Peerlings, R. H., Brekelmans, W. A., & de Borst, R. (2000). Phenomenological nonlocal approaches based on implicit gradient-enhanced damage. *Acta Mechanica*, *144*(1-2), 1–15. https://doi.org/10.1007/BF01181824

Ghorbel, E. (2008). A viscoplastic constitutive model for polymeric materials. *International Journal of Plasticity*, *24*(11), 2032–2058. https://doi.org/10.1016/j.ijplas.2008.01.003

Guo, K., Yang, Z., Yu, C.-H., & Buehler, M. J. (2021). Artificial intelligence and machine learning in design of mechanical materials. *MATERIALS HORIZONS*, *8*(4), 1153–1172. https://doi.org/10.1039/d0mh01451f

Hashin, Z. (1980). Failure Criteria for Unidirectional Fiber Composites. *Journal of Applied Mechanics*, *47*(2), 329. https://doi.org/10.1115/1.3153664

Herraez, M., Mora, D., Naya, F., Lopes, C. S., González, C., & LLorca, J. (2015). Transverse cracking of cross-ply laminates: A computational micromechanics perspective. *Composites Science and Technology*, *110*, 196–204. https://doi.org/https://doi.org/10.1016/j.compscitech.2015.02.008

Hinton, M., Kaddour, A., & Soden, P. (2002). A comparison of the predictive capabilities of current failure theories for composite laminates, judged against experimental evidence. *Composites Science and Technology*, *62*(12), 1725–1797. https://doi.org/https://doi.org/10.1016/S0266-3538(02)00125-2

Hoff, D. (1995). Global solutions of the navier-stokes equations for multidimensional compressible flow with discontinuous initial data. *Journal of Differential Equations*, *120*(1), 215–254. https://doi.org/10.1006/jdeq.1995.1111

Hofman, P., Ke, L., & van der Meer, F. P. (2023). Circular representative volume elements for strainlocalization problems. *International Journal for Numerical Methods in Engineering*, *124*(-–), 784–807. https://doi.org/10.1002/nme.7142

Jiang, H., Ren, Y., Liu, Z., & Zhang, S. (2019). Microscale finite element analysis for predicting effects of air voids on mechanical properties of single fiber bundle in composites. *JOURNAL OF MATERIALS SCIENCE*, *54*(2), 1363–1381. https://doi.org/10.1007/s10853-018-2928-6

Jirasek. (1998). Nonlocal models for damage and fracture: comparison of approaches. *International Journal of Solids and Structures*, *135*(97), 4133–4145.

Jirásek, M., & Grassl, P. (2008). Evaluation of directional mesh bias in concrete fracture simulations using continuum damage models. *Engineering Fracture Mechanics*, *75*(8), 1921–1943. https://doi.org/10.1016/j.engfracmech.2007.11.010

Kaddour, A. S., & Hinton, M. J. (2012). Input data for test cases used in benchmarking triaxial failure theories of composites. *Journal of Composite Materials*, *46*, 2295–2312. https://doi.org/10.1177/0021998312449886

Kaddour, A. S., & Hinton, M. J. (2013). Maturity of 3D failure criteria for fibre-reinforced composites: Comparison between theories and experiments: Part B of WWFE-II. *Journal of Composite Materials*, *47*(6-7), 925–966. https://doi.org/10.1177/0021998313478710

Knops, M. (2008). *Analysis of Failure in Fiber Polymer Laminates*. https://doi.org/10.1007/978-3-540-75765-8

Liu, H., Zeng, D., Li, Y., & Jiang, L. (2016). Development of RVE-embedded solid elements model for predicting effective elastic constants of discontinuous fiber reinforced composites. *Mechanics of Materials*, *93*, 109–123. https://doi.org/10.1016/j.mechmat.2015.10.011

M., J. (1998). Nonlocal models for damage and fracture: comparison of approaches. *International Journal of Solids and Structures*, *135*(97), 4133–4145.

Maimí, P., Camanho, P. P., Mayugo, J. A., & Dávila, C. G. (2007). A continuum damage model for composite laminates: Part II - Computational implementation and validation. *Mechanics of Materials*. https://doi.org/10.1016/j.mechmat.2007.03.006

Melro, A. R., Camanho, P. P., Andrade Pires, F. M., & Pinho, S. T. (2013a). Micromechanical analysis of polymer composites reinforced by unidirectional fibres: Part I-Constitutive modelling. *International Journal of Solids and Structures*, *50*(11-12), 1897–1905. https://doi.org/10.1016/j.ijsolstr.2013.02.009

Melro, A. R., Camanho, P. P., Andrade Pires, F. M., & Pinho, S. T. (2013b). Micromechanical analysis of polymer composites reinforced by unidirectional fibres: Part II-Micromechanical analyses. *International Journal of Solids and Structures*, *50*(11-12), 1906–1915. https://doi.org/10.1016/j.ijsolstr.2013.02.007

Melro, A. R., Camanho, P. P., & Pinho, S. T. (2008). Generation of random distribution of fibres in long-fibre reinforced composites. *Composites Science and Technology*, *68*(9), 2092–2102. https://doi.org/10.1016/j.compscitech.2008.03.013

Naya, F., Herráez, M., Lopes, C., González, C., Van der Veen, S., & Pons, F. (2017). Computational micromechanics of fiber kinking in unidirectional frp under different environmental conditions. *Composites Science and Technology*, *144*, 26–35. https://doi.org/https://doi.org/10.1016/j.compscitech.2017.03.014

Nemat-Nasser, S. (1999). Averaging theorems in finite deformation plasticity. *Mechanics of Materials*, *31*, 493–523. https://doi.org/10.1016/s0167-6636(98)00073-8

Nguyen, V.-D., Lani, F., Pardoen, T., Morelle, X., & Noels, L. (2016). A large strain hyperelastic viscoelastic-viscoplastic-damage constitutive model based on a multi-mechanism non-local damage continuum for amorphous glassy polymers. *International Journal of Solids and Structures*, *96*, 192–216. https://doi.org/https://doi.org/10.1016/j.ijsolstr.2016.06.008

Özdemir, İ. (2019). An alternative implementation of energy/dissipation based arc-length control method. *Theoretical and Applied Fracture Mechanics*, *100*, 208–214. https://doi.org/10.1016/j.tafmec.2019.01.007

Palizvan, M., Sadr, M. H., & Tahaye Abadi, M. (2020). Effect of interface properties on micromechanical damage behavior of fiber reinforced composites. *Materials Today Communications*, *23*, 100856. https://doi.org/https://doi.org/10.1016/j.mtcomm.2019.100856

Park, H., & Cho, M. (2020). A multiscale framework for the elasto-plastic constitutive equations of crosslinked epoxy polymers considering the effects of temperature, strain rate, hydrostatic pressure, and crosslinking density. *Journal of the Mechanics and Physics of Solids*, *142*, 103962. https://doi.org/https://doi.org/10.1016/j.jmps.2020.103962

Park, H., & Cho, M. (2021). Multiscale constitutive model using data–driven yield function. *Composites Part B: Engineering*, *216*, 108831. https://doi.org/https://doi.org/10.1016/j.compositesb.2021.108831

Paul, B. (1960). A modification of the coulomb-mohr theory of fracture. *Journal of Applied Mechanics, Transactions ASME*, *28*(2), 259–268. https://doi.org/10.1115/1.3641665

Peerlings, R. H. J., De Borst, R., Brekelmans, W. A. M., & De Vree, J. H. P. (1996). Gradient enhanced damage for quasi-brittle materials. *International Journal for Numerical Methods in Engineering*, *39*(19), 3391–3403. https://doi.org/10.1002/(SICI)1097-0207(19961015)39:19<3391::AID-NME7>3.0.CO;2-D

Peerlings, R. H., de Borst, R., Brekelmans, W. A., & Geers, M. G. (1998). Gradient-enhanced damage modelling of concrete fracture. *Mechanics of Cohesive-Frictional Materials*, *3*(4), 323–342. https://doi.org/10.1002/(SICI)1099-1484(1998100)3:4<323::AID-CFM51>3.0.CO;2-Z

Peerlings, R. H., Geers, M. G., De Borst, R., & Brekelmans, W. A. (2001). A critical comparison of nonlocal and gradient-enhanced softening continua. *International Journal of Solids and Structures*, *38*(44-45), 7723–7746. https://doi.org/10.1016/S0020-7683(01)00087-7

Peerlings, R. H., Massart, T. J., & Geers, M. G. (2004). A thermodynamically motivated implicit gradient damage framework and its application to brick masonry cracking. *Computer Methods in Applied Mechanics and Engineering*, *193*, 3403–3417. https://doi.org/10.1016/j.cma.2003.10.021

Pinho, S. T., Iannucci, L., & Robinson, P. (2006). Physically based failure models and criteria for laminated fibre-reinforced composites with emphasis on fibre kinking. Part II: FE implementation. *Composites Part A: Applied Science and Manufacturing*, *37*(5), 766–777. https://doi.org/10.1016/j.compositesa.2005.06.008

Poh, L. H., & Sun, G. (2017). Localizing gradient damage model with decreasing interactions. *International Journal for Numerical Methods in Engineering*, *110*(6), 503–522. https://doi.org/10.1002/nme.5364

Poulios, K., & Niordson, C. (2016). Homogenization of long fiber reinforced composites including fiber bending effects. *Journal of the Mechanics and Physics of Solids*, *94*(-–), 433–452. https://doi.org/10.1016/j.jmps.2016.04.010

Puck, A. (1998). Failure Analysis Of Frp Laminates By Means Of Physically Based Phenomenological Models. *Composites Science and Technology*, *58*(7), 1045–1067. https://doi.org/10.1016/S0266-3538(96)00140-6

Puck, A., Kopp, J., & Knops, M. (2002). Guidelines for the determination of the parameters in Puck's action plane strength criterion. *Composites Science and Technology*, *62*(3), 371–378. https://doi.org/10.1016/S0266-3538(01)00202-0

Puck, A., & Schürmann, H. (2002). Failure Analysis of FRP Lamninates by Means of Physically Based Phenomenological Models.pdf. *Composites Science and Technology*, *62*, 1633–1662. https://doi.org/10.1016/S0266-3538(01)00208-1

Reinoso, J., Catalanotti, G., Blázquez, A., Areias, P., Camanho, P. P., & París, F. (2017). A consistent anisotropic damage model for laminated fiber-reinforced composites using the 3D-version of the Puck failure criterion. *International Journal of Solids and Structures*, *126-127*, 37–53. https://doi.org/10.1016/j.ijsolstr.2017.07.023

Romanowicz, M. (2014). Initiation of kink bands from regions of higher misalignment in carbon fiber-reinforced polymers. *Journal of Composite Materials*, *48*(19), 2387–2399. https://doi.org/10.1177/0021998313498106

Sarkar, S., Singh, I. V., Mishra, B. K., Shedbale, A. S., & Poh, L. H. (2019). A comparative study and ABAQUS implementation of conventional and localizing gradient enhanced damage models. *Finite Elements in Analysis and Design*, *160*(September 2018), 1–31. https://doi.org/10.1016/j.finel.2019.04.001

Sarkar, S., Singh, I., & Mishra, B. (2021). A simplified continuous–discontinuous approach to fracture based on decoupled localizing gradient damage method. *Computer Methods in Applied Mechanics and Engineering*, *383*, 113893. https://doi.org/https://doi.org/10.1016/j.cma.2021.113893

Sarkar, S., Singh, I., & Mishra, B. (2022). A simple and efficient implementation of localizing gradient damage method in comsol for fracture simulation. *Engineering Fracture Mechanics*, *269*, 108552. https://doi.org/https://doi.org/10.1016/j.engfracmech.2022.108552

Schirmaier, F. J., Weiland, J., Kärger, L., & Henning, F. (2014). A new efficient and reliable algorithm to determine the fracture angle for Puck's 3D matrix failure criterion for UD composites. *Composites Science and Technology*, *100*, 19–25. https://doi.org/10.1016/j.compscitech.2014.05.033

Shah, V., Zadourian, S., Yang, C., Zhang, Z., & Gu, G. X. (2022). Data-driven approach for the prediction of mechanical properties of carbon fiber reinforced composites. *MATERIALS ADVANCES*, *3*(19), 7319–7327. https://doi.org/10.1039/d2ma00698g

Simo, J. C. (1999). Computational inelasticity. *Computers & Mathematics with Applications*, *37*(3), 134. https://doi.org/10.1016/S0898-1221(99)90413-3

Simulia, D. S. (2014). Abaqus 6.14 / Analysis User's Guide. *ABAQUS 6.14 Analysis User's Guide*, *1*, 862. https://doi.org/10.1017/CBO9781107415324.004

Skovsgaard, S. P., & Jensen, H. M. (2018). Constitutive model for imperfectly bonded fibre-reinforced composites. *Composite Structures*, *192*, 82–92. https://doi.org/https://doi.org/10.1016/j.compstruct.2018.02.053

Soden, P. D., Kaddour, A. S., & Hinton, M. J. (2004). Recommendations for designers and researchers resulting from the world-wide failure exercise. https://doi.org/10.1016/S0266-3538(03)00228-8

Sun, Q., Guo, H., Zhou, G., Meng, Z., Chen, Z., Kang, H., Keten, S., & Su, X. (2018). Experimental and computational analysis of failure mechanisms in unidirectional carbon fiber reinforced polymer laminates under longitudinal compression loading. *Composite Structures*, *203*, 335–348. https://doi.org/https://doi.org/10.1016/j.compstruct.2018.06.028

Sun, Q., Meng, Z., Zhou, G., Lin, S. P., Kang, H., Keten, S., Guo, H., & Su, X. (2018). Multi-scale computational analysis of unidirectional carbon fiber reinforced polymer composites under various loading conditions. *Composite Structures*, *196*(May), 30–43. https://doi.org/10.1016/j.compstruct.2018.05.025

Sun, Q., Zhou, G., Meng, Z., Guo, H., Chen, Z., Liu, H., Kang, H., Keten, S., & Su, X. (2019). Failure criteria of unidirectional carbon fiber reinforced polymer composites informed by a computational micromechanics model. *Composites Science and Technology*, *172*(December 2018), 81–95. https://doi.org/10.1016/j.compscitech.2019.01.012

Systemes, D. (2013). *Abaqus user subroutines reference guide*.

Thomson, D. M., Cui, H., Erice, B., Hoffmann, J., Wiegand, J., & Petrinic, N. (2017). Experimental and numerical study of strain-rate effects on the IFF fracture angle using a new efficient implementation of Puck's criterion. *Composite Structures*, *181*, 325–335. https://doi.org/10.1016/j.compstruct.2017.08.084

Totry, E., González, C., & LLorca, J. (2008). Failure locus of fiber-reinforced composites under transverse compression and out-of-plane shear. *Composites Science and Technology*, *68*(3-4), 829–839. https://doi.org/10.1016/j.compscitech.2007.08.023

Tsai, S. W., & Wu, E. M. (1971). A General Theory of Strength for Anisotropic Materials. *Journal of Composite Materials*, *5*(1), 58–80. https://doi.org/10.1177/002199837100500106

Tschoegl, N. W. (1971). Failure surfaces in principal stress space. *Polymer Science Symposium*, *32*, 239–267. https://doi.org/10.1002/polc.5070320113

Van Der Meer, F. P. (2016). Micromechanical validation of a mesomodel for plasticity in composites. *European Journal of Mechanics, A/Solids*, *60*, 58–69. https://doi.org/10.1016/j.euromechsol.2016.06.008

Vinícius, A. M., Leite, R. M., & Volnei, T. (2018). A computational framework for predicting onset and crack propagation in composite structures via extended finite element method (xfem). *Latin American Journal of Solids and Structures*, *15*. https://doi.org/10.1590/1679-78254301

Vogler, M., Rolfes, R., & Camanho, P. (2013). Modeling the inelastic deformation and fracture of polymer composites – part i: Plasticity model. *Mechanics of Materials*, *59*, 50–64. https://doi.org/https://doi.org/10.1016/j.mechmat.2012.12.002

Voyiadjis, G. Z., & Deliktas, B. (1997). *Damage in mmcs using the gmc: Theoretical formulation*.

Voyiadjis, G. Z., Deliktas, B., & Aifantis, E. C. (2001). *Multiscale analysis of multiple damage mechanisms coupled with inelastic behavior of composite materials*.

Voyiadjis, G. Z., Pekmezi, G., & Deliktas, B. (2010). Nonlocal gradient-dependent modeling of plasticity with anisotropic hardening. *International Journal of Plasticity*, *26*, 1335–1356. https://doi.org/10.1016/j.ijplas.2010.01.015

Wan, L., Ismail, Y., Zhu, C., Zhu, P., Sheng, Y., Liu, J., & Yang, D. (2020). Computational micromechanics-based prediction of the failure of unidirectional composite lamina subjected to transverse and in-plane shear stress states. *Journal*

of Composite Materials, *54*(24), 3637–3654. https://doi.org/10.1177/0021998320918015

Wan, L., Ullah, Z., Yang, D., & Falzon, B. G. (2023). Probability embedded failure prediction of unidirectional composites under biaxial loadings combining machine learning and micromechanical modelling. *COMPOSITE STRUCTURES*, *312*. https://doi.org/10.1016/j.compstruct.2023.116837

Wang, Z. W., Zhao, J. P., & Zhang, X. (2018). Finite element analysis of composite laminates subjected to low-velocity impact based on multiple failure criteria. *Materials Research Express*, *5*. https://doi.org/10.1088/2053-1591/aacca3

Wiegand, J., Petrinic, N., & Elliott, B. (2008). An algorithm for determination of the fracture angle for the three-dimensional Puck matrix failure criterion for UD composites. https://doi.org/10.1016/j.compscitech.2008.05.004

Wongsto, A., & Li, S. (2005). Micromechanical fe analysis of ud fibre-reinforced composites with fibres distributed at random over the transverse cross-section. *Composites Part A: Applied Science and Manufacturing*, *36*(9), 1246–1266. https://doi.org/https://doi.org/10.1016/j.compositesa.2005.01.010

Wosatko, A. (2021). Comparison of evolving gradient damage formulations with different activity functions. *ARCHIVE OF APPLIED MECHANICS*, *91*(2, SI), 597–627. https://doi.org/10.1007/s00419-021-01889-2

Wosatko, A. (2022). Survey of localizing gradient damage in static and dynamic tension of concrete. *Materials*, *15*. https://doi.org/10.3390/ma15051875

Ye, S., Li, B., Li, Q., Zhao, H.-P., & Feng, X.-Q. (2019). Deep neural network method for predicting the mechanical properties of composites. *APPLIED PHYSICS LETTERS*, *115*(16). https://doi.org/10.1063/1.5124529

Yu, Y., Zhang, B., Tang, Z., & Qi, G. (2015). Stress transfer analysis of unidirectional composites with randomly distributed fibers using finite element method. *Composites Part B: Engineering*, *69*, 278–285. https://doi.org/10.1016/j.compositesb.2014.09.035

Yuan, Z., & Fish, J. (2008). Toward realization of computational homogenization in practice. *International Journal for Numerical Methods in Engineering*, *73*(3), 361–380. https://doi.org/10.1002/nme.2074

Zhang, C., Zhao, J., & Rabczuk, T. (2018). The interface strength and delamination of fiber-reinforced composites using a continuum modeling approach. *Composites*

Part B: Engineering, *137*, 225–234.
https://doi.org/https://doi.org/10.1016/j.compositesb.2017.11.007

Zhou, S., Yang, C., Tian, K., Wang, D., Sun, Y., Guo, L., & Zhang, J. (2019). Progressive failure modelling of double-lap of composite bolted joints based on puck's criterion. *Engineering Fracture Mechanics*.
https://doi.org/10.1016/j.engfracmech.2018.11.038

APPENDIX A

User Element Implementation

sect:UEL To implement eight nodded fully integrated linear three-dimensional brick elements (C3D8), firstly, the weak form of the linear moment balance equation is expressed.

A.1. The Weak Form of the Linear Momentum Balance Equation

$$\begin{aligned} \rho\dot{v} &= div\boldsymbol{\sigma} + \rho\boldsymbol{b} \\ div\boldsymbol{\sigma} + \rho\boldsymbol{b} &= 0 \end{aligned} \tag{A.1}$$

The linear momentum equation (Equation (A.1)) is complemented with boundary conditions given in Equation (A.2). To the purpose of the derivation of the weak form, a special test function η, which takes the value of zero at displacement boundary conditions ($on\ \delta B_u,\ \eta = 0$) is introduced. Furthermore, instead of satisfying Equation (A.1) pointwise, equation is satisfied by in an integral sense (Equation (A.3))

$$\begin{aligned} \boldsymbol{u} &= \bar{\boldsymbol{u}}\ on\ \delta B_u \\ \boldsymbol{t} &= \bar{\boldsymbol{t}}\ on\ \delta B_t \end{aligned} \tag{A.2}$$

$$\int_V \left(div(\boldsymbol{\sigma}) + \rho\boldsymbol{b}\right)\eta dV = \mathbf{0} \tag{A.3}$$

If Equation (A.3) is expanded, then Equation (A.4) is obtained.

$$\int_V div(\boldsymbol{\sigma})dV + \int_V \rho\boldsymbol{b}\eta dV = \mathbf{0} \tag{A.4}$$

The term $div(\boldsymbol{\sigma})$ in Equation (A.4) can be written in an alternative form as follows,

$$div(\boldsymbol{\sigma}) = \nabla(\boldsymbol{\sigma}\boldsymbol{\eta}) : \boldsymbol{I} \tag{A.5}$$

$$= \frac{\partial \sigma_{ij}\eta_j}{\partial x_k}\delta_{ik} \tag{A.6}$$

$$= \left(\frac{\partial \sigma_{ij}}{\partial x_k}\eta_j + \sigma_{ij}\frac{\partial \eta_j}{x_k}\right)\delta_{ij} \tag{A.7}$$

$$= \left(\frac{\partial \sigma_{kj}}{\partial x_k}\eta_j + \sigma_{kj}\frac{\partial \eta_j}{x_k}\right) \tag{A.8}$$

$$= \left(\frac{\partial \sigma_{jk}}{\partial x_k}\eta_j + \sigma_{kj}\frac{\partial \eta_j}{x_k}\right) \tag{A.9}$$

Equation (A.9) can be written in close form as follows,

$$div(\boldsymbol{\sigma}\boldsymbol{\eta}) = \boldsymbol{\eta} div(\boldsymbol{\sigma}) + \nabla\boldsymbol{\eta} : \boldsymbol{\sigma} \tag{A.10}$$

Hence, the term $div(\boldsymbol{\sigma})$ can be expressed as follows.

$$div(\boldsymbol{\sigma}\boldsymbol{\eta}) = div(\boldsymbol{\sigma}\boldsymbol{\eta}) - \nabla\boldsymbol{\eta} : \boldsymbol{\sigma} \tag{A.11}$$

Once Equation (A.11) is put into Equation (A.4), the following equation is obtained.

$$\int_V div(\boldsymbol{\sigma}\boldsymbol{\eta})\, dV - \int_V \nabla\boldsymbol{\eta} : \boldsymbol{\sigma} dV + \int_V \rho \boldsymbol{b}\eta dV = \boldsymbol{0} \tag{A.12}$$

The term, $\int_V div(\boldsymbol{\sigma}\boldsymbol{\eta})\, dV$ in Equation (A.12) can be transformed into area integral by using divergence theorem as follows,

$$\int_V div(\boldsymbol{\sigma}\boldsymbol{\eta})\, dV = \int_{\delta_B} (\boldsymbol{\sigma}\boldsymbol{\eta})\, \boldsymbol{n} dA$$

in index notation,

$$\int_{\delta_B} (\boldsymbol{\sigma}\boldsymbol{\eta})\, \boldsymbol{n} dA = \int \sigma_{ij}\eta_j n_i dA \tag{A.13}$$

$$= \int \sigma_{ji} n_i \eta_j dA$$

Finally, in matrix form,

$$= \int_{\delta_B} \boldsymbol{t}\boldsymbol{\eta} dA$$

One of the first assumptions of $\boldsymbol{\eta}$ is that, η takes value of zero on displacement boundary

conditions. Hence the term Equation $\int_{\delta_B} \boldsymbol{t}\boldsymbol{\eta} dA$ in (A.13)is changed and takes the following form.

$$\int_{\delta_B} \boldsymbol{t}\boldsymbol{\eta} dA = \int_{\delta_{B_t}} \boldsymbol{t}\boldsymbol{\eta} dA \tag{A.14}$$

Replacing the term of $\int_V div\,(\boldsymbol{\sigma}\boldsymbol{\eta})\, dV$ in Equation (A.12) with the Equation (A.14), yields the weak form of the Equation (A.1).

$$\int_V \boldsymbol{\sigma} : \nabla\boldsymbol{\eta} dV = \int_V \rho \boldsymbol{b}\boldsymbol{\eta} dV - \int_{\delta_{B_t}} \boldsymbol{t}\boldsymbol{\eta} dA \tag{A.15}$$

Since there is no special assumption is made for the derivation of Equation (A.15), it applies to general problems such as in-elastic materials Bathe, 1996, non-associated loading implicit gradient formulations, etc.

To complete the derivation, the term $\nabla\eta$ must be investigated. To do so, the concept of variation must be employed. Variation of the derivative of a quantity in the direction of η. The Greek letter "δ" is used for the variation. The variation of $\nabla\boldsymbol{u}$ in the direction of special function η is defined as follows,

$$\begin{aligned} D\left(\nabla\boldsymbol{u}\right)[\eta] &= \frac{d}{d\epsilon}\left(\nabla\left(\boldsymbol{u} + \epsilon\boldsymbol{\eta}\right)\right)|_{\epsilon=0} \\ \delta\nabla\boldsymbol{u} &= \nabla\boldsymbol{\eta} \end{aligned} \tag{A.16}$$

With the aid of Equation (A.16), the term $\boldsymbol{\sigma} : \nabla\eta$ in Equation (A.15) takes the following form,

$$\boldsymbol{\sigma} : \nabla\eta = \boldsymbol{\sigma} : \delta\nabla\boldsymbol{u} \tag{A.17}$$

It is known that, $\boldsymbol{\sigma}$ is symmetric. The $\delta\nabla\boldsymbol{u}$ in Equation (A.17) can be splitted into symmetric and skew-symmetric parts as follows,

$$\delta\nabla\boldsymbol{u} = \frac{1}{2}\delta\left(\nabla\boldsymbol{u} + (\nabla\boldsymbol{u})^T\right) + \frac{1}{2}\delta\left(\nabla\boldsymbol{u} - (\nabla\boldsymbol{u})^T\right) \tag{A.18}$$

It is also known that the multiplication of symmetric and skew-symmetric parts is zero.

Therefore, the result of Equation (A.17) can be expressed as,

$$\begin{aligned} \boldsymbol{\sigma} : \delta\nabla\boldsymbol{u} &= \boldsymbol{\sigma} : \frac{1}{2}\delta\left(\nabla\boldsymbol{u} + (\nabla\boldsymbol{u})^T\right) \\ &= \boldsymbol{\sigma} : \delta\boldsymbol{\varepsilon} \end{aligned} \tag{A.19}$$

Where the term, $\delta\boldsymbol{\varepsilon}$ is the virtual strain. Finally, the weak form of the Equation (A.1) takes the following form

$$\int_V \boldsymbol{\sigma} : \delta\boldsymbol{\varepsilon} = \int_V \rho\boldsymbol{b}\boldsymbol{\eta}dV - \int_{\delta_{B_t}} \boldsymbol{t}\boldsymbol{\eta}dA \tag{A.20}$$

Equation (A.20) is known as Principle of Virtual Work Bathe, 1996. Furthermore, the left hand side of Equation (A.20) is the virtual work done by internal forces and the right hand side of Equation (A.20) is the virtual work done by external forces.

APPENDIX B

Derivation of the Weak Forms of Gradient Enhanced Models

B.1. Conventional Implicit Gradient Damage Model

With introducing η (a special function), the weak form of the Conventional implicit gradient damage model can be expressed in integral sense as follows,

$$\int_V \left(\bar{\varepsilon_p}^{eq} - l_c^2 \nabla^2 \bar{\varepsilon_p}^{eq} - \varepsilon_p^{eq}\right) \eta dV$$
$$\int_V \left(\bar{\varepsilon_p}^{eq} \eta dV\right) - \int_V \left(l_c^2 \nabla^2 \bar{\varepsilon}_p^{eq} \eta dV\right) - \int_V \left(\varepsilon_p^{eq} \eta dV\right) \tag{B.1}$$

The term $\nabla^2 \bar{\varepsilon}_p^{eq} \eta$ in Equation (B.1) can be expressed in an alternative way as follows,

$$\nabla . \left(\nabla \bar{\varepsilon}_p^{eq} \boldsymbol{\eta}\right) = \nabla^2 \bar{\varepsilon}_p^{eq} \boldsymbol{\eta} + \nabla \bar{\varepsilon}_p^{eq} \nabla \boldsymbol{\eta}$$
$$\nabla^2 \bar{\varepsilon}_p^{eq} \boldsymbol{\eta} = \nabla \cdot \left(\nabla \bar{\varepsilon}_p^{eq} \boldsymbol{\eta}\right) - \nabla \bar{\varepsilon}_p^{eq} \nabla \boldsymbol{\eta} \tag{B.2}$$

With the aid of Equation (B.2), Equation (B.1) can be expressed as follows,

$$\int_V \bar{\varepsilon}_p^{eq} \eta dV - l_c^2 \int_V \nabla . \left(\nabla \bar{\varepsilon}_p^{eq} \eta dV\right) + l_c^2 \int_V \nabla \bar{\varepsilon}_p^{eq} \cdot \nabla \eta dV - \int_V \varepsilon_p^{eq} \eta dV = 0 \tag{B.3}$$

Using the Divergence Theorem yields,

$$\int_V \bar{\varepsilon}_p^{eq} \eta dV - l_c^2 \int_{\delta B} (\nabla \bar{\varepsilon}_p^{eq} \eta) \cdot \boldsymbol{n} dA + l_c^2 \int_V \nabla \bar{\varepsilon}_p^{eq} \cdot \nabla \eta dV - \int_V \varepsilon_p^{eq} \eta dV = 0 \tag{B.4}$$

Using the boundary condition of $\nabla \bar{\varepsilon}_p^{eq} \boldsymbol{n} = 0$ is given, Equation (B.4) takes the following form,

$$\int_V \bar{\varepsilon}_p^{eq} \eta dV + l_c^2 \int_V \nabla \bar{\varepsilon}_p^{eq} \cdot \nabla \eta dV - \int_V \varepsilon_p^{eq} \eta dV = 0 \tag{B.5}$$

Finally Equation (B.5) is the weak form of the Equation (B.1).

B.2. Localizing Implicit Gradient Damage Model

To obtained the weak form, the following partial differential equation (Eq. B.6) must be solved with the boundary conditions given in Eq. B.7.

$$\bar{\varepsilon}_{eq}^{p,+,-} - \nabla \cdot \left(g l_c^2 \nabla \bar{\varepsilon}_{eq}^{p,+,-} \right) - \varepsilon_{eq}^{p,+,-} = 0 \tag{B.6}$$

$$\nabla \bar{\varepsilon}_{eq}^{p,+,-} \cdot \boldsymbol{n} = 0 \tag{B.7}$$

With introducing η (a special function), the weak form of the Conventional implicit gradient damage (Eq. B.6) model can be expressed in integral sense as follows,

$$\int_V \bar{\varepsilon}_{eq}^{p,+,-} \eta dV - g l_c^2 \int_V \nabla^2 \left(\bar{\varepsilon}_{eq}^{p,+,-} \right) \eta dV - \int_V \varepsilon_{eq}^{p,+,-} \eta dV = 0 \tag{B.8}$$

Where, $\nabla^2 \left(\bar{\varepsilon}_{eq}^{p,+,-} \right) \eta$ can be expressed as,

$$\nabla^2 \left(\bar{\varepsilon}_{eq}^{p,+,-} \right) \eta = \nabla . \left(\nabla \bar{\varepsilon}_{eq}^{p,+,-} \right) - \nabla \bar{\varepsilon}_{eq}^{p,+,-} \nabla \eta \tag{B.9}$$

Once Eq. B.9 is implemented to Eq. B.8 the following is obtained.

$$\int_V \bar{\varepsilon}_{eq}^{p,+,-} \eta dV - g l_c^2 \int_B \left(\nabla \bar{\varepsilon}_{eq}^{p,+,-} \right) \boldsymbol{n} dB + g l_c^2 \int_V \nabla \bar{\varepsilon}_{eq}^{p,+,-} \nabla \eta dV - \int_V \varepsilon_{eq}^{p,+,-} \eta dV = 0 \tag{B.10}$$

Since the term $\left(\nabla \bar{\varepsilon}_{eq}^{p,+,-} \right) \boldsymbol{n}$ in Eq. B.10 is zero, the weak form of the Localizing implicit gradient damage model takes the following form,

$$\int_V \bar{\varepsilon}_p^{eq} \eta dV + g l_c^2 \int_V \nabla \bar{\varepsilon}_{eq}^{p,+,-} \nabla \eta dV - \int_V \varepsilon_{eq}^{p,+,-} \eta dV = 0 \tag{B.11}$$

Eq. B.11 is the weak form of Eq. B.6

B.3. Localizing Implicit Gradient Damage Model for Puck's Criteria

To obtained the weak form, the following partial differential equation (Eq. B.12) must be solved with the boundary conditions given in Eq. B.13.

$$\bar{f}^{+,-}_{E,IFF} - \nabla \cdot \left(g l_c^2 \nabla \bar{f}^{+,-}_{E,IFF} \right) - f^{+,-}_{E,IFF} = 0 \tag{B.12}$$

$$\nabla \bar{f}^{+,-}_{E,IFF} \cdot \boldsymbol{n} = 0 \tag{B.13}$$

With introducing η (a special function), the weak form of the Conventional implicit gradient damage (Eq. B.12) model can be expressed in integral sense as follows,

$$\int_V \bar{f}^{+,-}_{E,IFF} \eta dV - g l_c^2 \int_V \nabla^2 \left(\bar{f}^{+,-}_{E,IFF} \right) \eta dV - \int_V f^{+,-}_{E,IFF} \eta dV = 0 \tag{B.14}$$

Where, $\nabla^2 \left(\bar{f}^{+,-}_{E,IFF} \right) \eta$ can be expressed as,

$$\nabla^2 \left(\bar{f}^{+,-}_{E,IFF} \right) \eta = \nabla \cdot \left(\nabla \bar{f}^{+,-}_{E,IFF} \right) - \nabla \bar{f}^{+,-}_{E,IFF} \nabla \eta \tag{B.15}$$

Once Eq. B.15 is implemented to Eq. B.14 the following is obtained.

$$\int_V \bar{f}^{+,-}_{E,IFF} \eta dV - g l_c^2 \int_B \left(\nabla \bar{f}^{+,-}_{E,IFF} \right) \boldsymbol{n} dB + g l_c^2 \int_V \nabla \bar{f}^{+,-}_{E,IFF} \nabla \eta dV - \int_V f^{+,-}_{E,IFF} \eta dV = 0 \tag{B.16}$$

Since the term $\left(\nabla \bar{f}^{+,-}_{E,IFF} \right) \boldsymbol{n}$ in Eq. B.16 is zero, the weak form of the Localizing implicit gradient damage model for Puck's failure criteria takes the following form,

$$\int_V \bar{f}^{+,-}_{E,IFF} \eta dV + g l_c^2 \int_V \nabla \bar{f}^{+,-}_{E,IFF} \nabla \eta dV - \int_V f^{+,-}_{E,IFF} \eta dV = 0 \tag{B.17}$$

Eq. B.17 is the weak form of Eq. B.12

APPENDIX C

Linearization of the Weak Form of Localizing Implicit Gradient Damage Model

$$\int \left(\bar{N}\hat{\varepsilon}_{pl}^{+,-}\right)\left(\bar{N}\hat{\eta}\right) dV + gl_c^2 \int \left(\bar{B}\hat{\varepsilon}_{pl}^{+,-}\right)\left(\bar{B}\right) dV - \int \bar{N}^T f\left(\boldsymbol{\sigma}\right) \varepsilon_{pl}^{+,-} = 0 \quad \text{(C.1)}$$

$$\hat{\eta}^T \left[\int \left(\bar{N}^T\right)\left(\bar{N}\hat{\varepsilon}_{pl}^{+,-}\right) dV + gl_c^2 \int \left(\bar{B}^T\right)\left(\bar{B}\hat{\varepsilon}_{pl}^{+,-}\right) dV - \int \bar{N}^T f\left(\boldsymbol{\sigma}\right) \varepsilon_{pl}^{+,-}\right] = 0 \quad \text{(C.2)}$$

The terms in [] must be zero. Then using Gauss quadrature internal force in typical integration point can be described as,

$$w_{igp}\bar{N}^T\left(\bar{N}\hat{\varepsilon}_{pl}^{+,-}\right) detJ + gl_c^2 w_{igp}\bar{B}^T\left(\bar{B}\hat{\varepsilon}_{pl}^{+,-}\right) detJ - w_{igp}\bar{N}^T f\left(\boldsymbol{\sigma}\right)\varepsilon_{pl}^{+,-} detJ = 0 \quad \text{(C.3)}$$

In a matrix form above equation can be described as follows,

$$\boldsymbol{f_I^{+,-}} + \boldsymbol{f_{II}^{+,-}} - \boldsymbol{f_D^{+,-}} = 0 \quad \text{(C.4)}$$

Where,

$$\boldsymbol{f_I^{+,-}} = w_{igp}\bar{N}^T\left(\bar{N}\hat{\varepsilon}_{pl}^{+,-}\right) det \quad \text{(C.5)}$$

$$\boldsymbol{f_{II}^{+,-}} = gl_c^2 w_{igp}\bar{B}^T\left(\bar{B}\hat{\varepsilon}_{pl}^{+,-}\right) detJ \quad \text{(C.6)}$$

$$\boldsymbol{f_D^{+,-}} = w_{igp}\bar{N}^T f\left(\boldsymbol{\sigma}\right)\varepsilon_{pl}^{+,-} detJ \quad \text{(C.7)}$$

Of course, the internal force columns regarding $\boldsymbol{\sigma}$ is defined as,

$$\boldsymbol{f} = \int B^T \sigma dV \quad \text{(C.8)}$$

Which can be discretized and computed numerically as follows,

$$\boldsymbol{f} = w_{igp}B^T \sigma detJ \quad \text{(C.9)}$$

To achieve the quadratic convergence rate, Abaqus uses Newton Raphson solution algorithm. Therefore tangent terms must be calculated. To do so both internal force columns must be linearized. Internal force columns regarding stress and non-local solutions are denoted as r^d and $r^{e,\,+,-}$, respectively.

$$r^d = \boldsymbol{f} \tag{C.10}$$

$$r^{e+} = \boldsymbol{f_I^+} + \boldsymbol{f_{II}^+} - \boldsymbol{f_D^+} \tag{C.11}$$

$$r^{e-} = \boldsymbol{f_I^-} + \boldsymbol{f_{II}^-} - \boldsymbol{f_D^-} \tag{C.12}$$

Which can be described in the matrix form as follows,

$$\begin{bmatrix} \dfrac{\partial r^d}{\partial \bar{u}} & \dfrac{\partial r^d}{\partial \bar{\varepsilon}^+} & \dfrac{\partial r^d}{\partial \bar{\varepsilon}^-} \\ \dfrac{\partial r^{e+}}{\partial \bar{u}} & \dfrac{\partial r^{e++}}{\partial \bar{\varepsilon}} & \dfrac{\partial r^{e+-}}{\partial \bar{\varepsilon}} \\ \dfrac{\partial r^{e-}}{\partial \bar{u}} & \dfrac{\partial r^{e-}}{\partial \bar{\varepsilon}^+} & \dfrac{\partial r^{e-}}{\partial \bar{\varepsilon}^-} \end{bmatrix} \begin{bmatrix} d\hat{u} \\ d\hat{\varepsilon}^+ \\ d\hat{\varepsilon}^- \end{bmatrix} = \begin{bmatrix} dr^d \\ dr^{e+} \\ dr^{e-} \end{bmatrix} \tag{C.13}$$

Where $\dfrac{\partial r^d}{\partial \bar{u}}$, $\dfrac{\partial r^d}{\partial \bar{\varepsilon}^+}$, $\dfrac{\partial r^d}{\partial \bar{\varepsilon}^-}$, $\dfrac{\partial r^{e+}}{\partial \bar{u}}$, $\dfrac{\partial r^{e+}}{\partial \bar{\varepsilon}^+}$, $\dfrac{\partial r^{e+}}{\partial \bar{\varepsilon}^-}$, $\dfrac{\partial r^{e-}}{\partial \bar{u}}$, $\dfrac{\partial r^{e-}}{\partial \bar{\varepsilon}^+}$ and $\dfrac{\partial r^{e-}}{\partial \bar{\varepsilon}^-}$ are denoted as K_{uu}, $K_{u\varepsilon^+}$, $K_{u\varepsilon^-}$, $K_{\varepsilon^+,u}$, $K_{\varepsilon^+,\varepsilon^+}$, $K_{\varepsilon^+,\varepsilon^-}$, $K_{\varepsilon^-,u}$, $K_{\varepsilon^-,\varepsilon^+}$ and $K_{\varepsilon^-,\varepsilon^-}$ respectively. By linearizing r^d, r^{e+} and r^{e-}, those K terms can be computed. First linearization of stress residual can be evaluated as follows,

$$dr^d = \frac{\partial r^d}{\partial \hat{u}} d\hat{u} + \frac{\partial r^d}{\partial \hat{\varepsilon}^+} d\hat{\varepsilon}^+ + \frac{\partial r^d}{\partial \hat{\varepsilon}^-} d\hat{\varepsilon}^- \tag{C.14}$$

$$= \frac{\partial w_{igp} B^T \sigma detJ}{\partial \hat{u}} d\hat{u} + \frac{\partial w_{igp} B^T \sigma detJ}{\partial \hat{\varepsilon}^+} d\hat{\varepsilon}^+ + \frac{\partial w_{igp} B^T \sigma detJ}{\partial \hat{\varepsilon}^-} d\hat{\varepsilon}^- \tag{C.15}$$

$$= K_{uu} d\hat{u} + K_{u\varepsilon^+} d\hat{\varepsilon}^+ + K_{u\varepsilon^-} d\hat{\varepsilon}^- \tag{C.16}$$

Now, K_{uu}, $K_{u\varepsilon^+}$ and $K_{u\varepsilon^-}$ terms can be computed as follows

$$K_{uu} = w_{igp} B^T \frac{\partial \sigma}{\partial \hat{\varepsilon}} B detJ \tag{C.17}$$

$$K_{u\varepsilon^+} = w_{igp} B^T \frac{\partial \sigma}{\partial \bar{\varepsilon}^+} \bar{B} detJ \tag{C.18}$$

$$K_{u\varepsilon^-} = w_{igp} B^T \frac{\partial \sigma}{\partial \bar{\varepsilon}^-} \bar{B} detJ \tag{C.19}$$

Where $(\bar{})$ and $(\hat{})$ terms denote non-local element functions and nodal quantities, respec-

tively. Linearization of non-local residual can be evaluated as follows,

$$dr^{e+} = \frac{\partial\left(f_I^+ + f_{II}^+ + f_D^+\right)}{\partial \hat{u}} d\hat{u} + \frac{\partial\left(f_I^+ + f_{II}^+ + f_D\right)}{\partial \hat{\varepsilon}^+} d\hat{\varepsilon}^+ + \frac{\partial\left(f_I^+ + f_{II}^+ + f_D\right)}{\partial \hat{\varepsilon}^-} d\hat{\varepsilon}^- \tag{C.20}$$

$$= K_{\varepsilon^+ u} d\hat{u} + K_{\varepsilon^+\varepsilon^+} d\hat{\varepsilon}^+ + K_{\varepsilon^+\varepsilon^-} d\hat{\varepsilon}^- \tag{C.21}$$

Where, $K_{\varepsilon^+ u}$ and $K_{\varepsilon^+\varepsilon^+}$ and $K_{\varepsilon^+\varepsilon^-}$ can be computed as follows,

$$K_{\varepsilon^+ u} = w_{igp} \bar{N} \frac{\partial \varepsilon_p^{eq}}{\partial \varepsilon^+} B det J \tag{C.22}$$

$$K_{\varepsilon^+\varepsilon^+} = \frac{\partial f_I^+}{\partial \hat{\varepsilon^+}} + \frac{\partial f_{II}^+}{\partial \hat{\varepsilon^+}} - \frac{\partial f_D^+}{\partial \hat{\varepsilon^+}} \tag{C.23}$$

$$K_{\varepsilon^+\varepsilon^-} = \frac{\partial f_I^+}{\partial \hat{\varepsilon^-}} + \frac{\partial f_{II}^+}{\partial \hat{\varepsilon^-}} - \frac{\partial f_D^+}{\partial \hat{\varepsilon^-}} \tag{C.24}$$

Where,

$$\frac{\partial f_I^+}{\partial \hat{\varepsilon}} = w_{igp} \bar{N} N det J \tag{C.25}$$

$$\frac{\partial f_{II}^+}{\partial \hat{\varepsilon}} = w_{igp} \frac{\partial g}{\partial \hat{\varepsilon}} l_c^2 \bar{B}^T \left(\bar{B}\hat{\varepsilon}\right) det J + g l_c^2 w_{igp} \bar{B}^T \bar{B} det J \tag{C.26}$$

$$\frac{\partial f_D^+}{\partial \hat{\varepsilon}} = w_{igp} \bar{N}^T \frac{\partial \varepsilon_p^{eq}}{\partial \bar{\varepsilon}} \bar{N} det J \tag{C.27}$$

$$\frac{\partial g}{\partial \hat{\varepsilon}} = \frac{\partial g}{\partial D} \frac{\partial D}{\partial \bar{\kappa}} \frac{\partial \bar{\kappa}}{\bar{\varepsilon}} \bar{N} \tag{C.28}$$

Similarly,

$$dr^{e-} = \frac{\partial\left(f_I^- + f_{II}^- + f_D^-\right)}{\partial \hat{u}} d\hat{u} + \frac{\partial\left(f_I^- + f_{II}^- + f_D^-\right)}{\partial \hat{\varepsilon}^+} d\hat{\varepsilon}^+ + \frac{\partial\left(f_I^- + f_{II}^- + f_D^-\right)}{\partial \hat{\varepsilon}^-} d\hat{\varepsilon}^- \tag{C.29}$$

$$= K_{\varepsilon^- u} d\hat{u} + K_{\varepsilon^-\varepsilon^+} d\hat{\varepsilon^+} + K_{\varepsilon^-\varepsilon^-} d\hat{\varepsilon^-} \tag{C.30}$$

Where, $K_{\varepsilon^- u}$ and $K_{\varepsilon^-\varepsilon^+}$ and $K_{\varepsilon^-\varepsilon^-}$ can be computed as follows,

$$K_{\varepsilon^- u} = w_{igp} \bar{N} \frac{\partial \varepsilon_{eq}^{p,\,-}}{\partial \varepsilon^+} B det J \tag{C.31}$$

$$K_{\varepsilon^-\varepsilon^+} = \frac{\partial f_I^-}{\partial \hat{\varepsilon^+}} + \frac{\partial f_{II}^-}{\partial \hat{\varepsilon^+}} - \frac{\partial f_D^-}{\partial \hat{\varepsilon^+}} \tag{C.32}$$

$$K_{\varepsilon^-\varepsilon^-} = \frac{\partial f_I^-}{\partial \hat{\varepsilon^-}} + \frac{\partial f_{II}^-}{\partial \hat{\varepsilon^-}} - \frac{\partial f_D^-}{\partial \hat{\varepsilon^-}} \tag{C.33}$$

APPENDIX D

Linearization of the Weak Form of Localizing Implicit Gradient Damage Model For Puck's Failure Criteria

$$\int \left(\bar{N}\hat{f}^{+,-}_{E,IFF}\right)\left(\bar{N}\hat{\eta}\right)dV + gl_c^2\int \left(\bar{B}\hat{f}^{+,-}_{E,IFF}\right)\left(\bar{B}\right)dV - \int \bar{N}^T f^{+,-}_{E,IFF} = 0 \quad \text{(D.1)}$$

$$\hat{\eta}^T\left[\int \left(\bar{N}^T\right)\left(\bar{N}\hat{f}^{+,-}_{E,IFF}\right)dV + gl_c^2\int \left(\bar{B}^T\right)\left(\bar{B}\hat{f}^{+,-}_{E,IFF}\right)dV - \int \bar{N}^T f^{+,-}_{E,IFF}\right] = 0 \quad \text{(D.2)}$$

The terms in [] must be zero. Then using Gauss quadrature internal force in typical integration point can be described as,

$$w_{igp}\bar{N}^T\left(\bar{N}\hat{f}^{+,-}_{E,IFF}\right)detJ + gl_c^2 w_{igp}\bar{B}^T\left(\bar{B}\hat{f}^{+,-}_{E,IFF}\right)detJ - w_{igp}\bar{N}^T f^{+,-}_{E,IFF}detJ = 0 \quad \text{(D.3)}$$

In a matrix form above equation can be described as follows,

$$\boldsymbol{f_I^{+,-}} + \boldsymbol{f_{II}^{+,-}} - \boldsymbol{f_D^{+,-}} = 0 \quad \text{(D.4)}$$

Where,

$$\boldsymbol{f_I^{+,-}} = w_{igp}\bar{N}^T\left(\bar{N}\hat{f}^{+,-}_{E,IFF}\right)det \quad \text{(D.5)}$$

$$\boldsymbol{f_{II}^{+,-}} = gl_c^2 w_{igp}\bar{B}^T\left(\bar{B}\hat{f}^{+,-}_{E,IFF}\right)detJ \quad \text{(D.6)}$$

$$\boldsymbol{f_D^{+,-}} = w_{igp}\bar{N}^T f^{+,-}_{E,IFF}detJ \quad \text{(D.7)}$$

Of course, the internal force columns regarding $\boldsymbol{\sigma}$ is defined as,

$$\boldsymbol{f} = \int B^T\sigma dV \quad \text{(D.8)}$$

Which can be discretized and computed numerically as follows,

$$\boldsymbol{f} = w_{igp}B^T\sigma detJ \quad \text{(D.9)}$$

To achieve the quadratic convergence rate, Abaqus uses Newton Raphson solution algorithm. Therefore tangent terms must be calculated. To do so both internal force columns must be linearized. Internal force columns regarding stress and non-local solutions are denoted as r^d and $r^{e,\,+,-}$, respectively.

$$r^d = \boldsymbol{f} \tag{D.10}$$

$$r^{e+} = \boldsymbol{f_I^+} + \boldsymbol{f_{II}^+} - \boldsymbol{f_D^+} \tag{D.11}$$

$$r^{e-} = \boldsymbol{f_I^-} + \boldsymbol{f_{II}^-} - \boldsymbol{f_D^-} \tag{D.12}$$

Which can be described in the matrix form as follows,

$$\begin{bmatrix} \dfrac{\partial r^d}{\partial \bar{u}} & \dfrac{\partial r^d}{\partial \bar{f}^+_{E,IFF}} & \dfrac{\partial r^d}{\partial \bar{f}^-_{E,IFF}} \\ \dfrac{\partial r^{e+}}{\partial \bar{u}} & \dfrac{\partial r^{e+}}{\partial \bar{f}^+_{E,IFF}} & \dfrac{\partial r^{e+}}{\partial \bar{f}^-_{E,IFF}} \\ \dfrac{\partial r^{e-}}{\partial \bar{u}} & \dfrac{\partial r^{e-}}{\partial \bar{f}^+_{E,IFF}} & \dfrac{\partial r^{e-}}{\partial \bar{f}^-_{E,IFF}} \end{bmatrix} \begin{bmatrix} d\hat{u} \\ d\hat{f}^+_{E,IFF} \\ d\hat{f}^-_{E,IFF} \end{bmatrix} = \begin{bmatrix} dr^d \\ dr^{e+} \\ dr^{e-} \end{bmatrix} \tag{D.13}$$

Where $\dfrac{\partial r^d}{\partial \bar{u}}$, $\dfrac{\partial r^d}{\partial \bar{f}^+_{E,IFF}}$, $\dfrac{\partial r^d}{\partial \bar{f}^-_{E,IFF}}$, $\dfrac{\partial r^{e+}}{\partial \bar{u}}$, $\dfrac{\partial r^{e+}}{\partial \bar{f}^+_{E,IFF}}$, $\dfrac{\partial r^{e+}}{\partial \bar{f}^-_{E,IFF}}$, $\dfrac{\partial r^{e-}}{\partial \bar{u}}$, $\dfrac{\partial r^{e-}}{\partial \bar{f}^+_{E,IFF}}$ and $\dfrac{\partial r^{e-}}{\partial \bar{f}^-_{E,IFF}}$ are denoted as K_{uu}, K_{uf^+}, K_{uf^-}, K_{f^+u}, $K_{f^+f^+}$, $K_{f^+f^-}$, K_{f^-u}, $K_{f^-f^+}$ and $K_{f^-f^-}$ respectively. By linearizing r^d, r^{e+} and r^{e-}, those K terms can be computed. First linearization of stress residual can be evaluated as follows,

$$dr^d = \frac{\partial r^d}{\partial \hat{u}} d\hat{u} + \frac{\partial r^d}{\partial \hat{f}^+_{E,IFF}} d\hat{f}_{E,IFF} + \frac{\partial r^d}{\partial \hat{f}^-_{E,IFF}} d\hat{f}^-_{E,IFF} \tag{D.14}$$

$$= \frac{\partial w_{igp} B^T \sigma detJ}{\partial \hat{u}} d\hat{u} + \frac{\partial w_{igp} B^T \sigma detJ}{\partial \hat{f}^+_{E,IFF}} d\hat{f}^+_{E,IFF} + \frac{\partial w_{igp} B^T \sigma detJ}{\partial \hat{f}^-_{E,IFF}} d\hat{f}^-_{E,IFF} \tag{D.15}$$

$$= K_{uu} d\hat{u} + K_{uf^+} d\hat{f}^+_{E,IFF} + K_{uf^-} d\hat{f}^-_{E,IFF} \tag{D.16}$$

Now, K_{uu}, K_{uf^+} and K_{uf^-} terms can be computed as follows

$$K_{uu} = w_{igp} B^T \frac{\partial \sigma}{\partial \hat{u}} B detJ \tag{D.17}$$

$$K_{uf^+} = w_{igp} B^T \frac{\partial \sigma}{\partial \bar{f}^+_{E,IFF}} \bar{B} detJ \tag{D.18}$$

$$K_{uf^-} = w_{igp} B^T \frac{\partial \sigma}{\partial \bar{f}^-_{E,IFF}} \bar{B} detJ \tag{D.19}$$

Where ($^-$) and ($\hat{}$) terms denote non-local element functions and nodal quantities, respectively. Linearization of non-local residual can be evaluated as follows,

$$dr^{e+} = \frac{\partial \left(f_I^+ + f_{II}^+ + f_D^+\right)}{\partial \hat{u}} \times d\hat{u} + \frac{\partial \left(f_I^+ + f_{II}^+ + f_D\right)}{\partial \hat{f}_{E,IFF}^+} \times d\hat{f}_{E,IFF} + + \frac{\partial \left(f_I^+ + f_{II}^+ + f_D\right)}{\partial \hat{f}_{E,IFF}^-} \times d\hat{f}_{E,IFF}^- \tag{D.20}$$

$$= K_{f^+u} \times d\hat{u} + K_{f^+f^+} \times d\hat{f}_{E,IFF}^+ + K_{f^+f^-} \times d\hat{f}_{E,IFF}^- \tag{D.21}$$

Where, K_{f^+u} and $K_{f^+f^+}$ and $K_{f^+f^-}$ can be computed as follows,

$$K_{f^+u} = w_{igp}\bar{N}\frac{\partial \varepsilon}{\partial f_{E,IFF}^+} BdetJ \tag{D.22}$$

$$K_{f^+fn^+} = \frac{\partial f_I^+}{\partial \hat{f}_{E,IFF}^+} + \frac{\partial f_{II}^+}{\partial \hat{f}_{E,IFF}^+} - \frac{\partial f_D^+}{\partial \hat{f}_{E,IFF}^+} \tag{D.23}$$

$$K_{f^+f^-} = \frac{\partial f_I^+}{\partial \hat{f}_{E,IFF}^-} + \frac{\partial f_{II}^+}{\partial \hat{f}_{E,IFF}^-} - \frac{\partial f_D^+}{\partial \hat{f}_{E,IFF}^-} \tag{D.24}$$

Similarly,

$$dr^{e-} = \frac{\partial \left(f_I^- + f_{II}^- + f_D^-\right)}{\partial \hat{u}} d\hat{u} + \frac{\partial \left(f_I^- + f_{II}^- + f_D\right)}{\partial \hat{f}_{E,IFF}^+} d\hat{f}_{E,IFF} + + \frac{\partial \left(f_I^- + f_{II}^- + f_D\right)}{\partial \hat{f}_{E,IFF}^-} d\hat{f}_{E,IFF}^- \tag{D.25}$$

$$= K_{f^+u} d\hat{u} + K_{f^+f^+} d\hat{f}_{E,IFF}^+ + K_{f^+f^-} d\hat{f}_{E,IFF}^- \tag{D.26}$$

Where, K_{f^-u} and $K_{f^-f^+}$ and $K_{f^-f^-}$ can be computed as follows,

$$K_{f^-u} = w_{igp}\bar{N}\frac{\partial \varepsilon}{\partial f_{E,IFF}^+} BdetJ \tag{D.27}$$

$$K_{f^-f^+} = \frac{\partial f_I^-}{\partial \hat{f}_{E,IFF}^+} + \frac{\partial f_{II}^-}{\partial \hat{f}_{E,IFF}^+} - \frac{\partial f_D^-}{\partial \hat{f}_{E,IFF}^+} \tag{D.28}$$

$$K_{f^-f^-} = \frac{\partial f_I^-}{\partial \hat{f}_{E,IFF}^-} + \frac{\partial f_{II}^-}{\partial \hat{f}_{E,IFF}^-} - \frac{\partial f_D^-}{\partial \hat{f}_{E,IFF}^-} \tag{D.29}$$

VITA

Name-Surname: Süleyman Yaşayanlar

Educational Information:

Graduation Degree	Institution	Graduation Year
BSc.	Celal Bayar University	2011
MSc.	Izmir Institute of Technology	2015
PhD.	Izmir Institute of Technology	2023

Employement:

- **Mechanical Analysis Lead Engineer** **2023-Present**
  General Electric – Aviation

- **Research Assistant** **2015-2022**
  Civil Engineering Department
  Izmir Institute of Technology

Publications:

- Süleyman, Y., İzzet, Ö., Bekir, K. (2022). Localizing Implicit Gradient Damage Based Treatment of Softening in Elasto-plasticity, Procedia Structural Integrity, 35, 18-24

- Selçuk, S., Süleyman, Y., Yonca, Y., Baturay, B. (2019). Çelik fiber katkısının farklı boyuna donatı oranına sahip betonarme döşemelerin zımbalama davranışı üzerinde etkileri. Gazi Üniversitesi Mühendislik Mimarlık Fakültesi Dergisi, 34, 1045-1060